THE UNIVERSITY OF CHICAGO

ORGANIC SELF-ASSEMBLED MONOLAYERS: CHEMICAL AND STRUCTURAL RESPONSES TO TEMPERATURE, LIGHT, AND REACTIVE GAS SPECIES

A DISSERTATION SUBMITTED TO
THE FACULTY OF THE DIVISION OF THE PHYSICAL SCIENCES
IN CANDIDACY FOR THE DEGREE OF
DOCTOR OF PHILOSOPHY

DEPARTMENT OF CHEMISTRY

BY
SARAH BROWN

CHICAGO, ILLINOIS
MARCH 2022

Nevertheless, she persisted.

Contents

List of Figures

Acknowledgements

To Amélie, Caroline and Michael: thank you for sharing your passion of physics and chemistry. I would never have pursued a degree in chemistry and physics if it weren't for your courses 10 years ago.

To my committee members, Andrei and David: thank you for taking an interest in me and my science, and for always making me feel like my work was truly interesting and exciting. Andrei, thank you for also being an incredible Department Chair to work with over the years; we might still have a long way to go, but I'm proud of the positive changes that we've made thus far.

To Steve: thank you for never letting me settle as a scientist, and for knowing when to push me that one step further. I will always cherish our shared love of ice skating and appreciate your kindness, especially during the Pandemic Times.

To Vera, Melinda, Maria, Brenda, Laura L, Tanya and Bahareh: thank you for having the answers to all of the questions all of the time, for making it a little easier to navigate this journey, and for always being up for a good gossip over wine or cookies.

To the MRSEC family, especially Justin and Qiti: thank you for opening my eyes to the world of materials science and for teaching me the power of collaboration.

To the ghosts of Sibener Group past – Grant, K2, Jon, Jeff, Darren, Ross, Becca, Tim and Jacob: thank you for sharing your knowledge and friendship over the years. Jeff and Darren, thank you for teaching me the ways of UHV-STM and spending countless hours in E011 troubleshooting liquid nitrogen dewars and yelling (or singing) at SAMs, for teaching me how to do my taxes,

and for nailing the Friday NYT crosswords. Jon, thank you for literally always being ready to go to some random fun event in Chicago at a moment's notice, and for talking through science shenanigans when I was stuck on a problem. And Tim, thank you for being the best officemate from day one; the past year has been a lonely one without you, but I promise that I've managed to keep the SlimJim alive.

To the Sibener Group of the present – OG Kevin, Michelle, Ali, Julia, Sarah W, Caleb, Rachael, Josh, Jasper, Blake, Mark and Michael: thank you for keeping the work days cheerful and the office parties plentiful. Sarah and Rachael, thank you for bringing fresh insanity and reality TV shows to the STM lab. Jasper, thank you for showing off pictures of your cat as much as I do, and for putting up with me being a completely chaotic mentor – keep me posted on the amazing science things that you accomplish with the Brown STM. And, to my Emotional-Suppot Julia: thank you for being the best of friends at work and in life. Please know that I will absolutely continue sending you emails to proofread until we are too old to use computers.

To my UChicago Chemistry Cohort: thank you for forming the best inner tube water polo team ever, and for being the life of the party at all department events. Laura, Bo, Youjin and Huw, thank you for the continued love, support and tea dates, and for being the best of friends.

To my fellow department leaders (Tea Mom Buds, WiC and WISC): we've done our best to make this department a better place, and I'm proud of all that we accomplished together. Thank you for making that load feel a little lighter as we've carried it together.

To my White Tigers: when I was an extremely homesick first year, you gave me a place to belong on the soccer pitch. Thank you for your friendship, and for trusting me to be your captain.

To my scuba crew: I never thought that I'd be within spitting distance of becoming a scuba instructor as I finished my Ph.D. in Chicago. Thank you to Memo for introducing me to this amazing world, and to all of you for teaching me the value of bubble time.

To my Katies: I literally would not have survived this long into the pandemic without you two. Thank you for literally always being there, for cheering me on no matter how small the accomplishment, for driving me wherever is needed in an emergency, for fondue dinners in back alleys, and for co-founding the magical Cabin Club.

To my JAC Girls: 10 years after graduating from Abbott, we're still having 7-way video chats and get-togethers. Thank you for showing me that real friendships truly can endure the tests of time.

To Kate: thank you for keeping me sane during undergrad, for always coming to visit me in Chicago, and for showing me where all of the good food is. This is currently the furthest apart we've ever lived, and I miss you.

To my family (and friends who are basically family): thank you for always making me feel like some kind of science rock star, and for being my biggest cheerleaders. I can't wait until I can come home and celebrate in-person with you all.

To my Mum: thank you for telepathically helping with all of my math homework, for teaching me how to fit far too many things into my schedule, for cultivating my love of the ocean, and for endless energy from power kisses.

To my Dad: thank you for telling me way more than I ever wanted to know about torque and airplane engines, for always being ready to stop for a snack, for cultivating my love of travel, and for always offering me a cup of tea – even if it's over the phone.

To Lisa: thank you for being my first teacher and endlessly discussing pedagogy with me, for eating your way through Chicago every time you come to visit, for numerous years of Nintendo competitions, nights on soccer fields and shared skating lessons, and for just generally being the best big sister anyone could ask for.

And finally, to EW: it seems fitting that you were the first person that I met in this crazy town. Thank you for always being there even when you were far away, for agreeing to spend every Christmas vacation in Montreal, for keeping our lives going while I was neck-deep in thesis writing, for the back rubs and head massages and infinite hugs, and for being the best cat dad to Bootsie – even if you do squash her against her will.

Abstract

Characterising the structural dynamics of materials is crucial to their implementation in real-world applications. Knowing how a system will respond to a particular stimulus, and understanding that response from a fundamental chemistry standpoint, is key to success in nanoscience. Accordingly, this thesis describes the use of kinetics and dynamics experiments to relate the structural behaviour of organic self-assembled monolayers to their environmental conditions.

The work herein examines three different self-assembled monolayers perturbed by three different external stresses. First, we present the classic self-assembly system of alkanethiols on Au(111) and show how their ability to effectively passivate metal surfaces when bombarded with reactive gas species is strongly dependent on both film thickness and substrate temperature. The use of localised imaging techniques such as scanning tunnelling microscopy (STM) allows us to relate these observations to the monolayer restructuring and surface rearrangement that occurs throughout the reaction.

Second, we study how the topographical and crystalline nature of novel wafer-scale two-dimensional (2D) porphyrin polymers (specifically, metal-organic frameworks (MOFs)) are impacted by sample annealing and post-anneal cooling rates. Understanding these temperature-dependent structural phases is important for knowing the application limitations of such films – and for recognising previously unknown application potential.

Finally, we explore the cooperative dynamics of azobenzene-functionalised liquid crystal (LC) thin films in response to irradiation with ultraviolet (UV) light. Although much work has already been done on the production of azo-functionalised thin films, it remains challenging to induce simultaneous and coherent isomerisation of an entire film. Understanding the dynamic interaction between molecules within the film is therefore crucial to making uniformly switchable films a molecular engineering reality.

Chapter 1

Introduction

The chemistry that occurs at surfaces is distinct from any other. Unlike bulk solutions, where molecules typically find themselves in homogeneous and isotropic environments, interfaces cause a reduction in dimension that gives rise to the concepts of orientation and directionality. As such, many important chemical and physical phenomena occur at the interface between two media, making the study of surface chemistry relevant to the real-world applications of food production, surface disinfection, corrosion inhibition – and more!

Some of the most scientifically intriguing surfaces to study are those formed by molecular thin films, and in particular, self-assembled organic thin films. These two-dimensional (2D) structures are composed of molecules that spontaneously self-organise into periodic patterns on a substrate or at an interface. The characteristics of the film are distinct from those of the individual molecules, due to both the vertical molecule-substrate and horizontal molecule-molecule interactions. Furthermore, given the high potential for chemical tunability within the components of the film, self-assembled monolayers provide much promise for the bottom-up fabrication of functional surfaces.[1–5]

Understanding the structural dynamics and chemical reactivity of these films is paramount to their implementation in real-world applications. This thesis explores the behaviour of three different organic self-assembled monolayers upon exposure to various environmental stresses and chemical reactants, and seeks to characterise these phenomena using physical chemistry principles and surface science techniques such as scanning tunnelling microscopy (STM).

Chapters 3 and **4** explore a classic self-assembly system that has been well-documented over the past 30 years: thiolate self-assembled monolayers (SAMs) on Au(111). Each molecule in these films consists of a sulphur head group adhered to the gold, and a carbon-based "tail" that extends away from the surface. Any number of chemical functionalities may be incorporated

into the molecular tail, which can customise the SAM's packing structure and chemical and physical properties. Thiolate SAMs also form multiple surface density-dependent phases on the Au(111) surface that are distinguishable using a variety surface analysis techniques, meaning that changes in monolayer structure are easily trackable. The experiments in **Chapter 3** focus on alkanethiolate SAMs of different lengths (8- to 11-carbons long) and examine how thiol film thickness influences the monolayer's reaction kinetics with atomic hydrogen. The use of localised analysis techniques such as scanning tunnelling microscopy (STM) also allows us to characterise the chain length-dependent surface rearrangement that occurs throughout the reaction. **Chapter 4** brings this work one step further and investigates how the combined effects of substrate temperature and alkanethiolate chain length influence the SAM's dynamic structure and, consequently, passivation capabilities.

In **Chapter 5**, we move towards SAMs that rely more heavily on lateral interactions in their assembly compared to vertical ones by studying the structural dynamics of two-dimensional (2D) porphyrin polymer films, specifically 2D metal-organic frameworks (MOFs). The growth and characterisation of 2D MOFs is of particular interest for applications as smart membranes, chemical sensors and other nanodevices,[6] and the Park Group (University of Chicago) has developed a novel wafer-scale synthesis for 2D porphyrin-based polymer heterostructures. My initial role in this collaboration was to confirm the hypothesised structure of the films using STM, but this chapter also elaborates on how post-anneal cooling rates influence the MOFs' topography and crystallinity, which could have important consequences on their applicability.

Finally, **Chapter 6** discusses ongoing work with self-assembled azobenzene-functionalised liquid crystal (LC) thin films and their potential uses in active/intelligent material design. Materials that can reliably, reproducibly and reversibly change their properties in response to external stimuli are of keen interest in the bottom-up fabrication of intelligent matter, and the azobenzene moiety is a classic way of inducing structural change in a material upon irradiation with UV light. This project is currently in the investigatory stages of producing and imaging LC films, as well as designing new azo-functionalised molecules in collaboration with the Rowan Group (University of Chicago) that will allow us to study the cooperative dynamics within these films.

Chapter 2

Instrumentation and Experimental Methods

Ambient chemistry is a messy business. At room temperature and atmospheric pressure, gas molecules collide with a surface at a rate of $\sim 10^{23}$ collisions $cm^{-2}s^{-1}$. In order to study specific surface chemistry processes, vacuum conditions are typically required to eliminate any background gases that may cause side undesired side reactions. We therefore perfom the bulk of the work in this thesis in an ultrahigh vacuum (UHV) chamber equipped with a variety of surface analysis techniques. The overall instrument design and main tools used are outlined in this chapter, and any procedures or equipment specific to a particular project are detailed later on.

2.1 Instrument Design

The UHV setup employed for this thesis work is pictured in **Figure 2.1** and consists of three stainless steel chambers separated by gate valves (SoftSht and VAT): the load lock, the microscope chamber and the sample preparatory ("prep") chamber. A transfer arm (Thermionics) is used to move samples horizontally between chambers. UHV chamber pressures are measured using Bayard-Alpert nude ion gauges and Convectron® Pirani Vacuum Gauges (Granville-Phillips).

The load lock is a small chamber designed to facilitate transferring samples into/out of the instrument without venting the microscope and/or prep chamber. It has a base pressure of around 1×10^{-8} Torr that is achieved using a turbomolecular pump (œrlikon Leybold Vacuum Turbovac SL80) backed by a dry scroll pump (Agilent Technologies SH-110).

The prep chamber houses many of the instrument's surface analysis tools. It operates at a base pressure of around 1×10^{-10} Torr, which is sustained using a TiTan 200 L ion pump (Gamma Vacuum). A mechanical hand (VACGEN) is used to move the sample from the transfer

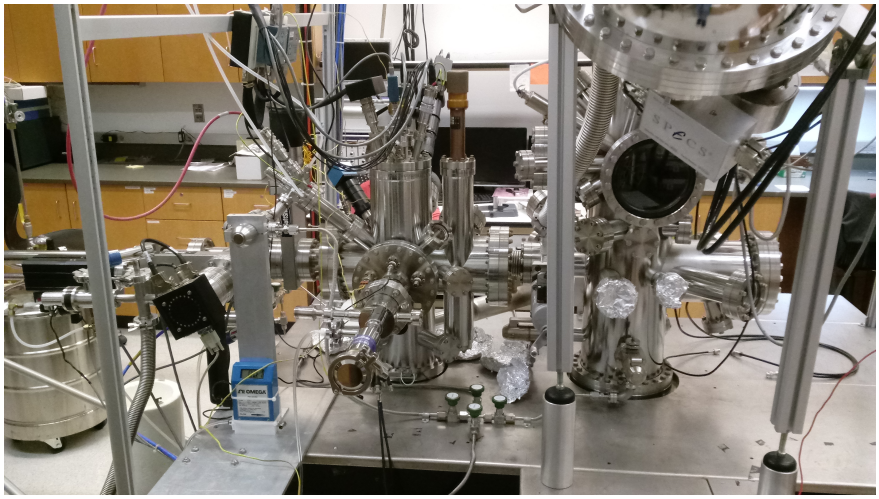

Figure 2.1: Photograph of the UHV setup employed for this thesis work. The load lock is on the far left, the microscope chamber is in the middle, and the prep chamber is on the right. The transfer arm used to move samples horizontally between chambers can also be seen to the left of the load lock.

arm to the four-axis manipulator (x-, y- and z-translation, and polar rotation), on which it is mounted during any procedures in the prep chamber. Although this thesis will not heavily feature the prep chamber's functionality, it houses many powerful surface science tools including a hemispherical electron energy analyser and an X-ray gun (SPECS) for X-ray photoelectron spectroscopy (XPS), an electron gun, an ion sputter gun (RBD Enterprises 04-172 Ion Gun), a residual gas analyser (RGA 300, Stanford Research Systems), sample heating and cryogenic cooling capabilities, and a homemade evaporative physical vapour deposition setup.

Almost all of the work done in this thesis was performed in the microscope chamber. Like the prep chamber, the microscope chamber operates at a base pressure of around 5×10^{-11} Torr (Gamma Vacuum TiTan 200 L ion pump) and uses a fork perpendicular to the transfer arm (a "wobble stick") (RHK) to move samples around the chamber. Samples and microscope tips are both housed in "pucks", which are then stored in the chamber's sample elevator.

The main feature of the microscope chamber is an RHK 350 Beetle UHV Variable Temperature Atomic Force Microscopy/Scanning Tunnelling Microscopy (AFM/STM) microscope. With a practical operating temperature range of 25-373 K, sample cooling and heating are achieved using a continuous flow cryostat (Cryo Industries) and filament heating (radiative or electron bombardment) respectively. More details on sample temperature control during experiments can be found in **Section 2.3**.

Finally, the microscope chamber also houses a Mantis MGC-75 thermal gas cracker, allowing samples to be dosed with atomic hydrogen or oxygen in situ while imaging. As shown in **Figure 2.2**, the gas cracker flow is in the line of sight of the sample stage, 8 cm away and oriented at 50° from the surface normal. Gas is introduced into the cracker through a leak valve (Agilent Technologies) and passes through a 3 mm diameter iridium capillary that is heated to approximately 2000 K via electron bombardment. Any molecular gas that touches the capillary as it passes through is hence thermally dissociated, with a cracking efficiency for low hydrogen flow rates of $\sim 90\%$[7]. More details on the atomic gas dosing procedures used in this thesis can be found in **Section 2.4**.

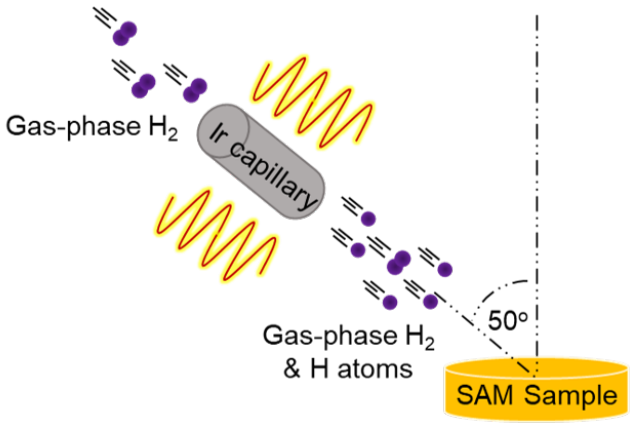

Figure 2.2: Schematic of the MGC-75 gas cracker setup within the microscope chamber. The gas cracker flow is in the line of sight of the sample stage, 8 cm away and oriented at 50° from the surface normal. Molecular gas passes through a 3 mm diameter iridium capillary that is heated via electron bombardment. Any molecular gas that touches the capillary as it passes through is hence thermally dissociated, with a cracking efficiency for low hydrogen flow rates of $\sim 90\%$

2.2 Scanning Tunnelling Microscopy (STM)

The main surface analysis technique employed throughout this thesis is scanning tunelling microscopy (STM). Unlike more traditional ensemble techniques such as low energy electron diffraction (LEED) and XPS, the localised nature of STM allows us to investigate surface kinetics and dynamics on the molecular scale.[8;9]

STM operates on the principle of quantum tunnelling to probe the electronic structure of a surface using an atomically-sharp conductive tip. A small electrical potential (termed "bias voltage") is applied to either the tip or the sample, and the tip is brought within angstroms of

the sample. Although the space between the tip and sample has a high potential barrier, making current flow classically forbidden, quantum tunnelling can occur because the electron's wave function remains non-zero even in classically-forbidden regions. Therefore, electrons will tunnel across the gap from the area of lower voltage (more negative) to the area of higher voltage (more positive). Because the rate of electron tunnelling is exponentially dependent on both the length of the vacuum gap (distance between the tip and the sample) and the the energy barrier heights (work functions of the tip and sample materials),[10] the tunnelling current is extremely sensitive to changes in sample height, allowing one to obtain atomically-resolved images with high fidelity. An energy diagram of the tunnelling junction can be found in **Figure 2.3**.

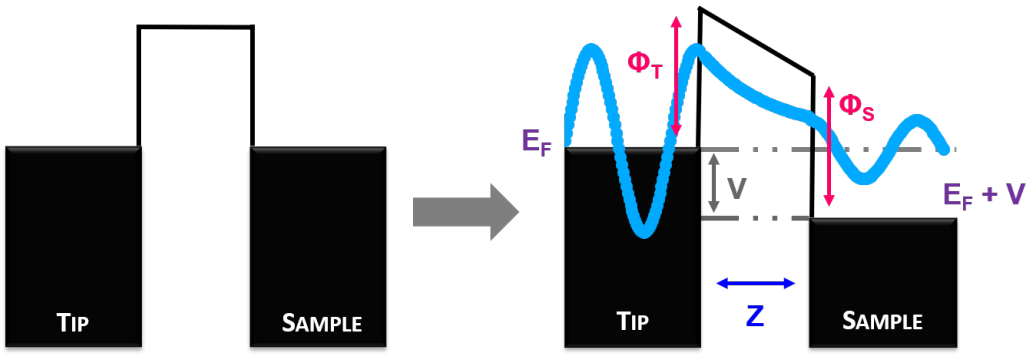

Figure 2.3: An energy diagram of the tunnelling junction in an STM setup. In this scenario, a positive bias has been applied to the sample, promoting flow of electrons from the tip to the sample. E_F is the Fermi level, Φ_T and Φ_S are the work functions of the tip and the sample respectively, V is the applied bias voltage, and Z is the distance between the tip and the sample.

The position of the STM tip is controlled with a piezoelectric tube, which maintains precise control over tip movement over extremely small distances (10^{-10}–10^{-9} m). The tip is rastered over the surface, producing a series of lines that are stacked to form the image (typically 512 lines per image for high resolution). At each pixel in the image, two pieces of information are collected: the tip height (how extended or retracted the piezo tube is relative to its equilibrium position) and the tunnelling current measured between the tip and the sample. The STM can therefore display two different types of information for any image that it takes.

There are two modes of STM imaging: constant current and constant height. In constant current mode, a current set point is decided by the user and the STM moves the tip up and down (controlled by a proportional-integral (PI) feedback loop) while imaging in order to maintain this tunnelling current. In constant height mode, the user sets a particular tip height that must

be maintained, and the STM measures the variation in current as it moves across the surface. Constant current mode is the more common method of using STM for imaging purposes, and it is the only method used in this thesis. A schematic of an STM constant current setup is shown in **Figure 2.4**.

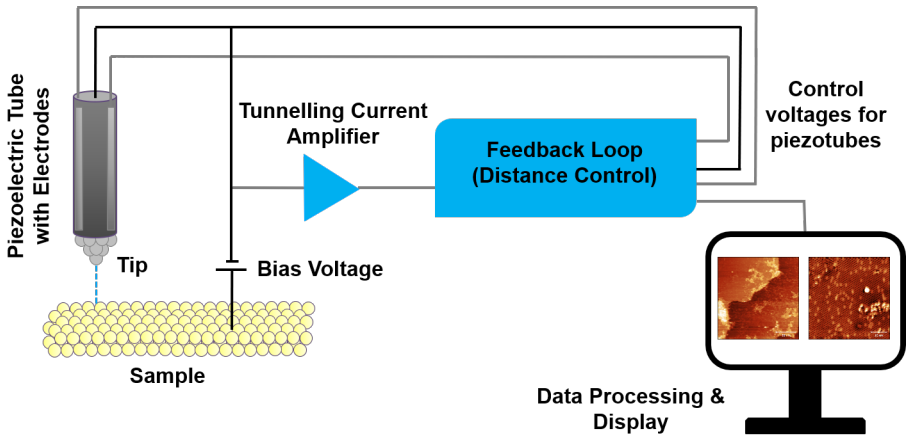

Figure 2.4: Schematic of a constant current STM setup.

It is important to note that the images produced using STM are a convolution of topographical and electronic density information. Because the density of electronic states (DOS) of the sample will affect the tunnelling current, it can make certain electron-rich (high DOS) surface features appear "taller" than they physically are. However, while this can sometimes be a slight hindrance to interpreting STM images, it also allows for a method of interrogating the sample's electronic information, known as scanning tunnelling spectroscopy (STS).[10]

Finally, we performed all of our STM image processing using Gwyddion, an open-source software for SPM data analysis.[11]

2.3 Sample Temperature Control

The ablitiy to cool our samples on the imaging stage is vital to the work presented in **Chapters 4** and **5**. As previously stated in **Section 2.1**, sample cooling is achieved by flowing a cryogenic liquid (in our case, liquid nitrogen (LN2)) through a continuous flow cryostat attached to the imaging stage. The cryogen's flow rate is monitored with a flow meter on the cryostat's exhaust valve, and the sample's temperature is monitored using a K-type (chromel-aluminel) thermocouple. An N_2 exhaust flow of 1.0-2.0 L min^{-1} is required to avoid introducing noise

into the STM images.

In order to control the sample temperature within 0.01 K, variable heating is applied while the sample is cooled. This is achieved via radiative heating from a tungsten filament that is mounted underneath the sample within the sample puck. The output of the power supply attached to the filament is regulated by a Lakeshore 331 Temperature Controller, which uses the sample's thermocouple reading and a proportional-integral-derivative (PID) feedback loop to determine the heating required to maintain the target setpoint temperature.

2.4 Atomic Gas Reaction Methods

Chapters 3 and **4** rely on the MGC-75 to produce atomic hydrogen (H) for in situ reaction with alkanethiolate self-assembled monolayers (SAMs). This section outlines the reaction procedure used for these experiments.

All of the atomic H experiments in this thesis are statistical; that is, each sample is surveyed in multiple locations and the results are averaged to give a complete picture of the overall reactivity. We therefore fully retract the microscope scan head from the sample during exposures to prevent shadowing from the STM tip.

Typical operating parameters for the gas cracker are a filament current of ~ 2.68 A and a capillary power of 40 W, with water cooling lines required to be running for cracker function. Once these conditions are met, molecular gas is introduced into the cracker through a leak valve until the desired experimental pressure is reached (1.0×10^{-7} Torr for the experiments in this thesis). Note that the ion gauges in the microscope chamber are calibrated for N_2, which has twice the sensitivity factor of H_2, so appropriate corrections must be made when reading the pressure of hydrogen in the chamber.

After the chamber pressure and gas cracker power have stabilised, the manual shutter in front of the cracker is opened and the reaction begins. To end the reaction after the desired experiment time, the shutter and leak valve are closed and the filament current is turned off. The microscope scan head can then be relowered for post-reaction imaging. Although a small amount of sample heating occurs during the dosing with atomic gases, there is minimal thermal drift in the imaging that follows. In particular, we note that in the experiments below room

temperature in **Chapter 4**, the thermocouple reading never increases more than 1 K, even after long exposures.

2.4.1 Calculation of Atomic Gas Flux at the Sample Surface

We can estimate the H-atom flux reaching the sample surface using our microscope pressure and pumping speed. First, for an ion gauge reading of 5.0×10^{-8} Torr and an H_2 ion gauge correction factor of 0.46, we assume our actual H_2 pressure to be

$$\frac{5.0 \times 10^{-8}\ \text{Torr}}{0.46} = 1.09 \times 10^{-7}\ \text{Torr} \tag{2.1}$$

Next, because we maintain a constant pressure in the chamber, we know that the amount of gas being pumped out of the chamber must equal the amount of gas being pumped in. Therefore, with an ion pump pumping speed of 200 L s^{-1}, we have

$$pV = nRT \tag{2.2}$$

$$(1.09 \times 10^{-7}\ \text{Torr})(200\ \text{L s}^{-1}) = n(62.36\ \text{L} \cdot \text{Torr mol}^{-1} \cdot \text{K}^{-1})(298\ \text{K}) \tag{2.3}$$

$$n = 1.17 \times 10^{-9}\ \text{mol s}^{-1} \tag{2.4}$$

$$= 7.06 \times 10^{14}\ \text{molecules s}^{-1}\ \text{of}\ H_2 \tag{2.5}$$

entering the gas cracker from the leak valve. With a cracking efficiency of 90%, this means that we have

$$(2)(0.9)(7.06 \times 10^{14}\ \text{molecules s}^{-1}) = 1.27 \times 10^{15}\ \text{H atoms s}^{-1} \tag{2.6}$$

exiting the cracker.

To find the atomic H flux at the sample surface, we assume that the gas cracker is an effusive hemispherical emitter. This assumption is valid given that the mean free path $\lambda \approx 1$ km under our pressure and temperature conditions, and that the H atoms exiting the cracker are thermally distributed in front of the gas cracker. Thus,

$$\text{Flux}_{\text{surface}} = \frac{\text{Flux}_{\text{cracker}}}{2\pi d^2} \tag{2.7}$$

where d is the distance between the source and the sample. Finally, because the cracker is oriented at 50° from the surface normal, there are

$$\text{Flux}_{\text{surface}} = \frac{1.27 \times 10^{15} \text{ H atoms s}^{-1}}{2\pi(8 \text{ cm})^2} \cos(50^\circ) \tag{2.8}$$

$$= 2.03 \times 10^{12} \text{ H atoms s}^{-1} \text{ cm}^{-2} \tag{2.9}$$

reaching the sample surface.

2.4.2 Calculation of Alkanethiolate Reaction Probability

To compute the reaction probabilities of 1-decanethiolate (10C) SAMs with atomic H in **Chapter 4**, we first estimate the molecular density of an unreacted 10C SAM. Using STM images to estimate the area of a single hexagonal close-packed alkanethiol molecule to be 0.216 nm^2 (4.63×10^{14} molecules cm^{-2}) and the area of a single low-density phase alkanethiol molecule to be 0.64 nm^2 (1.56×10^{14} molecules cm^{-2}), and assuming an unreacted SAM surface composition of 0.95:0.05 (high density:low density), we find an average unreacted SAM surface density of 4.48×10^{14} molecules cm^{-2}.

If we assume this SAM surface density to be approximately constant for the first 12.36 min of the reaction (**Figure 4.2**), there are

$$(741.6 \text{ s})(2.03 \times 10^{12} \text{ H atoms s}^{-1} \text{ cm}^{-2}) = 1.51 \times 10^{15} \text{ H atoms cm}^{-2} \tag{2.10}$$

H atoms hitting the surface during this time period. We can therefore estimate the reaction probability for this interval as

$$\frac{4.48 \times 10^{14} \text{ molecules cm}^{-2}}{1.51 \times 10^{15} \text{ H atoms cm}^{-2}} = 0.297 \approx 30\% \tag{2.11}$$

and we can perform similar calculations for any other discrete time intervals during a SAM

reaction.

2.5 Thin Film Preparation

2.5.1 Alkanethiolate Self-Assembled Monolayers

We purchased our alkanethiols (1-octanethiol ($\geq$ 98.5%), 1-nonanethiol (99%), 1-decanethiol (99%) and 1-undecanethiol (98%)), 1H, 1H, 2H, 2H-perfluorodecanethiol (97%), and absolute ethanol (ACS Reagent Grade, > 99.5%) from MilliporeSigma and used them without any additional purification. Our gold substrates are Au(111)-on-mica samples (gold thickness of $\sim$ 150 nm) obtained from Keysight Technologies (**Chapter 3**) and Phasis (**Chapter 4**) as 10 mm $\times$ 10 mm squares. We cut the squares into smaller sizes prior to use (2.5 mm $\times$ 5 mm and 5 mm $\times$ 5 mm, depending on the experiment), and annealed them with a hydrogen flame to both remove any trace contaminants and enlarge the gold terraces. Following this preparation, we observe atomically flat gold terraces of $\geq$ 100-200 nm in size.

To form the thiolate SAMs, we prepare 1.0 mM solutions of each thiol in ethanol and immerse face up annealed gold substrates in each vial of solution. The vials are then annealed at 60 °C for $\sim$ 2.5 hr; this procedure accelerates the formation of densely-packed SAMs without damage to the molecules. Post-anneal, we allow the SAMs to cool to room temperature in their vials before rinsing with ethanol and drying in air. We then mount the samples into the UHV sample pucks and place them in the instrument load lock. Typically, the SAMs are exposed to atmospheric conditions for $\leq$ 30 min before entering vacuum, where they remain stable for multiple weeks. The ion gauges, however, must be turned off in any chamber(s) housing the samples, as stray electrons and/or ions have been shown to degrade thiolate SAMs.[12]

2.5.2 Liquid Crystal Thin Films

We purchased our liquid crystals (LC) (para-azoxyanisole (PAA) (98%) and N-(4-Methoxybenzylidene)-4-butylaniline (MBBA) (98%)) from MilliporeSigma and used them without any further purification. Our highly oriented pyrolytic graphite (HOPG) substrates are of grade ZYB (Bruker), and we cleave them with adhesive tape prior to film formation.

To create the liquid crystal thin films, we first prepare 1.0 mM solutions of each LC in

DCM (anhydrous, $\geq$ 99.8% MilliporeSigma). The solutions are spin coated onto the HOPG substrates at 3000 rpm for 1 min. The samples are then annealed in air at 130 °C for several hours, followed by a gradual cooldown period. Ellipsometry (LSE-WS) measurements suggest that these conditions produce films that are $\sim$ 200 nm thick, though atomic force microscopy (AFM) scratch tests are currently underway to confirm this value.

Chapter 3

Chain-Length-Dependent Reactivity of Alkanethiolate Self-Assembled Monolayers with Atomic Hydrogen

Gas-surface interactions are some of the most important yet complex chemical processes to occur, as they intrinsically involve many-body phenomena across a wide spectrum of energies and length scales. To understand these complicated interfacial interactions, we often use model systems such as thiolate self-assembled monolayers (SAMs) to study phenomena like reactivity and passivation, as these systems afford fine control over the surface parameters governing the events in question. In this study, we examine the effect of chain length on the reactivity of alkanethiolate SAMs with atomic hydrogen by monitoring morphological surface evolution throughout the reaction. These spatiotemporal data were obtained using ultrahigh vacuum scanning tunnelling microscopy (UHV-STM) with directed in situ atomic hydrogen dosing. For a series of alkanethiolate SAMs 8- to 11-carbons long, we find that small increases in chain length cause disproportionately large decreases in reactivity. These reaction trends led us to develop a kinetic model characterised by two rate constants: a slow rate for hydrogen reactivity with close-packed domains, which is chain-length dependent, and a fast rate for reactivity with low-density regions, which is the same for all samples examined. In addition to reaction rates, we also tracked chain-length-dependent changes in surface morphology, notably how the size and shape of the SAMs' etch pits evolved following hydrogen exposure. Few differences were

observed in the 10C and 11C samples, while there was a significant increase in the mean etch pit area of the 8C and 9C SAMs. Overall, this study provides important quantitative insights into how surface packing and dynamic disorder of organic thin films can influence their passivation capabilities.

3.1 Introduction

Thiolate self-assembled monolayer (SAMs) on Au(111) are some of the most well-studied systems in the surface science community.[14–17] These materials consist of densely packed organic molecules that are chemisorbed onto a metal substrate and arranged in a highly ordered two-dimensional (2D) polycrystalline structure. The tunability of the molecules' chemical functionality allows for the control of surface properties such as wetting,[18–21] adhesion,[20;22] photoactivity,[23] and chemical reactivity.[16] This versatility has enabled SAMs to be used in a variety of applications ranging from biomimetics[18;22;24;25] to corrosion inhibition.[26;27]

The versatility of SAMs has also popularised their use as model systems for studying gas-surface interactions. These are some of the most important yet complex chemical processes, as they intrinsically involve many-body phenomena across a wide spectrum of energies and length scales. However, this also means that they often require simplified model systems to facilitate their study. An appropriately selected SAM can hence be used to probe reaction dynamics as a function of surface parameters such as the chain length, chain parity, or chemical functionality.[28] For example, alkanethiolate SAMs have been used to explore the reactivity of atomic gases with hydrocarbons, which has importance for applications such as the passivation of electronic surfaces with organic thin films.[29;30]

Several groups have studied thiolate SAM reactivity with energetic gas species such as H,[28;31–38] O,[39–43] and O_3,[44–46] as adsorption energetics and reaction dynamics are of great interest to the surface science community. For example, techniques such as X-ray photoelectron spectroscopy[28;41] and reflection absorption infrared spectroscopy[39] have been used to explore the effect of chain length on the reactivity of alkanethiolate SAMs with atomic gases. However, these spectroscopic methods are limited to providing spatially averaged information about the reactive surface as a whole; they cannot identify how individual surface features evolve over

the course of the reaction.

To study the nanoscale kinetics of chain-length-dependent alkanethiolate SAM reactivity, we must therefore employ a more localised technique such as scanning tunnelling microscopy (STM). The direct-imaging and nondestructive nature of scanning probe microscopy typically allows better investigation of the mechanistic details of such reactions. Furthermore, results from previous STM studies of thiolate SAMs already provide us with important information on how variables such as temperature,[16;47–50] local surface environment,[37] and exposure to reactive gases[32–37;40;43] will influence a SAM's film structure. For example, earlier work by Kandel's group[35] shows how 1-octanethiolate SAMs react with atomic hydrogen and how the resultant monolayer damage is characterisable with STM. In particular, this work emphasises the key role that domain boundaries play in SAM reactivity as well as how the adsorbate overlayer restructures throughout the reaction. As discussed below, our work builds upon these early findings, including the formulation of a comprehensive kinetic model that quantifies the overall chain-length-dependent reactivity for the various SAM phases. Subsequent studies[33;34] also reveal some molecular-scale mechanistic details of this reaction, with a focus on how gold adatoms are incorporated into alkanethiolate SAMs during monolayer formation, findings with which we agree. Finally, STM studies of hydrogen's reaction with bulkier, substituted thiolates such as 1-adamantanethiolate[32] show that the incorporation of gold adatoms into SAMs is not unique to *n*-alkanethiolates; however, the reduced packing density of these substituted monolayers does impact how the thiol molecules bind to and organise on the surface.

Here, we present a comprehensive ultrahigh vacuum scanning tunnelling microscopy (UHV-STM) study on how chain length impacts the microscopic surface reconstruction of alkanethiolate SAMs during their reaction with atomic hydrogen (H). We track the reaction progression of four alkanethiolate SAMs (8- to 11-carbons long) by monitoring the surface fraction of close-packed thiols remaining after each hydrogen exposure. This progression is then correlated with the time-evolving local structure of high- and low-density molecular domains. These data have allowed us to develop a model that quantitatively describes the observed kinetics for short-chain alkanethiolate SAMs. Furthermore, we address spatiotemporal correlations in these reactions by characterising the surface rearrangements that occur in both the monolayer and underlying substrate, with emphasis on how these changes depend on alkanethiolate chain length. This

study demonstrates the variances in the passivation efficacy of these organic thin films with respect to attack by atomic hydrogen.

3.2 Experimental Section

Experiments were performed in the UHV microscope chamber described in **Section 2.1**, and using the MGC-75 gas cracker introduced in **Section 2.4**. Thiolate SAMs were prepared according to the procedure outlined in **Section 2.5.1**.

STM images were taken with a +0.70 V bias on the sample and a tunnelling current setpoint of 10 pA. To obtain precise data on relative reaction rates between SAMs of different chain lengths, two 2.5 mm $\times$ 5 mm samples were adjacently mounted and dosed simultaneously for each reaction: a 1-decanethiol sample, to be used as a control between the different experiments, and a second SAM sample of the desired length (8-, 9- or 11-carbons long). We also mounted two 10C samples together in a control experiment and observed identical reaction profiles, thus confirming that both samples received the same exposure to hydrogen. This control also confirmed that there are no noticeable differences in reactivity due to variations in the Au(111) surface structure or SAM domain orientation relative to the gas flux.

3.3 Results and Discussion

Figure 3.1 presents STM images of the reaction progressions of a 1-decanethiolate SAM during its reaction with atomic hydrogen. These images are representative of the data taken during each experiment, for all chain lengths. The zero-minute panel of **Figure 3.1** shows the SAM prior to any atomic hydrogen exposure. Here, we see the typical features of a saturated alkanethiolate SAM on Au(111): The thiol molecules have self-organised into a standing-up hexagonal close-packed structure (**Figure 3.2**A) with a lattice constant of 0.50 nm and a c(4 $\times$ 2)R30° superlattice. The alkane tails of the thiol molecules are in trans configuration, tilted 32° from the surface normal, and the symmetry of the underlying gold lattice produces three degenerate molecular orientations.[16;51;52] From this rotational degeneracy, the SAM acquires a polycrystalline structure in which single-crystal domains, 20-30 nm in diameter, are separated by grain boundaries. In these grain boundaries, we also find circular defects known as etch pits, which are gold vacancies

created during the SAM's formation. It has been previously shown[33;34] that as the SAM forms, thiol molecules remove gold atoms from the substrate and incorporate them into the monolayer at a 2:1 thiol-to-gold ratio. This process leaves behind the etch pits with an average diameter of 5 nm, evenly scattered across the surface and filled with additional standing-up molecules (**Figure 3.2**B).

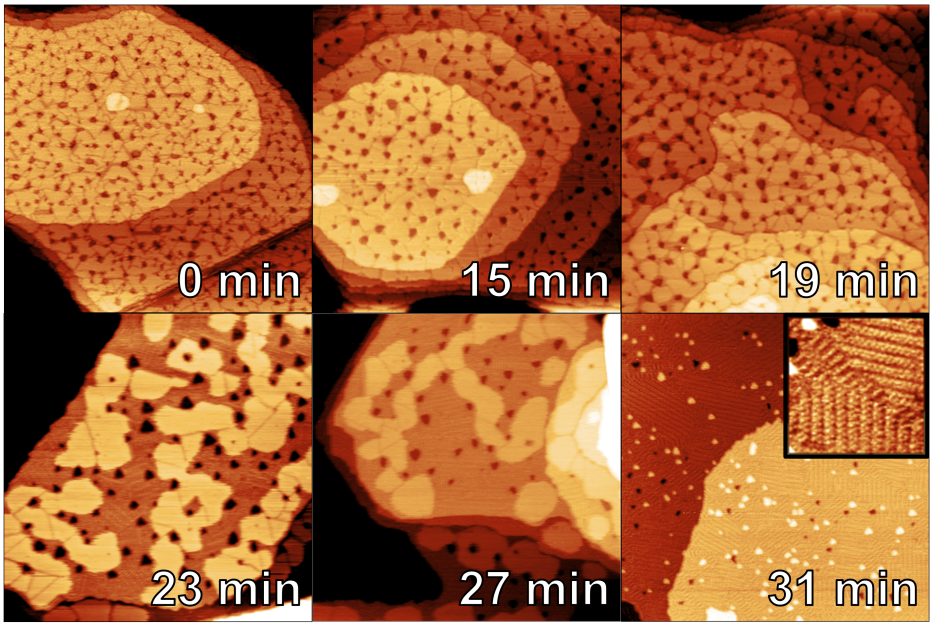

Figure 3.1: STM image progression (300 nm × 300 nm) of 1-decanethiolate SAM during its reaction with atomic hydrogen. At the end of the reaction, bright gold islands and low-density lying-down phase are visible on the gold substrate (see the inset 50 nm × 50 nm). The other three alkanethiolate SAMs (1-octanethiolate, 1-nonanethiolate, and 1-undecanethiolate) followed similar reaction pathways.

The later time points of **Figure 3.1** show the morphological changes of the SAMs upon exposure to hydrogen. According to previous studies,[28] H-atoms will react with alkanethiolate SAMs in one of two ways: complete removal of whole thiols through the cleavage of the sulphur-gold bond or removal of hydrocarbon fragments via piecewise erosion. For longer alkanethiolates ($C \geq 12$), reactivity is dominated by the latter mechanism. Hydrogen atoms react along the length of the hydrocarbon chains, which creates radical species and results in cross-linking between neighbouring chains. This cross-linking slows the desorption of thiol molecules from the surface and causes hydrocarbon species to leave the surface in fragments. For shorter alkanethiolates ($C \leq 12$), however, it is easier for atomic hydrogen to penetrate the thiolate film and directly attack the sulphur-gold bond.[28] We therefore expect to exclusively

observe the sulphur-gold bond cleavage mechanism in our experiments. Moreover, our results suggest that when longer-chain thiols diminish in length due to repeated reaction with hydrogen, thiol removal via subsequent sulphur-gold bond cleavage may also become a significant reaction channel.

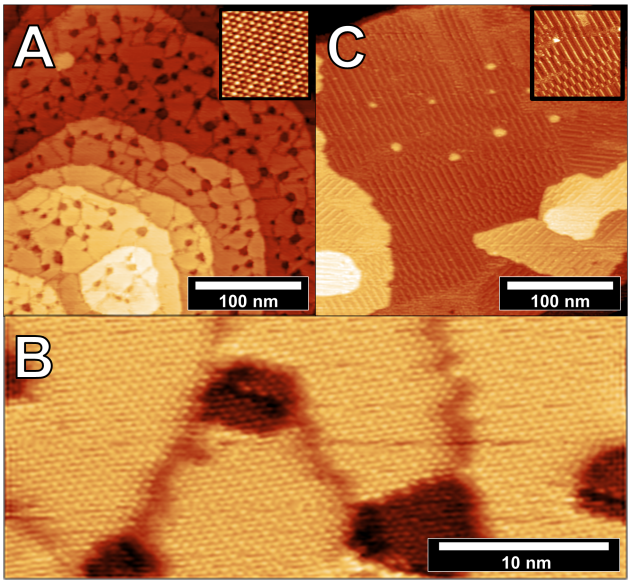

Figure 3.2: (A) STM image of an unreacted 1-decanethiolate SAM, with hexagonally close-packed domains separated by grain boundaries and etch pits. The inset (7 nm $\times$ 7 nm) shows molecular resolution of the thiolate lattice and the c(4 $\times$ 2)R30° superlattice. (B) Image of etch pits on a 1-decanethiolate SAM, where the close-packed hexagonal lattice is visible both inside and outside the pits. (C) Ordered low-density lying-down phase of 1-decanethiol. The inset (50 nm $\times$ 50 nm) shows bright and dark stripes corresponding to the aligned sulphur heads and the alkane tails, respectively.

This reactivity initially presents itself as the thickening of grain boundaries, in agreement with the observations of previous studies;[33–35;37] as molecules leave the surface, lower density thiolate phases begin to form and are observed in the STM images as darker regions. These low-density SAM phases include various disordered 2D fluid phases as well as ordered lying-down phases, which present as bright and dark stripes on the surface (**Figure 3.2**C).[15;47;49;53] Upon further exposure to hydrogen, the lower-density areas expand and interconnect, creating isolated puddles of standing-up phase. Eventually, no standing-up phase remains on the surface and small gold islands are formed from the Au atoms previously incorporated in the SAM.[33;34] We consider the reaction to be complete when no standing-up phase remains on the surface. A schematic of the phase changes that occur during a thiol SAM's reaction with atomic H is shown in **Figure 3.3**.

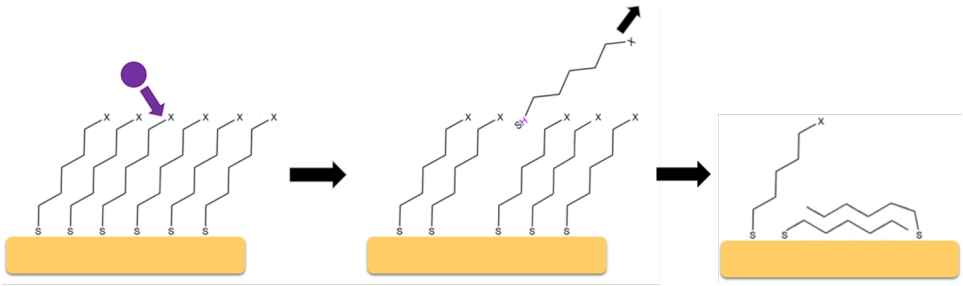

Figure 3.3: Schematic of the phase changes observed during the reaction of alkanethiol SAMs with atomic H. Prior to reaction, the thiol molecules are organised in a hexagonal close-packed structure tilted 32° from the surface normal. Upon bombardment with atomic H, intact alkanethiol molecules are removed from the surface. This removal creates enough space on the Au(111) substrate such that lower density thiolate phases begin to form, including ordered lying-down phases where molecules are aligned sulphur head-to-sulphur head and alkane tail-to alkane tail.

To quantify the reaction of alkanethiolate SAMs with atomic hydrogen, **Figure 3.4**A presents the area fraction of standing-up phase plotted as a function of hydrogen exposure time. We adjusted the exposure times for each reaction pair (10C and nC, where n = 8, 9, and 11) so that all decanethiolate times overlapped, enabling us to obtain relative reaction rates between all chain lengths. These data show that the rate of SAM reaction with atomic hydrogen decreases with increasing chain length, a fact that is also highlighted in **Figure 3.4**B where images of all four SAMs are compared at the same hydrogen exposure time. Remarkably, a chain length increase of a single carbon unit causes a disproportionately large decrease in the reaction rate; that is, a ∼10% increase in chain length corresponds to a 30% or greater decrease in reaction time (**Figure 3.4**C). It is also interesting to note that the reactivity does not depend noticeably on the parity of the carbon chains, despite even- and odd-numbered chains having terminal methyl groups with different orientations.[54;55]

According to the experimental data trends in **Figure 3.4**A, a SAM's reaction with atomic hydrogen accelerates as thiolates are removed from the surface. This implies that lower-density thiolate phases react more readily than close-packed molecules, in agreement with previous studies on octanethiolate SAMs which showed that reactivity is greater at defected sites such as grain boundaries and already-eroded regions.[35;37]

There are two different pathways through which the standing-up phase of a short-chain SAM can be consumed upon exposure to atomic hydrogen: the direct reaction of standing-up molecules (θ_S) with H-atoms, resulting in thiols leaving the surface (↑)

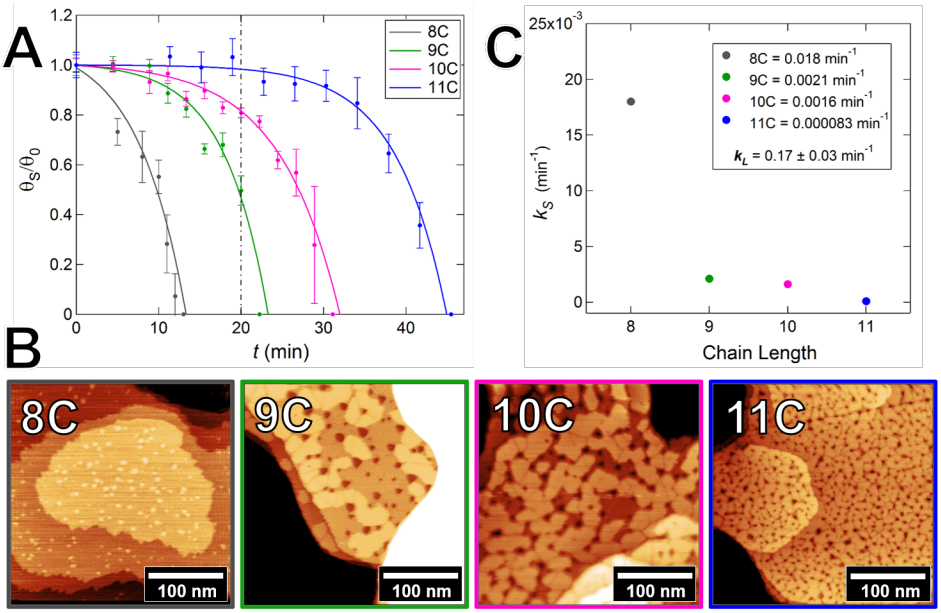

Figure 3.4: (A) Plot showing the fraction of standing-up phase coverage as a function of hydrogen exposure time. Each point is a weighted average of each sample's data collected at that time. Solid curves are fits produced using Equation 3.4, and all experimental exposure times have been normalized to the common control sample (10C) to obtain relative reaction rates. The vertical dashed line marks the time at which we obtained the images shown in (C). (B) Representative images (300 nm × 300 nm) of the 8C, 9C, 10C, and 11C SAMs after 20 min of hydrogen exposure. At this time, there is a wide range of standing-up coverage between the different SAMs: The 8C sample has no standing-up phase left, which is evidenced by the bright gold islands covering the surface, whereas the 11C sample shows little evidence of reactivity, given its thin grain boundaries and numerous, evenly spaced etch pits. (C) Plot of rate constants for all four alkanethiolates, illustrating the nonlinear decrease in k_S associated with small increases in the chain length.

$$\theta_S \xrightarrow{k_S} \uparrow \tag{3.1}$$

and the conversion of the standing-up phase into lower-density phases (θ_L),[15;47;49;53] which then proceed to react with H-atoms

$$\theta_S \xrightarrow{k_{SL}} \theta_L \xrightarrow{k_L} \uparrow \tag{3.2}$$

Given that the conversion of standing-up molecules to low-density phase is much faster than the reaction of low-density phase SAM with H-atoms ($k_{SL} \gg k_L$), we can express the rate of standing-up phase erosion as

$$\frac{d\theta}{dt} = -k_S\theta_S - k_L\theta_L = -k_S\theta_S - k_L(\theta_0 - \theta_S) \tag{3.3}$$

where θ_S is the surface fraction of standing-up phase ($0 \leq \theta_S \leq 1$), t is the hydrogen exposure time, k_S is the rate constant for hydrogen's reaction with the standing-up phase, and k_L defines the rate of hydrogen's reaction with low-density phases. The final variable, θ_0, corresponds to the surface fraction of the standing-up phase at t = 0; note that this value is not equal to 1, as we exclude any area corresponding to initial defect sites such as etch pits and grain boundaries. Note that we also assume $\theta_0 = \theta_S + \theta_L$ for all t, as the thiolates' mobility on the surface at room temperature allows the approximation that non-standing-up phase regions will always be covered in some form of low-density SAM rather than bare Au(111).[47;49;53] Therefore, according to our model, we can solve the above differential equation (**Equation 3.3**) and express θ_S as a function of t

$$\frac{\theta_S}{\theta_0} = Ae^{-(k_S - k_L)t} + \frac{1}{1 - \frac{k_S}{k_L}} \tag{3.4}$$

where $A = -\frac{k_S}{k_L}\left(\frac{1}{1-\frac{k_S}{k_L}}\right)$, a constant dependent on k_S and k_L.

When reacting with the standing-up phase, atomic hydrogen must pass through the tightly packed alkane tails to reach the reactive sulphur at the surface. We have previously shown[39] that longer alkane chains produce a monolayer that is both taller and has fewer dynamic fluctuations, thereby hindering a gas molecule's progress to the surface. This implies that k_S should be strongly and inversely dependent on alkanethiolate chain length.

When reacting with the low-density SAM phases, atomic hydrogen has little-to-no steric barrier before reaching the sulphur head of the thiolates. In these regions, the monolayer thickness is independent of chain length. The reactivity of such areas should therefore be uniform across all four samples, and k_L should be the same for all chain lengths.

The solid curves in **Figure 3.4**A represent the fitting of the experimental data to **Equation 3.4**, during which k_S and k_L remained free parameters. This process yielded k_S values ranging from 0.018 min^{-1} (8C) to 0.000083 min^{-1} (11C) and k_L values averaging at 0.17 ± 0.03 min^{-1}. Three major observations can be made based on these values. First, k_L varies minimally across chain lengths, a fact that agrees with our two-rate model and supports the proposal that k_L is independent of chain length. Second, $k_L \gg k_S$, which supports the expectation that regions covered with low-density phase are significantly more reactive than close-packed

domains. Finally, as shown in **Figure 3.4**C, k_S decreases considerably with each additional carbon in the alkanethiol chain, which shows that hydrogen's ability to permeate standing-up phase decreases rapidly with increased chain length, more so than would be expected from a simple increase in monolayer thickness. This implies that greater rigidity and packing in the longer chains' crystal lattice plays an active role in the passivation of the gold substrate. This conclusion is further supported by observations in previous studies[28;32;39;56] as well as the results of analogous experiments where we reacted 1H,1H,2H,2H-perfluorodecanethiolate SAMs with atomic hydrogen. Although this SAM is of comparable thickness to the 1-decanethiolate monolayer, its chemical functionalisation lends itself to a very different packing structure on the surface. Accordingly, the fluorinated SAM exhibited little-to-no reactivity after several hours of hydrogen exposure, unlike its hydrocarbon counterpart.

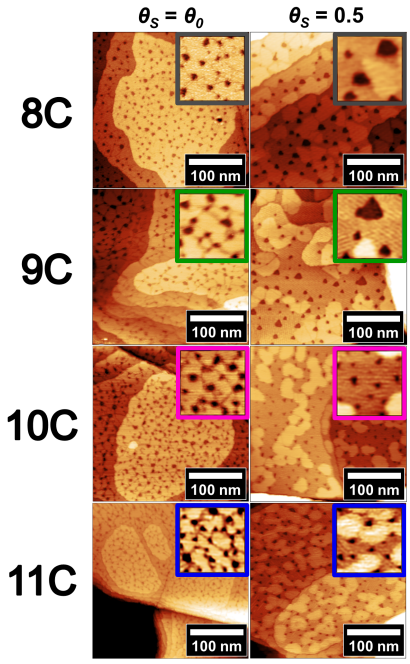

Figure 3.5: Representative 300 nm × 300 nm images of each alkanethiolate SAM (8C, 9C, 10C, and 11C) both prior to reaction and at $\theta_S = 0.5$. Square insets (50 nm × 50 nm) highlight the changes that we observe in etch pit morphology for each post-reaction sample. In the 8C and 9C samples, we find that the post-reaction etch pits are larger, fewer in number, and more triangular in their geometry compared to their initial counterparts. For the 10C and 11C samples, however, the etch pits are largely unchanged between the pre- and post-reaction samples; although their density across the surface decreases slightly, their small size and circular shape remain consistent.

As previously mentioned, a major advantage of using STM for this study is that the reactions can be explored on a molecular level rather than being restricted to statistical averages. **Figure**

3.5 shows visual comparisons of all four SAM chain lengths, both before and after exposure to atomic hydrogen. Prior to reaction, the size and density of domains and etch pits are similar across the four samples. However, differences in etch pit size and distribution become evident in the 8C and 9C samples at $\theta_S = 0.5$. For these shorter-chain monolayers, the etch pits grow larger, become more triangular, and decrease in density across the surface. Contrarily, the etch pits of the 10C and 11C samples do not exhibit any major changes at $\theta_S = 0.5$. This result is quantified in **Figure 3.6**, where the distribution of etch pit sizes is presented for all chain lengths, both before and after hydrogen exposure. The 8C and 9C distributions shift noticeably at $\theta_S = 0.5$, indicating that there is an increase in the mean etch pit area for these SAMs post-reaction. The 10C and 11C distributions, however, remain largely unchanged after hydrogen exposure.

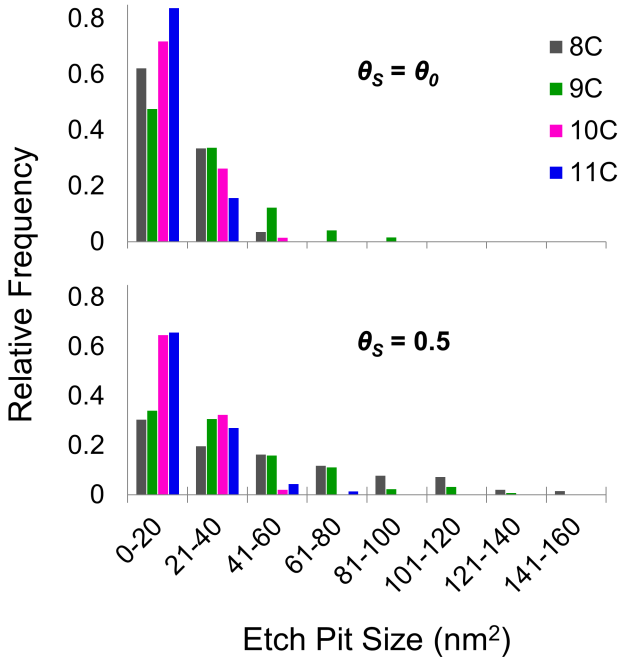

Figure 3.6: Histograms of etch pit areas for all four chain lengths prior to atomic hydrogen exposure (top) and at $\theta_S = 0.5$ (bottom). Shorter chain SAMs show a larger growth in mean etch pit area, with increases of 33, 12, 2, and 5 nm^2 for 8C, 9C, 10C, and 11C, respectively.

Previous studies[43;56;57] attribute this etch pit restructuring to increased mobility of gold surface atoms upon the formation of low-density SAM phases. They propose that the formation of fewer, larger etch pits is the result of Ostwald ripening. However, our results in **Figures 3.5** and **3.6** also suggest that the etch pits' degree of ripening depends strongly on thiolate chain length: 8C and 9C show the largest amount of gold substrate rearrangement, while 10C

and 11C exhibit minimal restructuring. We can explain this trend by noting that the longer the alkanethiolate SAM, the stronger the van der Waals forces between neighboring chains.[28] Greater intermolecular forces reduce the likelihood of longer SAMs forming 2D fluid phases, thereby lowering both thiol molecule and gold adatom mobility across the surface.

3.4 Conclusions

We have successfully used the direct-imaging capabilities of STM to show that the carbon chain length of an alkanethiolate SAM greatly impacts its reactivity with atomic hydrogen. First, our experimental data shows that areas of low thiol density on the surface are more susceptible to hydrogen attack than standing-up domains. Based on this observation, we have successfully described the kinetics of the reaction using a two-rate model: one rate constant for hydrogen reacting with the standing-up phase (which is chain length dependent) and the other for hydrogen reacting with low-density regions (which is the same for all chain lengths). This model describes the behaviour of all four chain lengths within statistical error and could be used to predict the behaviour of other alkanethiolate SAMs in the short-chain regime. Second, we found that small decreases in the film thickness lead to disproportionately large increases in the reaction rate. This implies that the packing structure and chain-length-dependent fluctuations of thiolate SAMs play an active role in the passivation of the underlying gold substrate. Finally, we found that the size, shape, and density of the SAMs' etch pits changed noticeably over the course of the reaction with hydrogen and that these changes depend on thiol chain length. The 10C and 11C samples exhibited minimal etch pit rearrangement, while there was significant growth in the mean etch pit size for the 8C and 9C SAMs. These reconstructions are attributed to Ostwald ripening, and we conclude that the weaker intermolecular forces between shorter-chain molecules permit greater mobility and dynamic fluctuations of thiols and their corresponding gold adatoms. These fluctuations therefore allow for more surface rearrangement. This STM study provides important insight into the passivation capabilities of organic thin films and how these abilities depend heavily on packing structure and dynamic disorder.

Chapter 4

Influence of Structural Dynamics on the Kinetics of Atomic Hydrogen Reactivity with Low-Temperature Alkanethiolate Self-Assembled Monolayers

This study examines the impact of surface temperature on alkanethiolate self-assembled monolayer (SAM) reactivity with atomic hydrogen (H) as well as how the combined effects of temperature and alkanethiol chain length alter the reaction outcome. This is achieved using ultrahigh vacuum scanning tunnelling microscopy (UHV-STM) to monitor the spatiotemporal evolution of the monolayer throughout the reaction. We find that with decreasing temperature, the reaction rate of alkanethiol SAMs with atomic H decreases monotonically. Furthermore, the kinetic profile of the low-temperature reaction differs from that at room temperature, indicating structural and dynamical fluctuations within the monolayer that influence reactivity. Chain length is also seen to significantly affect reactivity at reduced substrate temperature, with longer alkanethiols reacting more slowly than shorter ones. Finally, we observe a unique surface rearrangement of the SAM upon exposure to atomic H, including changes in the organisation of close-packed thiol domains and the evolution of gold adatom islands not observed at elevated temperatures. Overall, this work provides both quantitative and nanoscopic insight into how substrate temperature influences the structural dynamics of thiolate monolayers and how these fluctuations influence chemical reactivity.

4.1 Introduction

The ability to passivate a chemically active surface is of interest to many industrial sectors such as metallurgy and semiconductor manufacturing, as the functional lifetime of these materials depends heavily on slowing their degradation when they are exposed to a variety of reactive species. To this end, organic thin films demonstrate significant promise in their use as passivating coatings for metal and semiconductor surfaces. Thiolate self-assembled monolayers (SAMs), for example, have already been shown to provide significant resistance to chemical reactivity and corrosion on a variety of technologically relevant substrates.[59–66]

However, structural deviations often occur in these films under different environmental conditions, which can alter their physical and chemical properties and, in turn, impact their passivation abilities. For example, many pioneering studies on alkanethiolate SAMs on Au(111), both theoretical[67–70] and experimental,[71–73] show that these films are subject to temperature-dependent tilt-order phase transformations due to their canted assembly on the surface. These include both low-temperature transitions ($T < 300$ K) between two ordered phases of differing tilt angles, and high-temperature transitions ($T > 300$ K) between ordered, crystalline phases and phases characterised by disordered molecular fluctuations. Further studies also illustrate that the surface structure and packing density of alkanethiolate SAMs influence the energy-transfer dynamics that occur between a monolayer and gas-phase particles that collide with it.[74;75] A thorough understanding of how structural changes impact surface reactivity is hence crucial in advancing the implementation of functional thin films in real-world applications.

The well-characterised and highly ordered polycrystalline structure of thiolate SAMs, in addition to their vast chemical versatility, provides a unique platform for studying the dynamics between environmental conditions and chemical reactivity of organic thin films.[16;30;76;77] Several groups have employed spectroscopic techniques such as X-ray photoelectron spectroscopy[78] and reflection absorption infrared spectroscopy[39] to examine how surface temperature influences the film structure and reactivity of SAMs with O(^{3}P). Previous work has also utilised a combination of spectroscopies to explore the impact of substrate temperature on alkanethiolate interactions with X-ray irradiation.[79]

To gain an accurate understanding of how these temperature-dependent thin film dynamics

evolve on the nanoscale, however, we must use a more localised experimental technique such as scanning probe microscopy (SPM). SPM allows us to better investigate kinetic events on the molecular level, rather than being limited to averaged information from the entire reactive surface. This work therefore uses ultrahigh vacuum scanning tunnelling microscopy (UHV-STM) to investigate the localised impact of substrate temperature and alkanethiol chain length on self-assembled monolayer reactivity. First, we track the reaction progression of 1-decanethiolate (10C) SAMs exposed to atomic hydrogen (H) at substrate temperatures T_S = 295, 270, 250, and 130 K by monitoring the close-packed thiol surface coverage. Using our previously developed rate model,[13] we describe the reaction kinetics and deduce the rate constants for the reaction at each temperature. Furthermore, we compare the reactivity of 1-octanethiolate (8C) and 10C SAMs at low temperature (250 K) to reveal the combined effects of reduced T_S and shorter chain length on reaction kinetics with atomic H. Finally, we examine the impact of substrate temperature on the SAMs' surface rearrangement during their reaction with atomic H. This paper provides significant insight into the relationship between substrate temperature and the resultant chemical activity of organic thin films upon exposure to energetic species such as atomic H. In particular, it emphasises how structural fluctuations in the film influence its reactivity as a function of temperature.

4.2 Experimental Section

Experiments were performed in the UHV microscope chamber described in **Section 2.1**, and using the MGC-75 gas cracker introduced in **Section 2.4**. Sample cooling is achieved using the methods outlined in **Section 2.3**, and thiolate SAMs were prepared according to the procedure written in **Section 2.5.1**.

All STM images are taken with a +0.70 V bias on the sample and a tunnelling current setpoint of 10 pA. Previous control experiments with 10C SAMs confirm that exposure to atomic H is uniform across the entire substrate and that there are no noticeable differences in reactivity due to variations in Au(111) surface structure or SAM domain orientation for this reaction.[13] Finally, we perform all of our STM image processing using Gwyddion, an open-source software for SPM data analysis.[11]

4.3 Results and Discussion

It is well-documented in previous studies[28] that the primary reaction mechanism of atomic H with short-chain alkanethiolate SAMs (C $\leq$ 12) is through the cleavage of the sulphur-gold bonds, thereby removing entire thiols from the surface. This reactivity, as shown in our reaction of an 8C SAM in **Figure 4.1**, initially appears around the thiolate domain grain boundaries and subsequently expands outward, in agreement with previous results.[13;33–37] The removal of thiolate molecules promotes the formation of various low-density phases, including both ordered lying-down, or striped, phases and disordered 2D fluids.[15;47;49;53] These low-density regions continue to grow as the reaction proceeds, consuming the hexagonal close-packed (ϕ-phase) domains until only low-density alkanethiol and gold adatom islands[13;33;34] remain. We consider the reaction to be complete when no ϕ-phase SAM is left on the Au(111) surface.[13] The bottom row of **Figure 4.1** illustrates the image processing procedure used to quantify the ϕ-phase coverage at any point in the reaction, where all low-density SAM regions are masked in blue to allow the computation of the unreacted area.

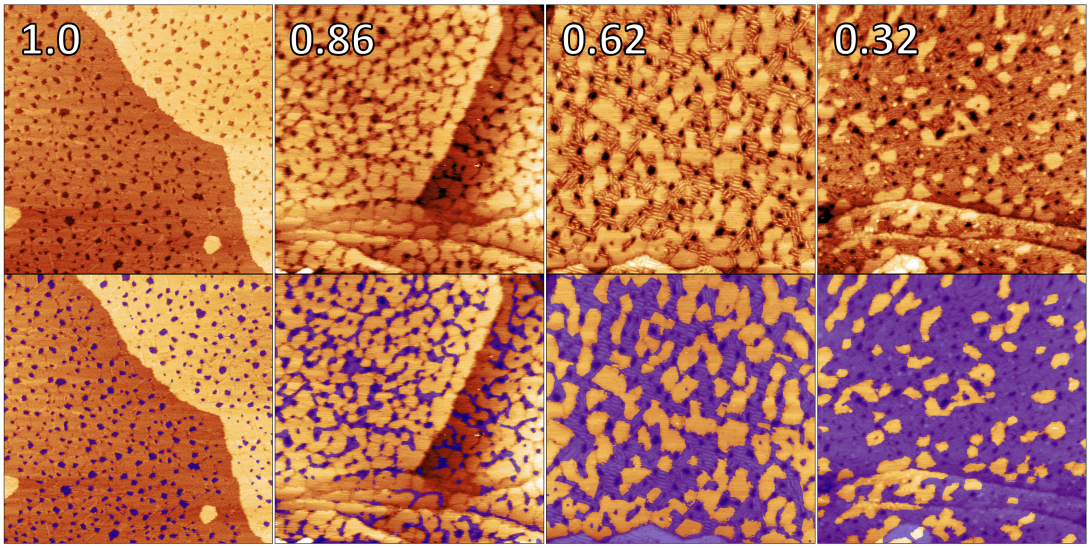

Figure 4.1: Representative STM image progression (200 nm $\times$ 200 nm) of a 1-octanethiolate (8C) SAM as it reacts with atomic H at 250 K. Top row: STM images showing ϕ-phase coverages of 100%, 86%, 62%, and 32%. Regions of low-density SAM first appear around the domain boundaries at 86% coverage, with low-density striped phase clearly visible beginning at 62% coverage. Bottom row: examples of the image processing procedure used to quantify the ϕ-phase coverage for each of the images in the top row, with the low-density SAM regions marked in blue and the ϕ-phase domains in orange. Note that initial defect sites such as etch pits and grain boundaries are always masked.

The results of our study are divided into three parts. First, we present the reaction of 1-decanethiolate (10C) SAMs at decreased substrate temperatures and discuss the validity of our previously developed kinetic model[13] for $T_S \neq 295$ K. Second, we examine the effect of chain length on low temperature alkanethiolate reactivity by comparing the reaction rates of 8C and 10C SAMs at both T_S = 295 and 250 K. Finally, we analyse the impact of T_S on nanoscale alkanethiolate surface rearrangement, with particular emphasis on the restructuring of ϕ-phase domains and gold adatom islands at low temperature.

4.3.1 1-Decanethiolate (10C) Reactivity at Various T_S

To understand the impact of reduced temperature on alkanethiolate SAM reactivity with atomic H, we tracked the reaction progression of 10C SAMs at T_S = 295, 270, 250, and 130 K. These results are presented in **Figure 4.2**A, where the area fraction of ϕ-phase SAM is plotted as a function of hydrogen exposure time. The rate of a 10C SAM's reaction with atomic H decreases with decreased temperature, with the lowest temperature of T_S = 130 K showing no measurable reaction. This trend in reactivity in relation to T_S is in agreement with previous work[39;78;79] and is visually represented in **Figure 4.2**B, where the STM images of 10C SAMs are presented for the same atomic H exposure at different surface temperatures. The experimental data in **Figure 4.2**A were fitted to our previously developed model, which successfully describes the reactivity of alkanethiolate SAMs of different lengths at room temperature[13]

$$\frac{\theta_S}{\theta_0} = A\mathrm{e}^{-(k_S-k_L)t} + \frac{1}{1-\frac{k_s}{k_L}} \tag{4.1}$$

where $\frac{\theta_S}{\theta_0}$ is the normalized area fraction of ϕ-phase SAM, t is the hydrogen exposure time, k_S is the rate constant for hydrogen's reaction with the ϕ-phase, k_L defines the rate of hydrogen's reaction with low-density phases, and A is a constant dependent on k_S and k_L. This two-rate model builds on previously proposed theory[80] and assumes that the reaction of thiols with atomic H occurs one of two ways: (a) the slow reaction of sterically hindered close-packed thiols or (b) the fast reaction of easily accessible edge-site and/or low-density thiols. Calculated reaction probabilities based on the atomic H flux and time-dependent SAM densities also provide further support for our two-rate model. At T_S = 295 K, a 10C SAM has $\sim$30% reaction

probability for $\frac{\theta_S}{\theta_0} = 0.95$, which increases to a ~90% reaction probability once there is greater low-density thiol coverage and $\frac{\theta_S}{\theta_0} = 0.60$.

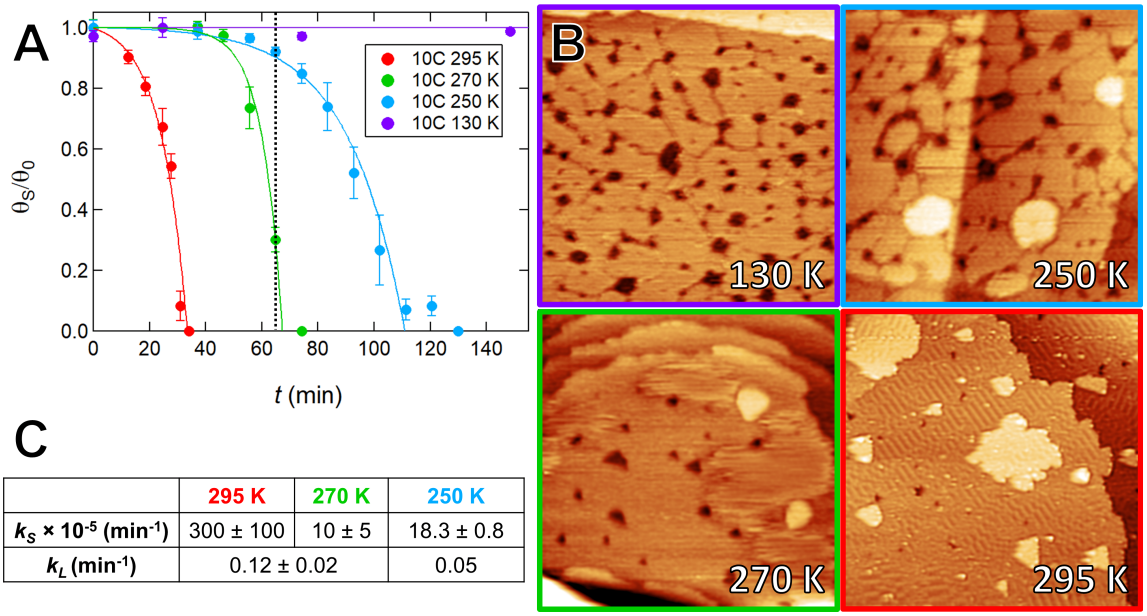

C

	295 K	270 K	250 K
$k_S \times 10^{-5}$ (min^{-1})	300 ± 100	10 ± 5	18.3 ± 0.8
k_L (min^{-1})	0.12 ± 0.02		0.05

Figure 4.2: (A) Plot showing the fraction of 1-decanethiolate (10C) SAM ϕ-phase coverage as a function of atomic H exposure time, at four different temperatures and under constant atomic H flux. Each point is a weighted average of the data collected for the sample at that time, and we performed multiple experimental runs to confirm the validity of the trajectories. Solid curves are fits produced using **Equation 4.1**, and the vertical dashed line marks the time at which we obtained the images in (B). (B) Representative images (150 nm × 150 nm) of 10C SAMs at 130, 250, 270, and 295 K after 64 min of atomic H exposure. At this time point, we observe a wide range of temperature-dependent reactivity: the SAM at 130 K shows little-to-no reactivity (thin grain boundaries with numerous evenly distributed etch pits), whereas the SAM at 295 K is fully reacted (covered in striped low-density phase and covered in bright gold islands). (C) Table of rate constants produced by **Equation 4.1** for all four reaction temperatures. Although the two-rate model appears to adequately describe the reaction at 295 and 270 K, there is breakdown at 250 K, as evidenced by a significantly lower value for k_L.

Both the fitted curves in **Figure 4.2**A and the rate constants in **Figure 4.2**C show that the two-rate model describes the experimental data well for T_S = 295 and 270 K. Three key statements about the impact of temperature on the reaction can be made following this analysis: First, k_L varies minimally between the two temperatures, which implies that the lying-down phase is equally reactive under both conditions, and thus the reactions likely follow similar mechanisms. Second, $k_L \gg k_S$, which once again suggests that low-density phase thiols are significantly more reactive than ϕ-phase thiols, regardless of temperature. Finally, k_S decreases for colder samples, which confirms that atomic H's ability to permeate the ϕ-phase domains is greatly reduced due to increased SAM crystallinity at lower temperature.[39;67–69;72;79]

However, the proposed two-rate model disagrees with the experimental data for $T_S \leq 250$ K. As shown in **Figure 4.2**A, there is a modest divergence of the model fit from the experimental data at longer atomic H exposure times. Unlike the reactions at T_S = 295 and 270 K, which accelerate continuously after their incubation periods, the reaction at T_S = 250 K appears to slow down as it approaches completion. This observation is a direct consequence of lingering ϕ-phase domains on the surface near the end of the reaction and is reflected in the calculated reaction probabilities for a 10C SAM at T_S = 250 K. For $\frac{\theta_S}{\theta_0}$ = 0.63, the reaction probability is at its peak of ∼31%; however, for $\frac{\theta_S}{\theta_0}$ = 0.17, it drops to ∼18% and continues to decrease until the end of the reaction. Sigmoidal profiles like these are commonly observed in systems governed by the Avrami equation, where the reaction begins slowly, accelerates when multiple nucleation centers are available to react simultaneously, and then decelerates once the amount of available reactant becomes minimal. In our experiment, we propose that the final deceleration occurs when the ϕ-phase domains approach the minimum size for thermodynamic stability, but there is not yet enough available surface area for all of the ϕ-phase to convert into lower-density striped phases. This phenomenon is more probable at lower temperature because the thiols are less mobile on the Au(111) surface, which prohibits the ϕ-phase from coalescing into larger and more stable domains.[49;57] Previous work supports this proposal, using the Avrami theorem as a basis to describe both the formation process of a self-assembled monolayer from solution[81] and the reductive desorption of alkanethiols from an Au(111) surface.[82]

The change in experimentally observed reactivity at T_S = 250 K supports the conclusions drawn by past molecular dynamics studies,[67–69] which state that alkanethiolate SAMs undergo distinct structural phase transitions at specific temperatures. At T_S = 150 K, thiolate SAMs form highly ordered solid films with all molecules tilted unidirectionally at $\sim 34^\circ$ from surface normal[72] and rotational motion fully prohibited. Conversely, at $T_S \geq 300$ K the collective tilt angle becomes diffuse, and the molecular fluctuations increase significantly. However, for 250 K $\leq T_S \leq$ 300 K, there exists an intermediate phase where although crystalline order is largely maintained, molecular fluctuations appear in the individual molecules' tilt directions. This suggests that our observed difference in reactivity at T_S = 250 K compared to T_S = 270 and 295 K can be explained by differences in the monolayer's temperature-dependent dynamic disorder and the degree of molecular fluctuations experienced, which in turn influence atomic H mobility

through the film.

4.3.2 Effect of Chain Length on Low-Temperature Alkanethiolate Reactivity

We also investigated how the chain length dependence of alkanethiolate reactivity is affected at low T_S by comparing the reaction progression of 8C and 10C SAMs at T_S = 295 and 250 K. **Figure 4.3**A plots the area fraction of ϕ-phase SAM as a function of hydrogen exposure time, and the experimental data are fitted to **Equation 4.1**. We find that the shorter SAM reacts with atomic H more quickly than the longer SAM because longer alkanethiolate chains exhibit a more crystalline packing structure and are thus less penetrable to atomic H.[28;43;83] This observation is true at both experimental temperatures, and the rate constants for each fit are tabulated in **Figure 4.3**B.

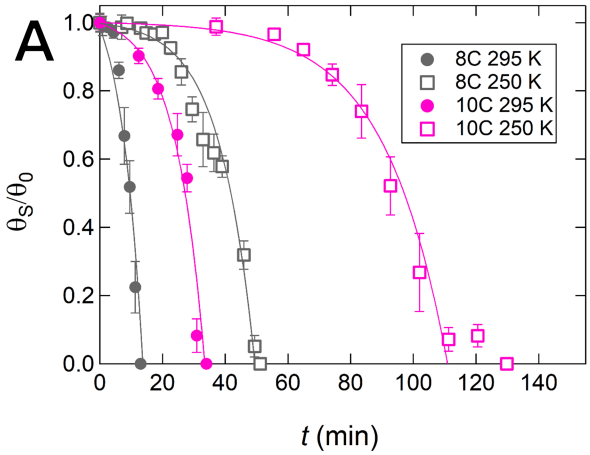

B

295 K ●

	8C	10C
$k_S \times 10^{-5}$ (min^{-1})	2200 ± 200	300 ± 100
k_L (min^{-1})	0.13 ± 0.03	

250 K □

	8C	10C
$k_S \times 10^{-5}$ (min^{-1})	89 ± 3	18.3 ± 0.8
k_L (min^{-1})	0.07 ± 0.02	

Figure 4.3: (A) Plot showing the fraction of ϕ-phase coverage as a function of atomic H exposure time for 8C and 10C SAMs at 295 and 250 K. Each point is a weighted average of the data collected for the sample at that time, and solid curves are fits produced using **Equation 4.1**. (B) Tabulated rate constants produced by **Equation 4.1** for 8C and 10C SAMs at 295 and 250 K. We note that k_L's independence of chain length appears to persist even at low temperature.

Both the 8C and 10C SAMs exhibit a similar decrease of 95% in relative reaction rate at T_S = 250 K compared to T_S = 295 K. This suggests that although the SAMs' reaction with atomic H is chain-length-dependent across multiple substrate temperatures, any changes in alkanethiolate packing due to reduced T_S are comparable for 8C and 10C SAMs. Although some previous studies[39] show that lowering T_S yields a more severe relative decrease in reactivity for longer-chain thiols, we suspect that this difference only manifests when comparing SAMs across different chain length regimes. Because both 8C and 10C SAMs are classified as short-chain

alkanethiols (C $\leq$ 12),[28] as determined by their tilt structure,[73] we expect the temperature dependences of their packing behavior and reactivity to be relatively similar.

4.3.3 Impact of T_S on Nanoscale Alkanethiolate Surface Rearrangement

Finally, we use the nanoscale imaging capabilities of STM to analyse chain-length-dependent surface rearrangements[13] at low T_S during reaction with atomic H. These temperature-dependent differences in surface morphology result in the rearrangement of ϕ-phase domains and etch pits and the evolution of gold adatom islands.

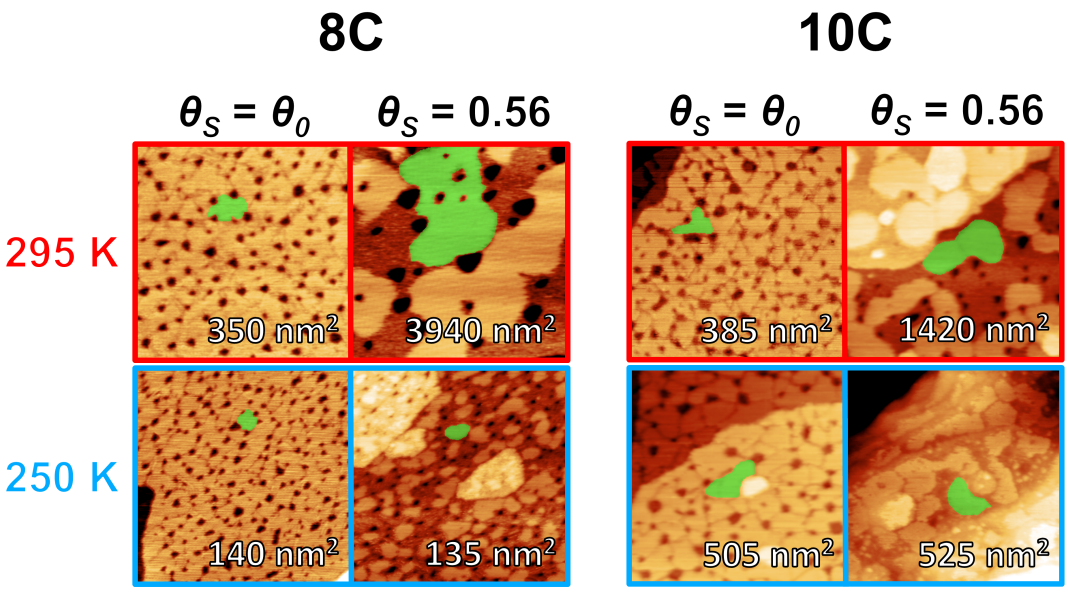

Figure 4.4: STM images (150 nm $\times$ 150 nm) of 8C and 10C SAMs at T_S = 295 and 250 K, both prior to reaction and at $\theta_S = 0.56$. Each image shows a representative ϕ-phase domain highlighted in green as well as the average ϕ-phase domain size for that chain length, temperature, and surface coverage in the bottom right-hand corner. At T_S = 295 K, the average ϕ-phase domain size increases as the reaction progresses, with the 8C sample exhibiting greater rearrangement than the 10C sample. At T_S = 250 K, however, the ϕ-phase domains remain approximately the same size following exposure to atomic H. This phenomenon is attributed to the freezing of lateral molecular movement, which would typically be thermodynamically favorable, at reduced temperature.

First, **Figure 4.4** presents STM images at both $\theta_S = \theta_0$ and $\theta_S = 0.56$ and demonstrates how the ϕ-phase domains of 8C and 10C SAMs evolve during the course of reaction at T_S = 295 and 250 K. At room temperature, we observe the anticipated Ostwald ripening of the close-packed thiols and etch pits,[13] with the 8C sample exhibiting greater rearrangement than the 10C sample. The chain length dependence of the monolayer restructuring is attributed to the van der Waals forces between neighbouring alkanethiol molecules; the shorter the molecule,

the weaker the intermolecular forces within the film[28] and therefore the greater the molecular mobility on the Au(111) surface. At T_S = 250 K, however, neither 8C nor 10C SAMs exhibit a statistically significant difference in their average ϕ-phase domain size when comparing $\theta_S = \theta_0$ to $\theta_S = 0.56$; that is, at low temperature, the ϕ-phase domains of alkanethiolate SAMs remain approximately the same size throughout their reaction with atomic H, as illustrated by the domains highlighted in green in **Figure 4.4**. We propose that this lack of surface rearrangement at T_S = 250 K is due to the thiols' reduced mobility at colder temperatures; the lower temperature prohibits molecular movement that would otherwise result in the formation of larger and more thermodynamically favorable domains.[49;57] Such temperature-dependent differences in ϕ-phase domain organisation may also impact the macroscopic surface properties produced by the alkanethiolate SAMs, including wettability, conductivity in the direction of surface normal, and passivation capabilities.

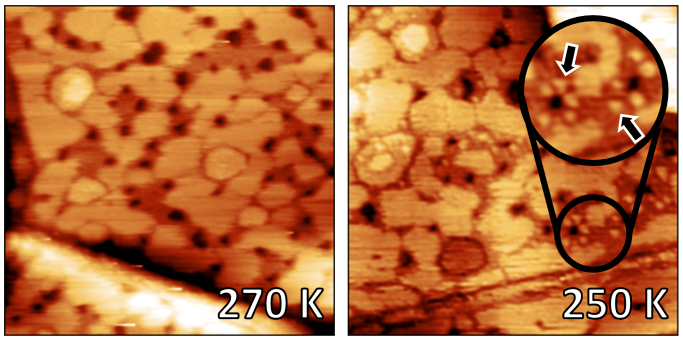

Figure 4.5: STM images (150 nm × 150 nm) of 10C SAMs with θ_S = 0.74 ϕ-phase coverage at 270 and 250 K. At 270 K, we observe the typical reaction progression: a widening of grain boundaries around the close-packed thiol domains. However, at 250 K, we notice the appearance of gold islands (see features highlighted in inset) within the low-density thiol regions, despite there still being ϕ-phase on the surface. This phenomenon occurred for both 10C and 8C SAMs at 250 K.

Finally, the temperature dependence of gold adatom island formation following the SAMs' exposure to atomic H is shown in **Figure 4.5**. During experiments performed at T_S = 295 K, gold islands appear exclusively at the end of the reaction; their appearance signals that the reaction with atomic H is complete and that no ϕ-phase SAM remains on the surface. This observation is also true for SAMs exposed to atomic H at T_S = 270 K. However, at T_S = 250 K, the gold islands appear gradually throughout the reaction, even while close-packed thiols are still present on the Au(111) surface. We propose that the slow growth of gold islands is partially due to the reduced mobility of thiols on the Au(111) surface at low temperature, although it is interesting to note

that the Kandel group has also recently reported on similar reaction-induced surface evolution at higher temperatures than our results.[84] This suggests that other factors likely impact the rate of gold adatom growth, such as atomic H flux and overall reaction speed.

4.4 Conclusions

We use STM to demonstrate that the temperature of alkanethiolate SAMs significantly impacts their reactivity with atomic H, in terms of both kinetics and surface reconstruction. First, our experimental data show that SAMs react more slowly as temperature decreases, and all reactivity can be eliminated at sufficiently low T_S. For slightly decreased temperatures (T_S = 270 K), the reaction kinetics are well-described using our previously developed two-rate model.[13] However, at T_S = 250 K, our proposed model diverges from the experimental data, likely due to a structural phase transition in the alkanethiol monolayer[67–69] which decreases the degree of molecular fluctuations experienced and, hence, hinders the mobility of atomic H through the SAM. Second, we find that shorter SAMs react with atomic H more quickly than longer SAMs due to increased dynamical fluctuations caused by their weaker interchain attractions,[28;43;83] and that this is true at both T_S = 295 and 250 K. Furthermore, 8C and 10C SAMs exhibit a similar decrease of 95% in relative reaction rate at T_S = 250 K compared to T_S = 295 K. These conclusions imply that although the SAMs' reaction with atomic H is chain-length-dependent at any given substrate temperature, changes in alkanethiolate packing due to reduced T_S are comparable for octanethiolate and decanethiolate SAMs. Finally, we observe nanoscale differences in the reaction-induced structural rearrangement of the alkanethiolate monolayers at T_S = 295 K compared to T_S = 250 K. At room temperature, the ϕ-phase domains undergo Ostwald ripening during their reaction with atomic H, with the 8C sample exhibiting greater rearrangement than the 10C sample. However, at T_S = 250 K, the average ϕ-phase domain size remains approximately unchanged following exposure to atomic H, for both the 8C and 10C SAMs. This lack of surface rearrangement is attributed to the reduced molecular motion of thiols across the surface at colder temperatures. Additionally, we observe a temperature dependence in the formation of gold adatom islands during the SAMs' reactions with atomic H. At room temperature, the adatoms appear abruptly after the ϕ-phase domains are gone;

however, at T_S = 250 K, the adatoms grow slowly throughout the course of the reaction. We propose that this slow growth of gold islands is partially due to the reduced mobility of thiols on the Au(111) surface at low temperature, although it is also likely impacted by other factors such as atomic H flux and overall reaction speed. This STM study therefore yields important insight into temperature-dependent structural changes that occur in organic thin films, as well as how these rearrangements influence the films' chemical reactivity and passivation capabilities.

Chapter 5

Temperature-Dependent Structures of 2D Metal-Organic Frameworks on Au(111)

This chapter presents work done in collaboration with the Park Group (University of Chicago). Broadly, this study discusses the large-scale synthesis of high-quality thin films with extensive tunability derived from molecular building blocks. The Park Group reports the synthesis of two-dimensional (2D) porphyrin polymer films with wafer-scale homogeneity in the ultimate limit of monolayer thickness by growing films at a sharp pentane/water interface, which allows the fabrication of their hybrid superlattices. Laminar assembly polymerisation of porphyrin monomers could form monolayers of metal-organic frameworks with Cu^{2+} linkers or covalent organic frameworks with terephthalaldehyde linkers. Both the lattice structures and optical properties of these 2D films were directly controlled by the molecular monomers and polymerisation chemistries. The 2D polymers were used to fabricate arrays of hybrid superlattices with molybdenum disulphide that could be used in electrical capacitors.

My role in this project was to confirm the films' lattice structure and crystallinity using scanning tunnelling microscopy (STM), which I achieved for one of the metal-organic framework (MOF) films. I also investigated the impact of thermal annealing on the film structure, and how post-anneal cooling rates affect the MOF's ordering. For the full published manuscript written about this work, please refer to **Appendix D**.

5.1 Introduction

Monolayer two-dimensional polymers (2DPs), which are one-molecule-thick, freestanding films composed of periodically linked monomers,[86–89] offer an ideal material system with two key advantages. First, their properties can be tuned at the molecular level by using different monomers and polymerisation chemistries.[90;91] Second, as the molecular analogs of 2D atomic crystals (e.g. graphene and transition metal dichalcogenides (TMDs)),[92–94] 2DPs can be assembled through van der Waals (vdW) interactions into heterostructures and superlattices, layer by layer. vdW heterostructures generated from 2D atomic crystals have produced properties not observed in individual building blocks.[95;96] Adding the chemical tunability of the 2DPs to such vdW heterostructures will lead to the properties and functionalities designed at the molecular level and further tuned by the interlayer interactions. However, it has remained an unmet challenge to scalably synthesise monolayer 2DP films and subsequently integrate them with other materials with monolayer precision.[97;98] This is due to the difficulty of controlling reactions in the monolayer limit with large-scale uniformity and to the lack of facile methods for the transfer and integration of monolayer 2DPs because of their fragility. Previous experiments have reported progress toward large-scale synthesis of 2DPs[99–107] but with limited success with regard to wafer-scale homogeneity, microscopic characterisation of crystalline structures, and scalable thin-film integration.[108]

Overall, this work presents the wafer-scale synthesis and integration of monolayer 2DPs for the fabrication of their hybrid heterostructures with monolayer precision. It includes the development of an interfacial synthesis technique, laminar assembly polymerisation (LAP), that is compatible with various other molecular building blocks and two primary polymerisation chemistries (coordination and covalent). This synthesis approach incorporated key features necessary for scalable and facile processing, as well as the fabrication of superlattices based on monolayer 2DPs and 2D atomic crystals.

The design approach for the 2DP monolayers was based on porphyrin building blocks. These molecules had two variation sites: one at the center of the porphyrin ring (**M** = 2H, Fe(III), or Pt(II)) that tuned the optical spectra and the other on the phenyl groups (**R** = -COOH or -NH_2) that controlled the monomer-monomer bonds. The monomers were cross-linked either through

coordination bonds via a copper paddle wheel structure in the presence of Cu^{2+} ions or through covalent bonds via the Schiff base reaction in the presence of terephthalaldehyde (TPA).[106] The former forms coordination 2DPs (2DP I-III, **M** = 2H, Pt^{2+}, or Fe^{3+}, respectively), also known as monolayer metal-organic frameworks (MOFs), whereas the latter forms covalent 2DPs (2DP IV, **M** = 2H), also known as monolayer covalent organic frameworks (COFs).

Although the Park Group's primary focus in this study was their novel synthsis method and characterisation of the product, this chapter will focus on my contributions to the project, namely the STM imaging of 2DP II (**M** = Pt^{2+}) and the evaluation of the impact of thermal annealing on the film's crystalline structure.

5.2 Experimental Section

The full synthesis of the 2DPs can be found in **Appendix D**. For the purposes of STM imaging, the 2DP II monolayer was deposited onto a hydrogen flame-annealed thin film of Au(111)-on-mica from Keysight Technologies. Samples were rinsed with hexanes, methanol and isopropyl alcohol (IPA) to remove any surface residue, and were then dried with nitrogen. Sample placement into the load lock (**Section 2.1**) occurred within one hour of preparation, and film integrity was confirmed to last multiple weeks at room temperature in the microscope chamber. All STM images were taken with a bias voltage of -1.50 V and a tunnelling current set point of 10 pA. Sample annealing was performed using the temperature control setup described in **Section 2.3**.

5.3 Results and Discussion

The results of these experiments are divided into two sections. First, I will discuss the basic STM imaging of 2DP II, and elaborate briefly on the characterisation included in the final publication of this project. Second, however, I will explore the temperature-dependent structural dynamics of the film which were (somewhat accidentally) discovered while attempting to flatten the film in the interest of obtaining higher quality STM images. This data was not included in the final paper, and is published here for the first time.

5.3.1 Scanning Tunnelling Microscopy (STM) of 2D Metal-Organic Frameworks (MOFs)

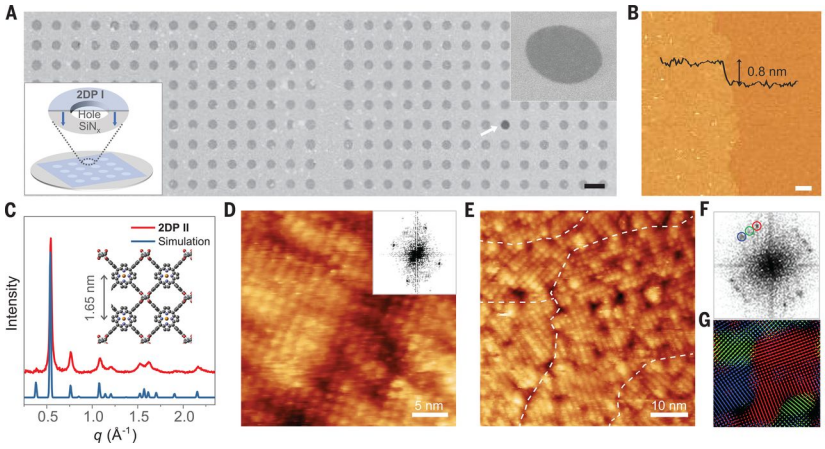

Figure 5.1: Structural characterisations of 2DPs. (A) SEM image of monolayer 2DP I on a holey silicon nitride TEM grid. The white arrow indicates a hole not covered by monolayer 2DP I. Scale bar, 5 μm. (Bottom left inset) Schematic of monolayer 2DP I suspended over a hole on a silicon nitride TEM grid. (Top right inset) Magnified SEM image of monolayer 2DP I suspended over a 2 μm hole. (B) AFM height image of monolayer 2DP I. Scale bar, 500 nm. (Inset) AFM height profile. (C) Experimental and calculated in-plane XRD profiles for 2DP II. The experiment was conducted on a stacked 2DP II of 147 layers on sapphire. (Inset) Crystal structure of 2DP II. (D) Constant-current STM topography image of a single-crystalline domain of monolayer 2DP II on a thin film of Au(111)-on-mica. (Inset) 2D FFT of the image. (E) Constant-current STM topography image of multiple crystalline domains of monolayer 2DP II. Boundaries between different domains are manually identified by the white dashed line. (F) 2D FFT of (E) showing square lattices of three major orientations. (G) Colour-coded inverse 2D FFT image generated using the three sets of square lattice spots in (F). One spot from each set is circled with the corresponding colour in (F).

The published structural characterisation of the 2DPs can be found in **Figure 5.1**. We chose STM as one of the characterisation techniques for 2DP II with the goal of confirming three characteristics about the film: coverage, crystallinity, and domain size/structure. Typically, the STM topography images displayed full surface coverage with a polycrystalline structure (**Figure 5.1**D-G), similar to previously-imaged 2DPs.[109;110] The domain size falls between 10-40 nm in diameter, which is consistent with complimentary synchrotron grazing incidence X-ray diffraction (GIXRD) (average domain diameter $\sim$ 20 nm). Finally, the STM images indicate that 2DP II assembles in a square lattice with a lattice constant of a = 1.66 $\pm$ 0.03 nm, which is once again consistent with GIXRD measurements (a = 1.64 nm) (**Figure 5.1**C). One piece of information about the 2DP II film that remained elusive, however, was the structure of the polycrystalline domain boundaries. Although atomic force microscopy (AFM) images show

a relatively flat surface on the micron scale (**Figure 5.1**B), the STM images indicate wrinkling in the film so severe that it masks the underlying terrace structure of the Au(111) substrate. The nature of this effect remains unclear, though we speculate that it is caused by the slightly buckled structure of the 2DP II itself.

5.3.2 Dependence of 2D MOF Structures on Post-Anneal Cooling Rates

In an attempt to flatten the 2DP II films and decipher the domain boundary structure, we proceeded with a variety of annealing experiments up to 370 K. We chose this temperature to ensure the safety of the 2DP II layer, which should be stable and free from degradation up to $\sim$ 473 K in air. After each anneal, we allowed the sample to cool down to room temperature before imaging.

Figure 5.2A shows an STM image of a 2DP II film after the first anneal attempt. This sample was heated to 370 K, annealed for 10 min, and then cooled rapidly with LN2 after the heater was turned off. The result was a 2DP II film that appears flatter than its non-annealed counterpart, as evidenced by the ability to resolve the Au(111) terrace structure beneath the monolayer. However, as highlighted in **Figure 5.2**B, this annealing procedure also interrupted the crystallinity of the MOF; that is, while some regions still exhibit a square lattice structure, others have been distorted into hexagonal patterns.

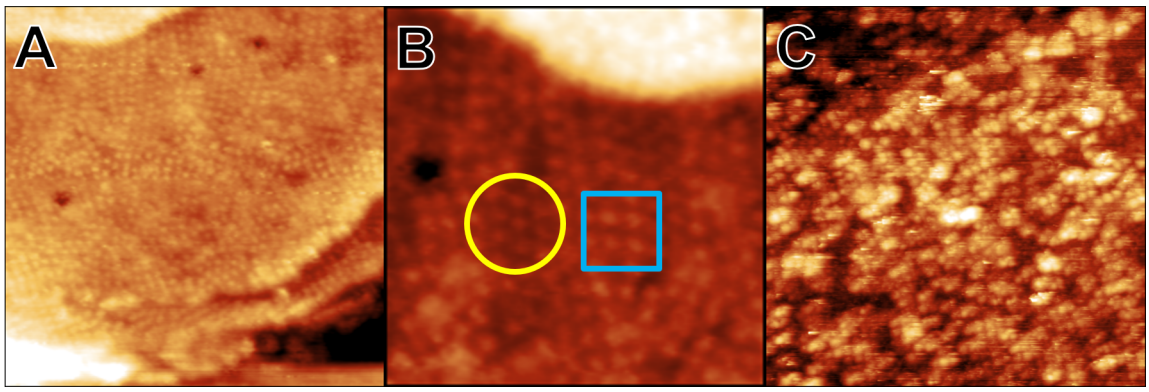

Figure 5.2: (A) STM image (60 nm $\times$ 60 nm) of a 2DP II film post-anneal at 370 K, followed by rapid cooling with LN2. The annealing procedure appears to have flattened the film, at the expense of its crystallinity. (B) Zoomed in STM image of the sample in (A), showing the coexistance of both square (blue square) and hexagonal (yellow circle) molecular alignments. (C) STM image (60 nm $\times$ 60 nm) of a 2DP II film post-anneal at 370 K, followed by slow cooling. This procedure yielded a 2DP II film much more similar to those imaged without any annealing.

The second attempted annealing procedure saw the sample heated to 370 K, annealed for

10 min, and then cooled slowly *without* LN2. An STM image of the resulting film is shown in **Figure 5.2**C. This procedure yielded a 2DP II film much more similar to those imaged without any annealing; the surface appears wrinkled, without any resolution of the underlying substrate, but the lattice structure is very clearly square and (poly)crystalline. The above results were highly reproducible, even when subsequent annealing procedures were performed on the same sample (*e.g.* a rapid cooling anneal would always result in a flattened, distorted lattice, even if it was preceeded by multiple slow cooling anneals). Furthermore, lower annealing temperatures and longer annealing times did not alter the results for any of the sample that were cooled slowly post-anneal.

We therefore propose that the main factor in determining the film's post-anneal structure is the post-anneal cooling rate. Given that our annealing temperatures are well below the degredation temperature of 2DP II, and that different results were observed for the same annealing temperature if the cooling rates were different, we suspect that the heating procedure stretches the bonds of the MOF beyond their room temperature equilibrium length without irreversibly damaging them. Then, upon cooling, the bonds either have time to relax back to their room temperature equilibrium (slow cool) or they are kinetically trapped in a non-crystalline metastable state (rapid cool). Further investigations into this phenomenon were cut short due to a lack of 2DP II samples, but some interesting questions that remain are: (1) How low of an annealing temperature will distort the lattice structure if paired with a rapid cooling rate? and (2) Is the lattice distortion reversible? That is, if the film is trapped in its non-crystalline metastable state, can its crystallinity be restored by subjecting it to an anneal followed by slow cooling?

5.4 Conclusions

This chapter describes an exciting and novel wafer-scale synthesis of 2DPs that shows promise for the future production of large-scale 2D materials. STM, alongside other surface characterisation techniques, reveals one of these 2DPs (2DP II) to have a polycrystalline square lattice structure with high surface coverage. The film as deposited on an Au(111) surface, however, exhibits wrinkling likely caused by the buckled structure of the monolayer itself. Attempts to flatten the

film via thermal annealing revealed unexpected dynamic behaviour when subject to different post-anneal cooling rates. This phenomenon raises questions about the potential applications for such films, including the impact of the loss of crystallinity within a device under certain environmental conditions, and new possible functions related to the system being able to reversibly switch between amorphous and crystalline states.

Chapter 6

Cooperative Dynamics of Photoresponsive Liquid Crystal Thin Films

Materials that can reliably, reproducibly, and reversibly change their properties in response to external stimuli are of keen interest in the bottom-up fabrication of intelligent matter. The azobenzene moiety, for example, is a classic way of inducing structural change upon irradiation with UV light, and therefore exhibits high potential as a component of responsive materials. Although much work has already been done on the production of azo-functionalised thin films, it remains challenging to induce the simultaneous, uniform isomerisation required to create a coherently responsive film with these molecules. This project therefore aims to employ azobenzene-functionalised liquid crystals (LC) to (1) produce a two-dimensional (2D) self-assembled film that photoisomerises uniformly upon irradiation with UV light, and (2) characterise the photoswitching energetics and kinetics of the film to better understand the impact of cooperative switching dynamics between neighbouring molecules. These experiments will use ultrahigh vacuum scanning tunnelling microscopy (UHV-STM) to track the isomerisation of individual molecules across the surface, and scanning tunnelling spectroscopy (STS) to detect differences in the local electronic density of states (LDOS) of isomers based on the structural alignment of the molecules surrounding them. To date, we have produced thin films of two LCs (para-azoxyanisole (PAA) and N-(4-Methoxybenzylidene)-4-butylaniline (MBBA)) and confirmed their ability to self-assemble on highly oriented pyrolytic graphite (HOPG). Next steps will involve producing thin films of 4-butyl-4'-methoxyazobenzene (BMAB), the photoactive analogue of MBBA that is currently being synthesised by our collaborators in the Rowan Group (University of Chicago), and proceeding with the subsequent irradiation experiments. Future goals of this project also include investigating how the dynamics of the film's structural isomerisation may influence other surface properties such as passivation and

resistance to chemical reactions like oxidation.

6.1 Introduction

The design and construction of intelligent matter has long dominated the goals of materials chemists in their quest to achieve biological mimicry and smarter technological devices.[111] Applications such as artificial skin that can self-regulate temperature and absorbance,[112;113] clothing that can adjust its warmth according to how its wearer feels,[114] and smart windows that can change their near infrared reflectance and opacity based on environmental conditions such as sunlight intensity or outside temperature[115] inspire hope in our ability to create materials that are able to respond to, adapt to, remember, and process external stimuli that they encounter. In order to succeed in such endeavours, the study and development of responsive systems is key. These materials contain molecular (or macromolecular) components that change their properties in response to a change in their environment, and this change in properties typically remains stable until a countertrigger is administered. Furthermore, in order for responsive materials to have real-world applicability, they should be able to reliably switch between their two states without degradation or failure.[116]

Photoactive functional groups such as stilbenes and azobenzenes are among some of the most commonly used responsive materials when large structural changes are desired.[117;118] These classes of molecules exhibit structural isomerisation that can alter the physical properties of a material without changing its chemical identity. Furthermore, they can easily be incorporated into larger molecular scaffolding (polymers, self-assembled monolayers, etc), providing tunability and flexibility for the type of material that they are employed to photoactivate. The isomerisation of azobenzene derivatives is also typically induced by wavelengths that can be produced by commercially-available sources (e.g. UV laser pointers and "black lights").

Although much work has already been done on the production of azo-functionalised thin films,[119–122] it remains challenging to create molecular films that undergo the simultaneous, uniform isomerisation required to make coherently responsive materials. The thermodynamic stability of the *cis* isomer is often significantly less than that of the *trans*, resulting in thermal relaxation and the reversion of photoexcited molecules to their ground state and rendering the

cis film unstable. Furthermore, in the case of azo-derivatives where the excitation wavelengths for the forward and reverse processes are too similar, illumination with one wavelength will likely result in the continuous activation of both transitions.[117]

This project therefore aims to construct photoactive thin films using azo-functionalised liquid crystals (LC), taking advantage of the long-range order and cooperative dynamics that liquid crystal systems inherently possess.[123] In collaboration with the Rowan Group, we are designing an azo-functionalised LC with a long-lived *cis* state that will self-assemble on surfaces and and photoisomerise uniformly upon irradiation with UV light. We also aim to characterise the photoswitching energetics and kinetics of the film to better understand the influence of cooperative switching dynamics between neighbouring molecules. Finally, future goals of this project also include investigating how the dynamics of the film's structural isomerisation may influence other surface properties such as passivation and resistance to chemical reactions like oxidation.

6.2 Experimental Methods

The liquid crystal films are prepared according to the procedures outlined in **Chapter 2.5.2**. The scanning tunnelling microscopy (STM) images included in this thesis were taken in air with a +0.65 V bias voltage on the sample and a tunnelling current set point between 850-950 pA (Bruker Nanoscope MS-10), though imaging is now also underway using our RHK UHV-STM. Finally, we are currently in the process of purchasing our UV light source and creating the setup for our UV irradiation experiments.

6.3 Current Results

Rod-like liquid crystals must generally contain three structural components: a planar aromatic central region, terminal alkyl chains, and polar groups housed within the alkyl chains to induce dipolar alignment.[123] A common way to create a photoactive LC is therefore to use an azobenzene ring system to fulfill the planar aromatic requirement. Our results for this project thus far are investigatory with respect to two different options for liquid thin films. First, we present STM data on para-azoxyanisole (PAA), a commercially-available photoactive liquid

crystal. However, as discussed below, although these data are promising with respect to film preparation and imaging, this system is unlikely to yield the desired uniform photoswitching behaviour. Second, we explore thin films of N-(4-Methoxybenzylidene)-4-butylaniline (MBBA), a commercially-available *non-photoactive* LC with a non-commercially-available *photoactive analogue*, 4-butyl-4'-methoxyazobenzene (BMAB). Collaboration with the Rowan Group is hence underway to synthesise BMAB using the MBBA precursor, while the STM results herein provide preliminary information on its expected film structure.

6.3.1 Para-azoxyanisole (PAA)

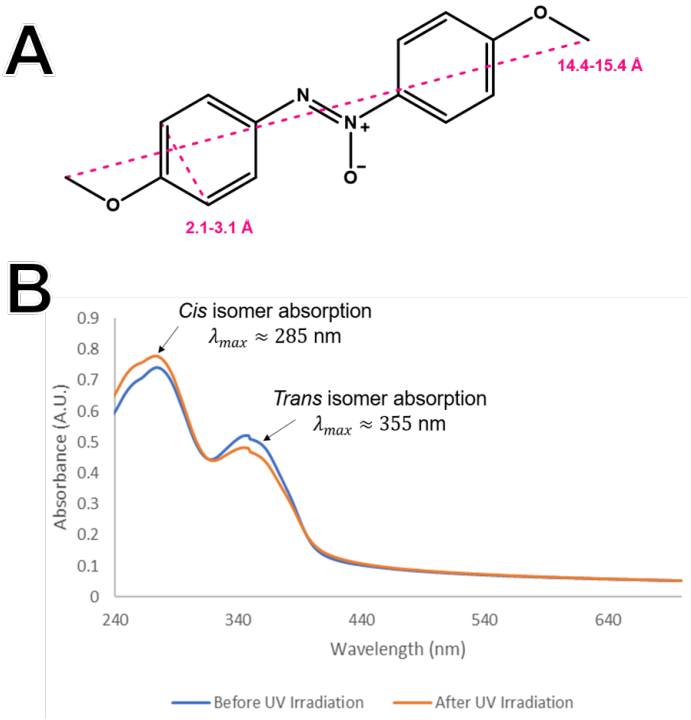

Figure 6.1: (A) Chemical structure of para-azoxyanisole (PAA). Approximate dimensions (calculated in ChemDraw) for the molecule are labelled in pink. (B) UV-Vis spectrum of bulk PAA. After irradiation with UV light, the population of the *trans* isomer decreases and the population of the *cis* isomer increases. This indicates that bulk PAA does indeed isomerise upon exposure to UV light.

PAA (**Figure 6.1**A) is a well-studied compound that was used in the early stages of liquid crystal display (LCD) devlopment[124], and it is known to exhibit *trans*-to-*cis* isomerisation. Furthermore, previous studies[125] confirm that PAA self-assembles into thin films on highly oriented pyrolytic graphite (HOPG), although the photoisomerisation of PAA films has not yet

been documented. Bulk UV-Vis measurements of PAA confirm the peak absorption wavelengths of PAA to be 355 nm for the *trans* isomer and 285 nm for the *cis isomer*, as shown in **Figure 6.1**B.

Figure 6.2A presents an STM image of a PAA thin film on HOPG. The observed structure is similar to that seen in previous work[125], and suggest an alignment of the liquid crystal molecules in rows. A line profile taken perpendicular to the bright stripes (**Figure 6.2**B) indicates an average stripe spacing of ∼1.52 nm, which is approximately the same length as a PAA molecule. Based on this information, as well as the fact that it is typical for ring systems to present as bright regions in STM images of physisorbed self-assembled monolayers due to their high local density of states (LDOS),[126] we propose an alignment in which the two-ring body spans the width of the bright stripes and the ether chains span the width of the dark stripes (**Figure 6.2**C).

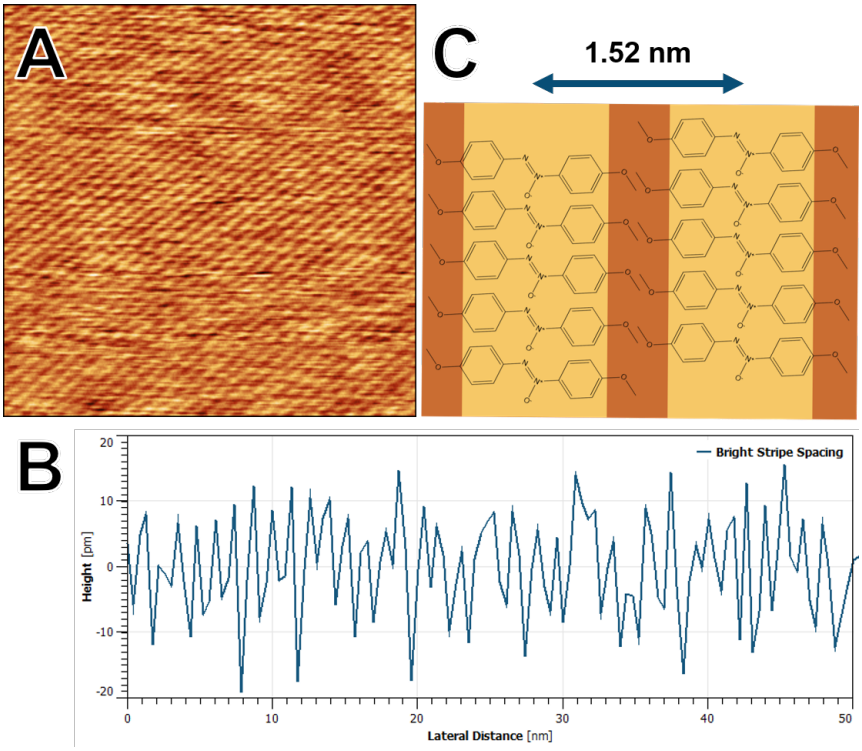

Figure 6.2: (A) STM image (50 nm × 50 nm) of PAA film on HOPG. (B) Line profile taken perpendicular to the bright-and-dark stripe pattern in the STM image of PAA. The spacing between adjacent peaks represents the spacing between adjacent bright stripes. (C) Proposed structural alignment of PAA on the HOPG surface, based on the average peak spacing from line profile (B).

Although the photoisomerisation of PAA is possible, it presents an additional challenge because it is an azoxy compound rather than an azo compound. In addition to isomerisation,

azoxybenzene compounds may undergo a competing UV-activated side reaction that causes a non-reversible rearrangement into their corresponding 2-hydroxyazobenzene.[127] Despite this reaction having minimal impact on the equilibrium crystalline order, it will severely destabilise the *cis* conformation of the molecule, thereby making it an unlikely candidate for long-lived *cis* films.

6.3.2 N-(4-Methoxybenzylidene)-4-butylaniline (MBBA)

The structural similarities between MBBA and BMAB are shown in **Figure 6.3**. We therefore expect BMAB to have nearly identical liquid crystal properties and surface alignment to MBBA, making MBBA an excellent analogue to characterise prior to the synthesis of BMAB.

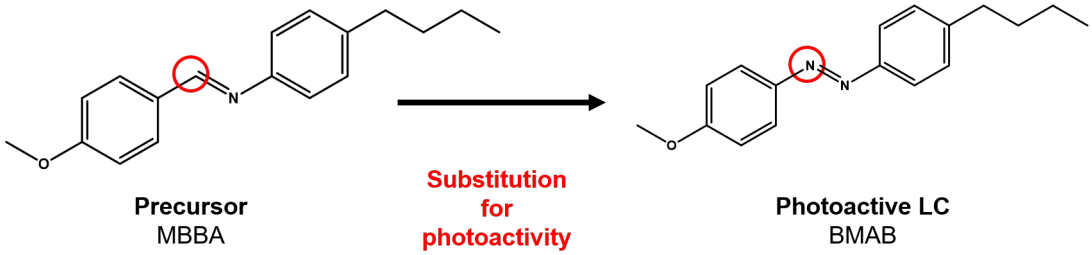

Figure 6.3: The chemical structures of N-(4-Methoxybenzylidene)-4-butylaniline (MBBA) and 4-butyl-4'-methoxyazobenzene (BMAB). Our collaborators in the Rowan Group are working to synthesise BMAB from the commercially-available MBBA.

Figure 6.4A presents an STM image of an MBBA film on HOPG. As with PAA, we observe an alternating bright-and-dark stripe pattern across the surface that suggests a linear alignment of the liquid crystal molecules. A line profile taken perpendicular to the bright stripes (**Figure 6.4**B) indicates an average spacing of 1.73 nm which is once again the approximate length of a single molecule (length MBBA $\approx$ 1.75 nm). An analogous LC alignment to PAA is hence proposed for the MBBA film (**Figure 6.4**C). Efforts are currently being made to obtain molecular-level resolution STM images of both PAA and MBBA films in order to further elucidate their molecular structures.

Unlike PAA, whose *cis* isomer is expected to be unstable and short-lived, the *cis* isomer of BMAB is predicted to be stable for multiple ($\geq$ 12) hours. This longevity can be further extended by adding electron-withdrawing groups such as fluorines to the ring structure of the azobenzene moiety,[128;129] leading to additional synthetic routes being pursued by our collaborators in the

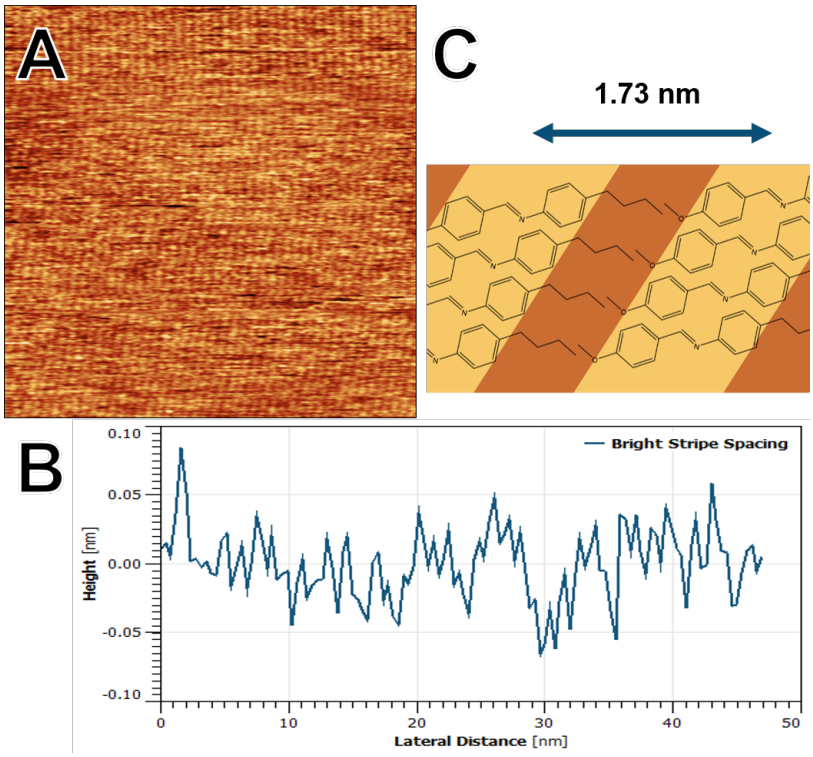

Figure 6.4: (A) STM image (50 nm × 50 nm) of MBBA film on HOPG. (B) Line profile taken perpendicular to the bright-and-dark stripe pattern in the STM image of MBBA. The spacing between adjacent peaks represents the spacing between adjacent bright stripes. (C) Proposed structural alignment of MBBA on the HOPG surface, based on the average peak spacing from line profile (B). This alignment is very similar to that of PAA, which is unsurprising given their similar rod-like LC structures.

Rowan Group.

6.4 Future Directions and Outlook

Next steps on this project begin with the formation and irradiation of BMAB thin films on HOPG. This will first involve the acquisition of a UV-Vis spectrum of the bulk molecule, as well as the purchase and setup of a UV light source of the appropriate wavelength. Challenges with these steps pertain primarily to constructing a UV source configuration for in situ UHV dosing, given the distance of the sample from the instrument viewports. The remainder of this chapter, however, will briefly outline some of the proposed experiments that may follow the successful production of a photoswitchable BMAB film.

6.4.1 Role of Inhomogeneities on the Local Density of States (LDOS)

Previous scanning tunnelling spectroscopy (STS) experiments show that the alignment of discotic liquid crystals with respect to the surface has an effect on their LDOS.[130] This is proposed to be because molecules with a "face-on" orientation (i.e. ring system flat on the substrate) are more strongly coupled to the substrate, thus exhibiting a superior tunnelling efficiency. We therefore propose that STS would measure different spectra for *cis* molecules versus *trans* molecules based on their surface geometry. Additionally, this means that one could expect to see differences in the LDOS of boundary *cis* molecules (*cis* molecules that are adjacent to *trans* molecules) and enclosed *cis* molecules, and vice-versa. Such differences could provide important information about how the lateral interactions between neighbouring molecules influence their electronic structure, which in turn may yield insight about the relative thermodynamic stability of structural inhomogeneities in an LC film.

6.4.2 Kinetics of Thermal *cis*-to-*trans* Isomerisation and the Role of Cooperative Dynamics

As previously mentioned, one of the most important factors determining the applicability of a photoactive liquid crystal film is the rate at which illuminated molecules will revert back from the *cis* state to the *trans* state. One of our goals is hence to measure this rate for our LC films, as has been done for bulk liquid crystal systems,[131] and to determine what role (if any) nearest neighbour interactions play in this process. To achieve this, we plan to track the *cis*-to-*trans* thermal isomerisation of an illuminated film over time using STM imaging – not unlike the SAM reactivity experiments performed in **Chapters 3** and **4**. If no cooperative interactions occur between neighbouring molecules, we expect to observe a first-order rate process characterised by an exponential (Ae^{-kt}). However, if the state of a molecule's neighbour affects the probability of that molecule's isomerisation (e.g. boundary *cis* molecules compared to enclosed *cis* molecules), as has been observed in other photoactive thin films with strong inter-neighbour interactions,[129;132] a more complex kinetic situation should be observed. These results would yield insight on nearest neighbour interactions within LC films, and help tune the chemical functionality of photoactive molecules in order to create uniformly cooperative

switchable films for real-world applications.

6.4.3 Effect of Structural Dynamics on Film Passivation Capabilities

One final proposed project is to study the effect of structural isomerisation on an azo-functionalised film's ability to passivate a surface. This experiment would be similar to those performed in **Chapters 3** and **4**, where we would use STM to monitor the reaction of the LC surface as a function of atomic gas dose. This could be especially interesting for the oxidation reaction of the azobenzene group; firstly, how does the N=N bond fare when exposed to atomic O, and can we detect these chemical changes using STM? Furthermore, does the structure of one isomer better protect the N=N bond, making one form of the film more passivating than the other? Experiments like these could provide information on how the structural dynamics of isomerisation can play a role in the passivation and protection of photoactive materials.

Appendix A

Full Derivation of Kinetic Model for Thiolate SAM Reaction with Atomic Hydrogen (Chapter 3)

This Section contains the full mathematical derivation of **Equation 3.4** in **Chapter 3**, beginning from the differential equation in **Equation 3.3**.

$$\frac{d\theta}{dt} = -k_S\theta_S - k_L(\theta_0 - \theta_S) \tag{A.1}$$

$$\frac{d\theta}{dt} = (k_L - k_S)\theta_S - k_L\theta_0 \tag{A.2}$$

$$= k\theta_S - c \tag{A.3}$$

where $k \equiv k_L - k_S$ and $c \equiv k_L\theta_0$ are both constants.

$$\frac{1}{k\theta_S - c}d\theta_S = dt \tag{A.4}$$

This integral can be solved using u-substitution, where $u = k\theta_S - c$.

$$u = k\theta_S - c \tag{A.5}$$

$$du = kd\theta_S \tag{A.6}$$

$$\frac{du}{k} = d\theta_S \tag{A.7}$$

Therefore,

$$\frac{1}{ku}du = dt \tag{A.8}$$

$$\frac{1}{k}\int \frac{1}{u}du = \int dt \tag{A.9}$$

$$\frac{1}{k}\ln\left(\frac{u}{u_0}\right) = t \tag{A.10}$$

$$\ln\left(\frac{k\theta_S - c}{k\theta_0 - c}\right) = kt \tag{A.11}$$

$$\frac{k\theta_S - c}{k\theta_0 - c} = e^{kt} \tag{A.12}$$

Substituting back in the definitions of k and c, we find:

$$(k_L - k_S)\theta_S - k_L\theta_0 = e^{(k_L - k_S)t}[(k_L - k_S)\theta_0 - k_L\theta_0] \tag{A.13}$$

$$(k_L - k_S)\theta_S = k_L\theta_0 - k_S\theta_0 e^{(k_L - k_S)t} \tag{A.14}$$

$$\frac{\theta_S}{\theta_0} = \frac{k_L}{k_L - k_S} - \frac{k_S}{k_L - k_S}e^{(k_L - k_S)t} \tag{A.15}$$

$$= \frac{1}{1 - \frac{k_S}{k_L}} - \frac{k_S}{k_L}\left(\frac{1}{1 - \frac{k_S}{k_L}}\right)e^{(k_L - k_S)t} \tag{A.16}$$

$$\tag{A.17}$$

And therefore,

$$\frac{\theta_S}{\theta_0} = Ae^{-(k_S - k_L)t} + \frac{1}{1 - \frac{k_S}{k_L}} \tag{A.18}$$

where

$$A \equiv -\frac{k_S}{k_L}\left(\frac{1}{1 - \frac{k_S}{k_L}}\right)$$

Appendix B

Raw Data (Chapter 3)

This Section contains the raw data STM images used to construct **Figures 3.4**, **3.5** and **3.6** in **Chapter 3**. All of these image files are in an electronic repository with the Sibener Group.

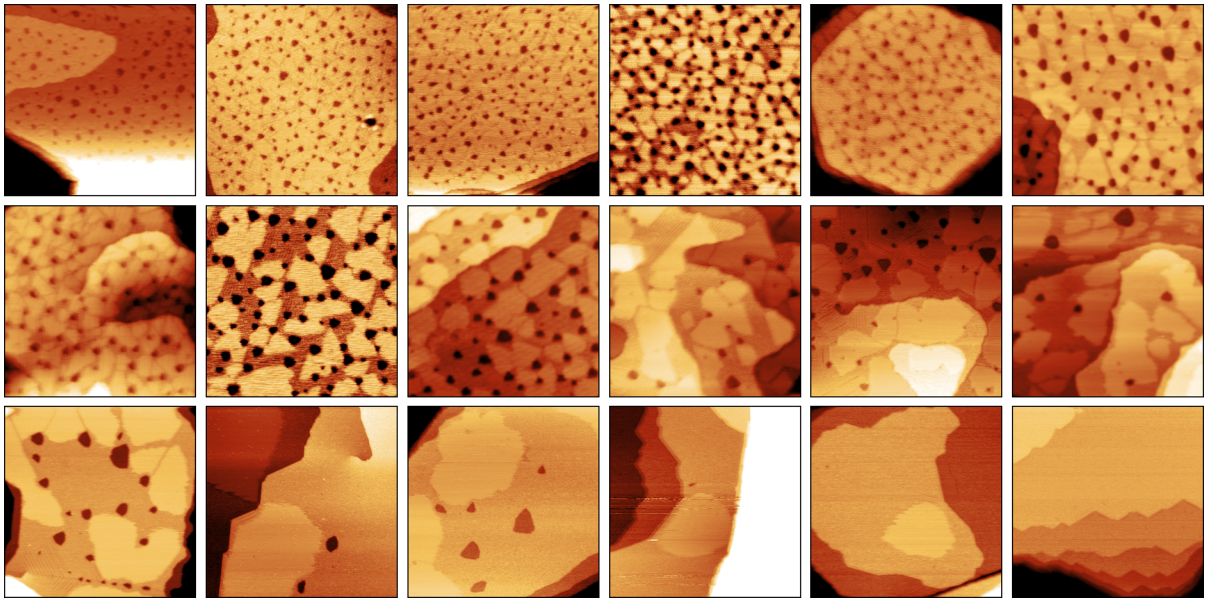

Figure B.1: STM images used to construct 8C SAM kinetics curve (**Figure 3.4**). All images are 200 nm $\times$ 200 nm in size. File names: 2018_04_17_SplitCrystal_8C_0min0004, 2018_04_17_SplitCrystal_8C_0min0010, 2018_04_17_SplitCrystal_8C_0min0012, 2018_04_17_SplitCrystal_8C_5min0033, 2018_04_17_SplitCrystal_8C_5min0036, 2018_04_18_SplitCrystal_8C_5min0003, 2018_04_18_SplitCrystal_8C_5min0017, 2018_04_18_SplitCrystal_8C_8min0035, 2018_04_18_SplitCrystal_8C_8min0038, 2018_04_19_SplitCrystal_8C_8min0007, 2018_04_19_SplitCrystal_8C_10min0018, 2018_04_20_SplitCrystal_8C_10min0025, 2018_04_20_SplitCrystal_8C_10min0029, 2018_04_23_SplitCrystal_8C_11min0002, 2018_04_23_SplitCrystal_8C_11min0008, 2018_04_23_SplitCrystal_8C_11min0011, 2018_04_23_SplitCrystal_8C_12min0037, 2018_04_24_SplitCrystal_8C_13min0017

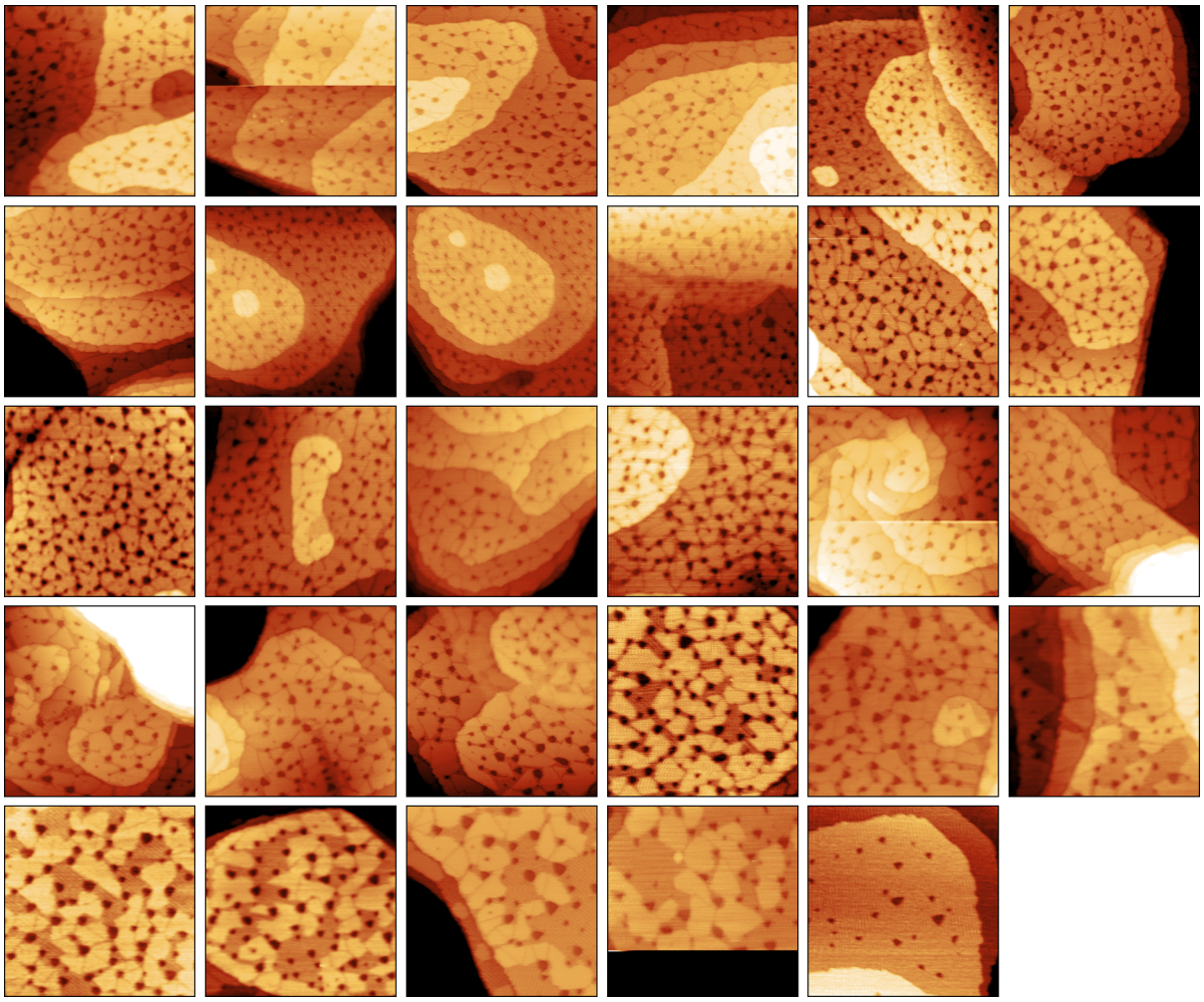

Figure B.2: STM images used to construct 9C SAM kinetics curve (**Figure 3.4**). All images are 200 nm × 200 nm in size. File names: 2018_03_28_split_sample2_9C_unreactred0005, 2018_03_28_split_sample2_9C_10min0031, 2018_03_29_split_sample2_9C_10min0001, 2018_03_29_split_sample2_9C_10min0003, 2018_03_29_split_sample2_9C_20min0037, 2018_03_29_split_sample2_9C_20min0040, 2018_03_29_split_sample2_9C_20min0042, 2018_03_29_split_sample2_9C_20min0051, 2018_03_29_split_sample2_9C_20min0052, 2018_03_30_split_sample2_9C_25min0014, 2018_03_30_split_sample2_9C_25min0017, 2018_03_30_split_sample2_9C_25min0018, 2018_03_30_split_sample2_9C_25min0024, 2018_04_01_split_sample2_9C_25min0005, 2018_04_01_split_sample2_9C_25min0006, 2018_04_01_split_sample2_9C_30min0026, 2018_04_01_split_sample2_9C_30min0028, 2018_04_01_split_sample2_9C_30min0029, 2018_04_01_split_sample2_9C_30min0030, 2018_04_01_split_sample2_9C_30min0031, 2018_04_02_split_sample2_9C_30min0001, 2018_04_02_split_sample2_9C_35min0033, 2018_04_02_split_sample2_9C_35min0034, 2018_04_03_split_sample2_9C_40min0021, 2018_04_03_split_sample2_9C_40min0023, 2018_04_03_split_sample2_9C_40min0028, 2018_04_03_split_sample2_9C_45min0048, 2018_04_04_split_sample2_9C_45min0007, 2018_04_04_split_sample2_9C_50min0010

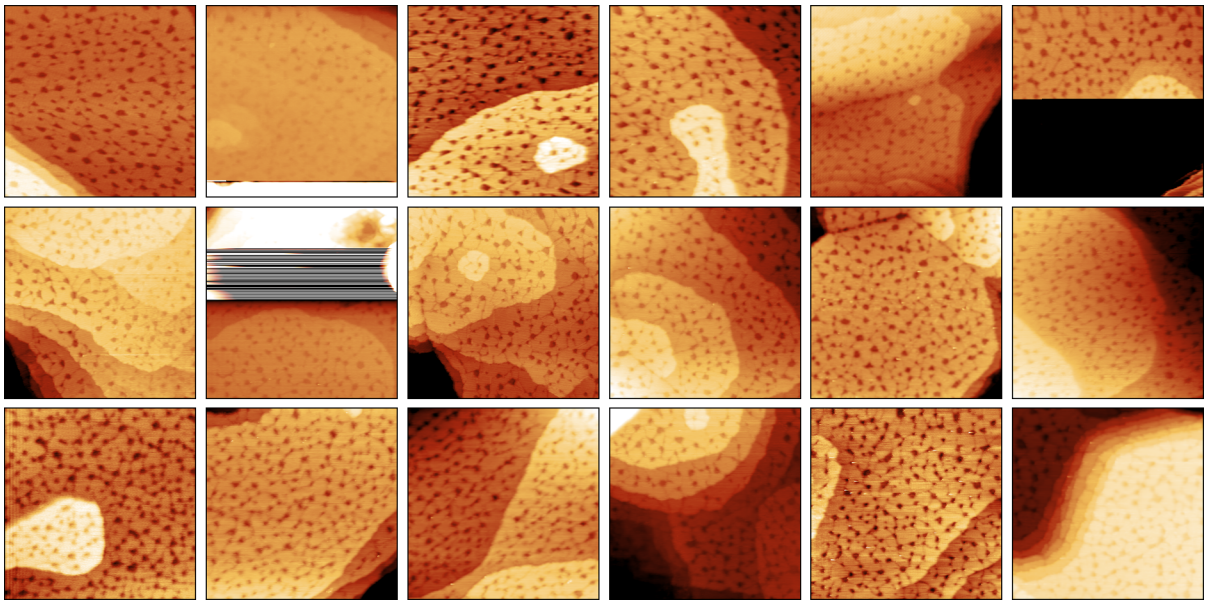

Figure B.3: STM images used to construct 10C SAM kinetics curve (**Figure 3.4**). All images are 200 nm $\times$ 200 nm in size (CONTINUED ON NEXT PAGE) File names:
2018_03_28_split_sample2_10C_10min0007, 2018_03_28_split_sample2_10C_10min0009, 2018_03_28_split_sample2_10C_10min0012, 2018_03_28_split_sample2_10C_10min0020, 2018_03_29_split_sample2_10C_20min0009, 2018_03_29_split_sample2_10C_20min0014, 2018_03_29_split_sample2_10C_20min0017, 2018_03_29_split_sample2_10C_20min0022, 2018_03_29_split_sample2_10C_20min0027, 2018_03_30_split_sample2_10C_25min0011, 2018_03_30_split_sample2_10C_25min0012, 2018_04_01_split_sample2_10C_25min0001, 2018_04_01_split_sample2_10C_30min0010, 2018_04_01_split_sample2_10C_30min0013, 2018_04_01_split_sample2_10C_30min0014, 2018_04_01_split_sample2_10C_30min0017, 2018_04_02_split_sample2_10C_35min0009, 2018_04_03_split_sample2_10C_35min0002, 2018_04_03_split_sample2_10C_35min0005, 2018_04_03_split_sample2_10C_40min0009, 2018_04_03_split_sample2_10C_40min0018, 2018_04_03_split_sample2_10C_45min0041, 2018_04_03_split_sample2_10C_45min0043, 2018_04_04_split_sample2_10C_50min0017, 2018_04_04_split_sample2_10C_50min0018, 2018_04_04_split_sample2_10C_50min0020, 2018_04_04_split_sample2_10C_50min0021, 2018_04_05_split_sample2_10C_50min0003, 2018_04_05_split_sample2_10C_50min0009, 2018_04_05_split_sample2_10C_50min0010, 2018_04_05_split_sample2_10C_55min0012, 2018_04_05_split_sample2_10C_55min0015, 2018_04_05_split_sample2_10C_55min0016, 2018_04_05_split_sample2_10C_55min0018, 2018_04_05_split_sample2_10C_60min0032, 2018_04_05_split_sample2_10C_60min0038, 2018_04_09_split_sample2_10C_60min0003, 2018_04_10_split_sample2_10C_65min0001, 2018_04_11_split_sample2_10C_70min0001_final

FIGURE B.3 CONTINUED

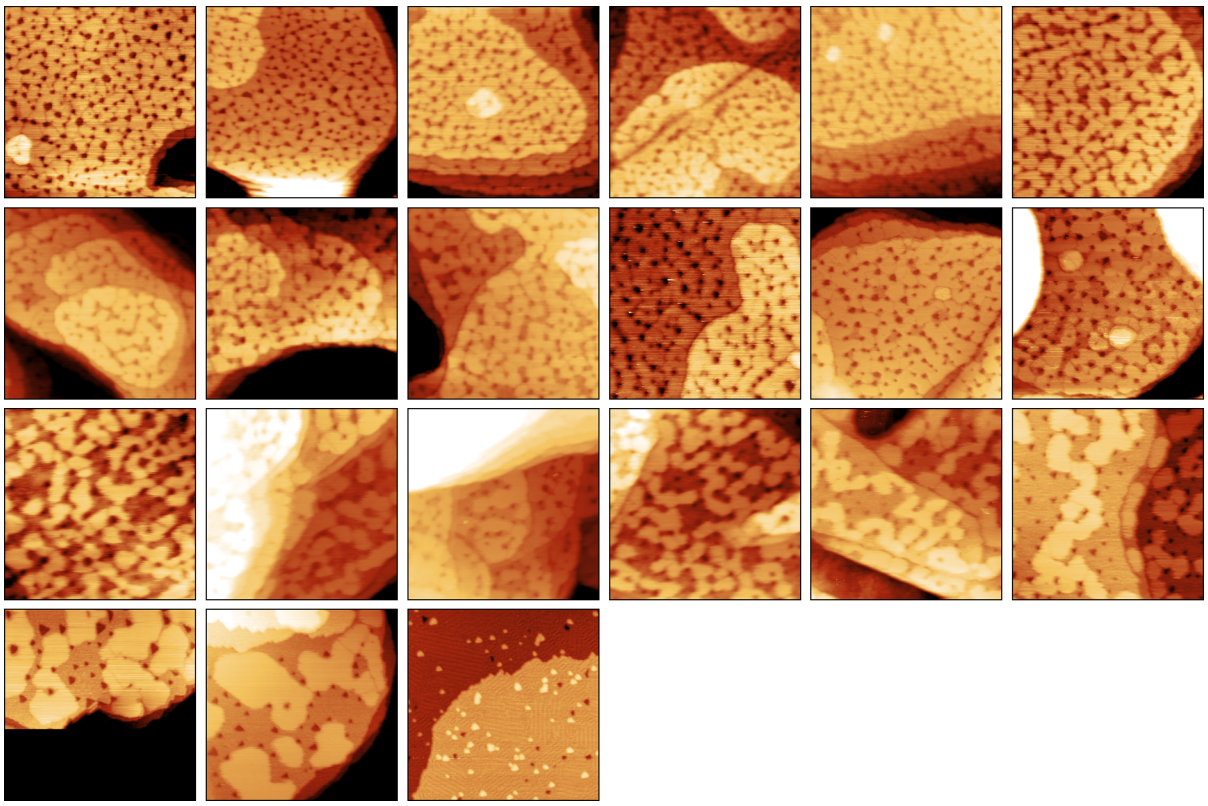

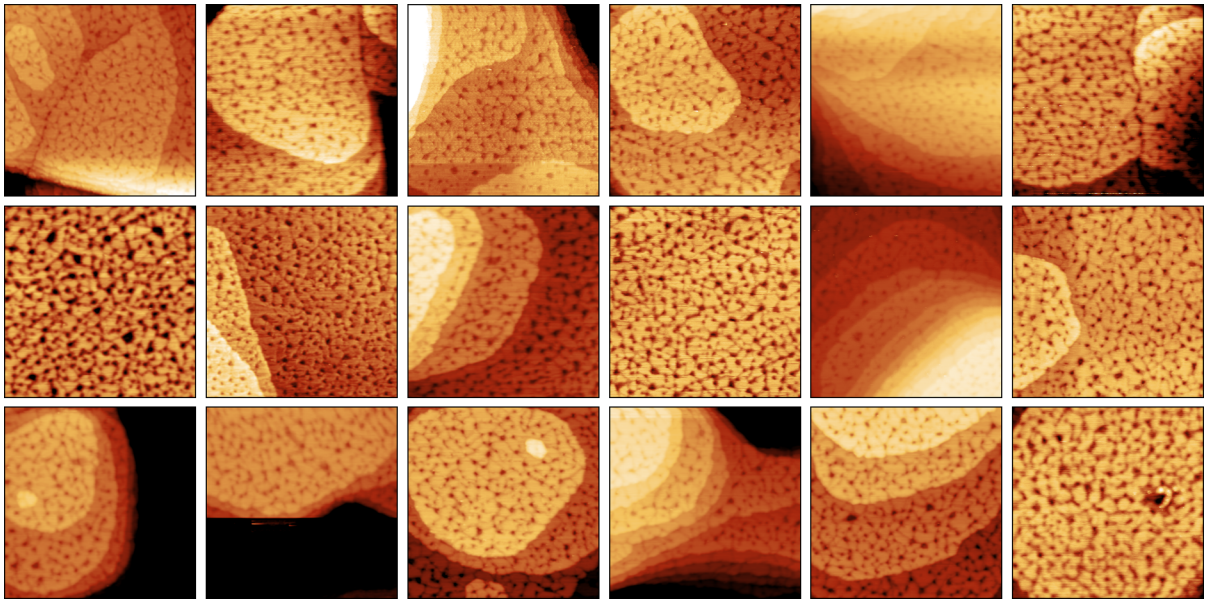

Figure B.4: STM images used to construct 11C SAM kinetics curve (**Figure 3.4**). All images are 200 nm × 200 nm in size (CONTINUED ON NEXT PAGE) File names:
2018_05_11_5SplitCrystal_11C_0min0004, 2018_05_14_5SplitCrystal_11C_0min0013, 2018_05_15_5SplitCrystal_11C_15min0022_crop, 2018_05_15_5SplitCrystal_11C_15min0040, 2018_05_15_5SplitCrystal_11C_15min0045, 2018_05_16_5SplitCrystal_11C_15min0002, 2018_05_16_5SplitCrystal_11C_20min0038, 2018_05_16_5SplitCrystal_11C_20min0042, 2018_05_17_5SplitCrystal_11C_20min0001, 2018_05_17_5SplitCrystal_11C_20min0007, 2018_05_17_5SplitCrysta_11C_25min0036, 2018_05_17_5SplitCrystal_11C_25min0040, 2018_05_17_5SplitCrystal_11C_25min0042, 2018_05_17_5SplitCrystal_11C_25min0043, 2018_05_18_5SplitCrystal_11C_25min0002, 2018_05_18_5SplitCrystal_11C_25min0003, 2018_05_18_5SplitCrystal_11C_25min0005, 2018_05_18_5SplitCrystal_11C_30min0022, 2018_05_18_5SplitCrystal_11C_30min0025, 2018_05_18_5SplitCrystal_11C_30min0027, 2018_05_18_5SplitCrystal_11C_30min0029, 2018_05_18_5SplitCrystal_11C_30min0032, 2018_05_21_5SplitCrystal_11C_35min0016, 2018_05_21_5SplitCrystal_11C_35min0017, 2018_05_21_5SplitCrystal_11C_35min0021, 2018_05_21_5SplitCrystal_11C_35min0023, 2018_05_21_5SplitCrystal_11C_35min0024, 2018_05_22_5SplitCrystal_11C_35min0002, 2018_05_22_5SplitCrystal_11C_35min0004, 2018_05_23_5SplitCrystal_11C_40min0002, 2018_05_23_5SplitCrystal_11C_40min0004, 2018_05_23_5SplitCrystal_11C_40min0005, 2018_05_24_5SplitCrystal_11C_45min0008, 2018_05_24_5SplitCrystal_11C_45min0009, 2018_05_24_5SplitCrystal_11C_45min0011, 2018_05_24_5SplitCrystal_11C_45min0014, 2018_05_24_5SplitCrystal_11C_45min0015, 2018_05_24_5SplitCrystal_11C_45min0016, 2018_05_24_5SplitCrystal_11C_45min0018, 2018_05_24_5SplitCrystal_11C_45min0019, 2018_05_25_5SplitCrystal_11C_50min0003, 2018_05_25_5SplitCrystal_11C_50min0005, 2018_05_25_5SplitCrystal_11C_50min0006, 2018_05_25_5SplitCrystal_11C_50min0008, 2018_05_25_5SplitCrystal_11C_50min0011, 2018_05_25_5SplitCrystal_11C_50min0012, 2018_05_25_5SplitCrystal_11C_50min0013, 2018_05_25_5SplitCrystal_11C_50min0014, 2018_05_28_5SplitCrystal_11C_55min0003, 2018_05_28_5SplitCrystal_11C_55min0004, 2018_05_28_5SplitCrystal_11C_55min0008, 2018_05_28_5SplitCrystal_11C_55min0010, 2018_05_28_5SplitCrystal_11C_55min0011, 2018_05_28_5SplitCrystal_11C_55min0012, 2018_05_28_5SplitCrystal_11C_55min0014, 2018_05_28_5SplitCrystal_11C_55min0015, 2018_05_28_5SplitCrystal_11C_55min0016

FIGURE B.4 CONTINUED

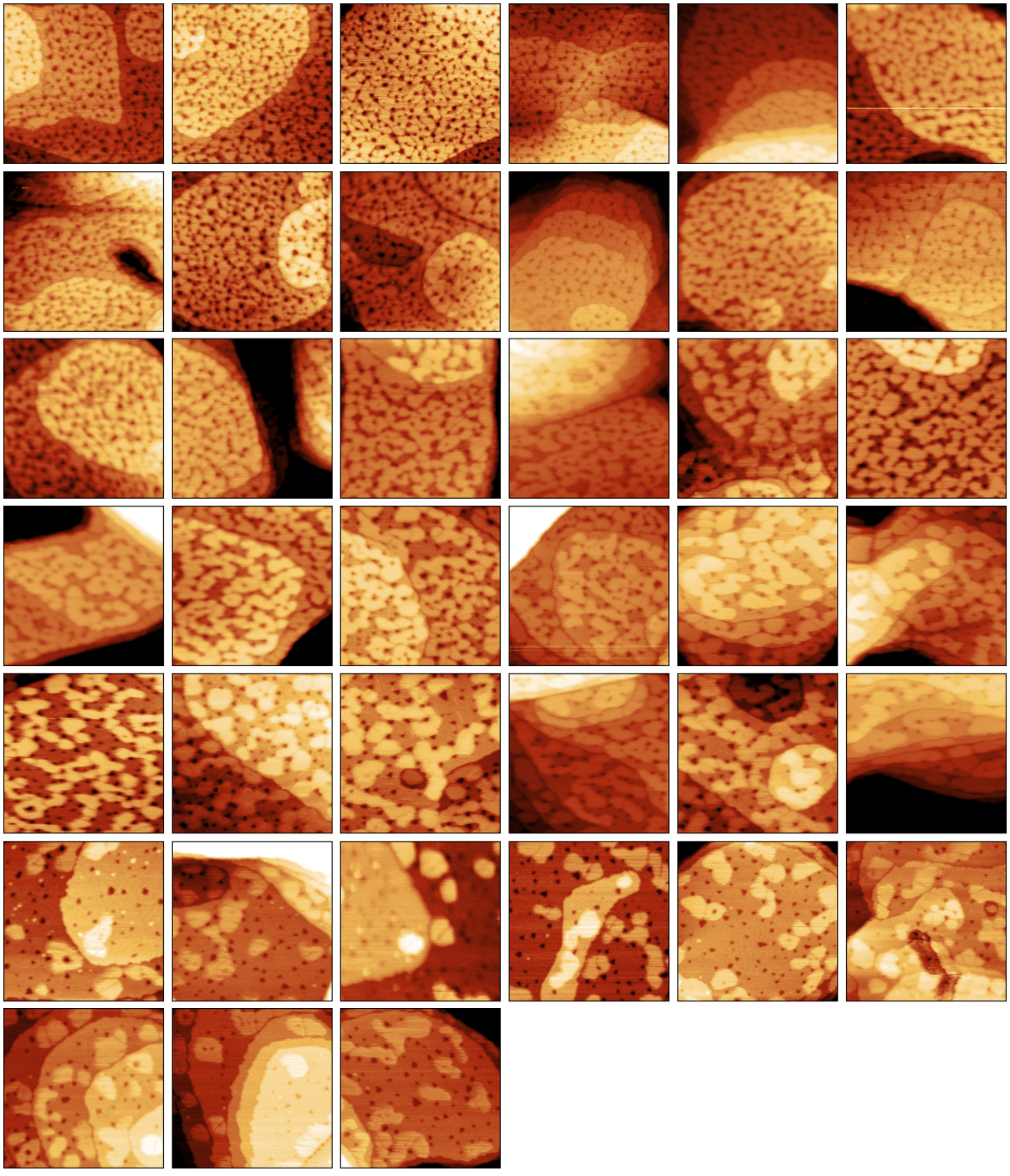

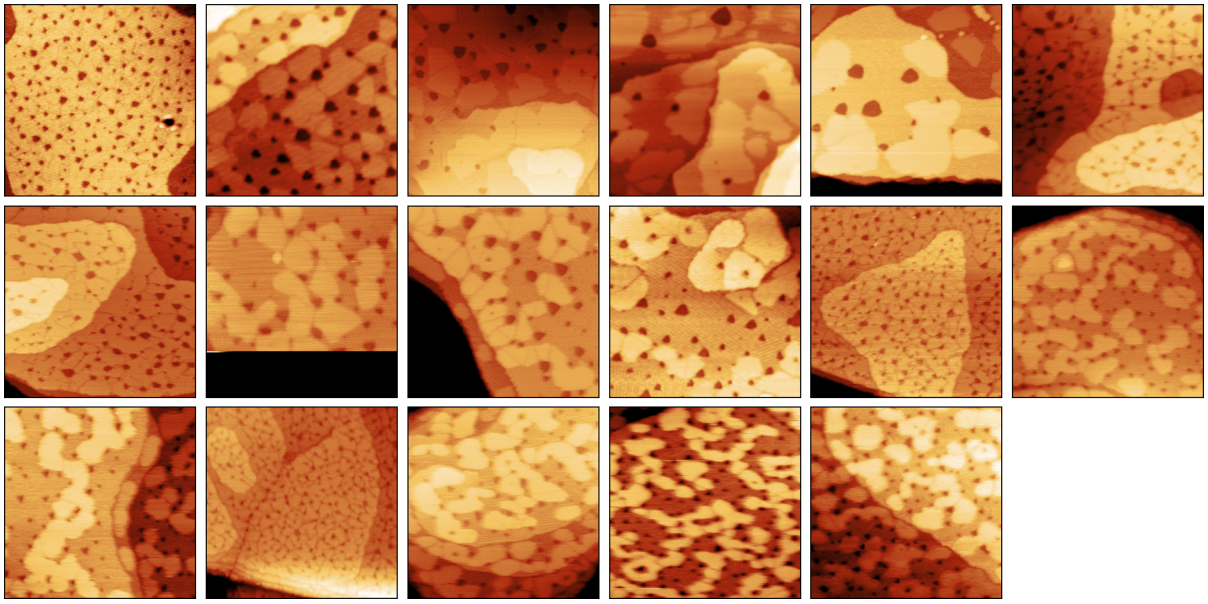

Figure B.5: STM images used to analyse etch pit size as a function of thiolate chain length during the SAM's reaction with atomic H (**Figures 3.5** & **3.6**). All images are 200 nm $\times$ 200 nm in size. File names: 2018_04_17_SplitCrystal_8C_0min0010, 2018_04_18_SplitCrystal_8C_8min0038, 2018_04_19_SplitCrystal_8C_10min0018_etchpits, 2018_04_20_SplitCrystal_8C_10min0025, 2018_04_20_SplitCrystal_8C_10min0026, 2018_03_28_split_sample2_9C_unreactred0005, 2018_03_29_split_sample2_9C_10min0001, 2018_04_04_split_sample2_9C_45min0007, 2018_04_03_split_sample2_9C_45min0048, 2018_04_03_split_sample2_9C_45min0050, 2018_04_17_SplitCrystal_10C_0min0022, 2018_04_05_split_sample2_10C_60min0036, 2018_04_05_split_sample2_10C_60min0038, 2018_05_11_5SplitCrystal_11C_0min0004, 2018_05_25_5SplitCrystal_11C_50min0003, 2018_05_25_5SplitCrystal_11C_50min0006, 2018_05_25_5SplitCrystal_11C_50min0008

Appendix C

Raw Data (Chapter 4)

This Section contains the raw data STM images used to construct **Figures 4.2**, **4.3** and **4.4** in **Chapter 4**. All of these image files are in an electronic repository with the Sibener Group.

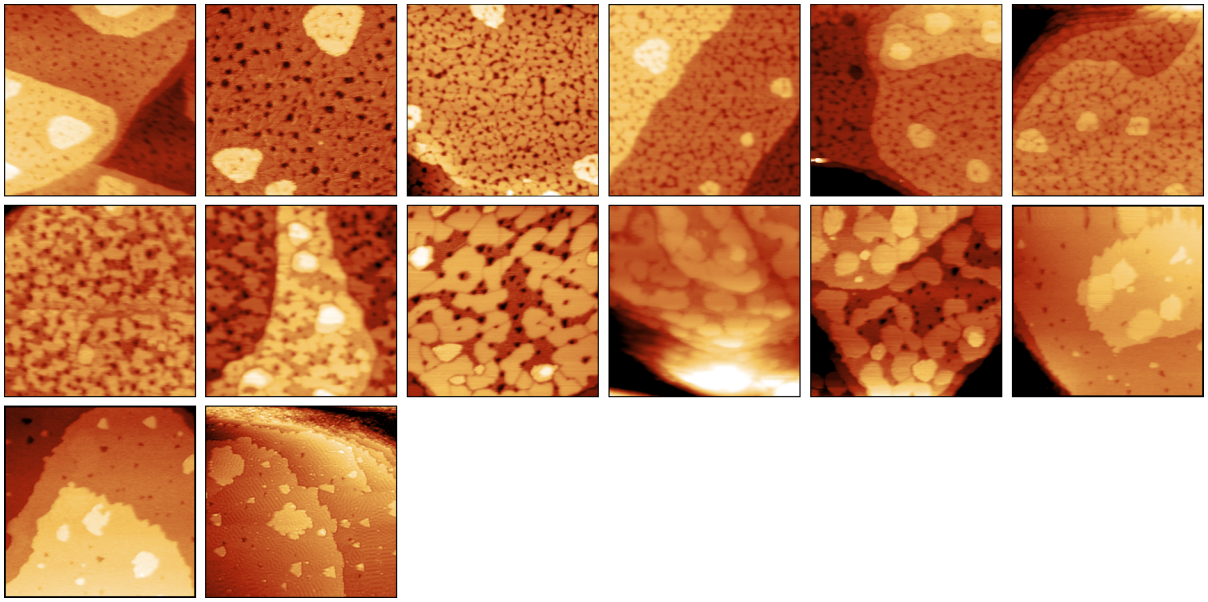

Figure C.1: STM images used to construct 10C SAM kinetics curve at 295 K (**Figures 4.2 and 4.3**). All images are 200 nm $\times$ 200 nm in size. File names: 2018_11_20_10CSAM0001, 2018_11_20_10CSAM0017, 2018_11_21_10CSAM_20min_reaction0005, 2018_11_21_10CSAM_20min_reaction0011, 2018_11_21_10CSAM_30min_reaction0016, 2018_11_21_10CSAM_30min_reaction0023, 2018_11_21_10CSAM_40min_reaction0032, 2018_11_21_10CSAM_40min_reaction0038, 2018_11_25_10CSAM_40min_reaction0000, 2018_11_25_10CSAM_45min_reaction0002, 2018_11_25_10CSAM_45min_reaction0004, 2018_11_25_10CSAM_50min_reaction0005, 2018_11_25_10CSAM_50min_reaction0007, 2018_11_25_10CSAM_55min_reaction0015

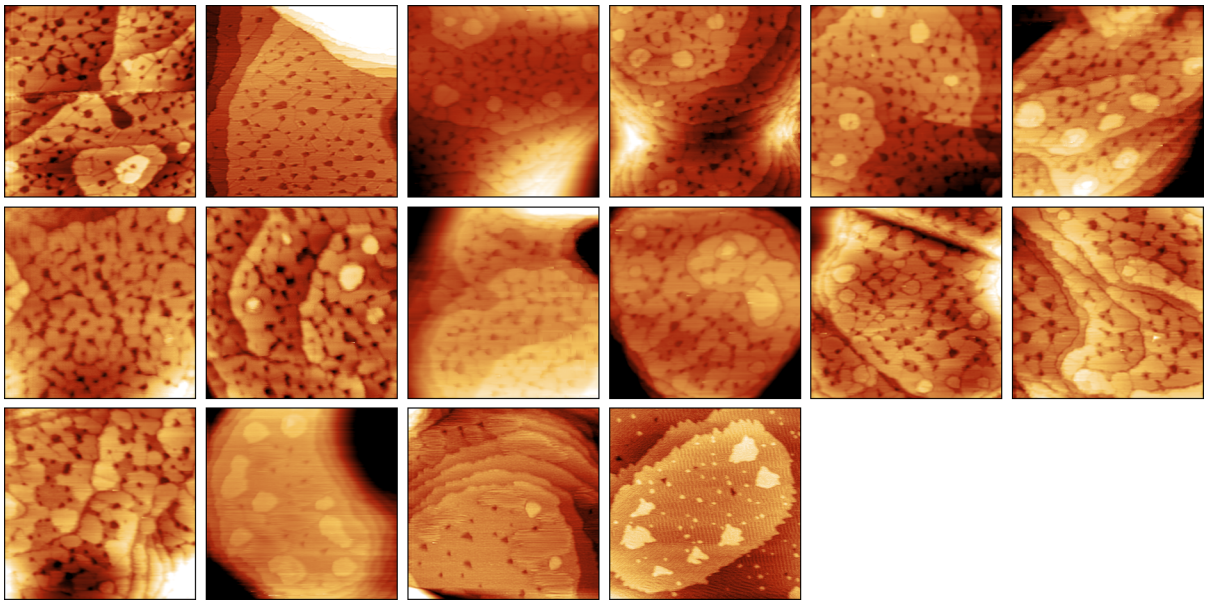

Figure C.2: STM images used to construct 10C SAM kinetics curve at 270 K (**Figure 4.2**). All images are 200 nm $\times$ 200 nm in size. File names: 2018_12_20_SAM_0min_RT0006, 2018_12_20_SAM_0min_RT0017, 2018_12_20_SAM_60min_270k0028, 2018_12_20_SAM_60min_270k0029, 2018_12_20_SAM_60min_270k0035, 2018_12_20_SAM_75min_270k0040, 2018_12_20_SAM_75min_270k0043, 2018_12_20_SAM_75min_270k0045, 2018_12_20_SAM_75min_270k0049, 2018_12_20_SAM_90min_270k0051, 2018_12_20_SAM_90min_270k0052, 2018_12_20_SAM_90min_270k0054, 2018_12_20_SAM_90min_270k0056, 2018_12_21_SAM_105min_270k0004, 2018_12_21_SAM_105min_270k0008, 2018_12_21_SAM_120min_270k0014

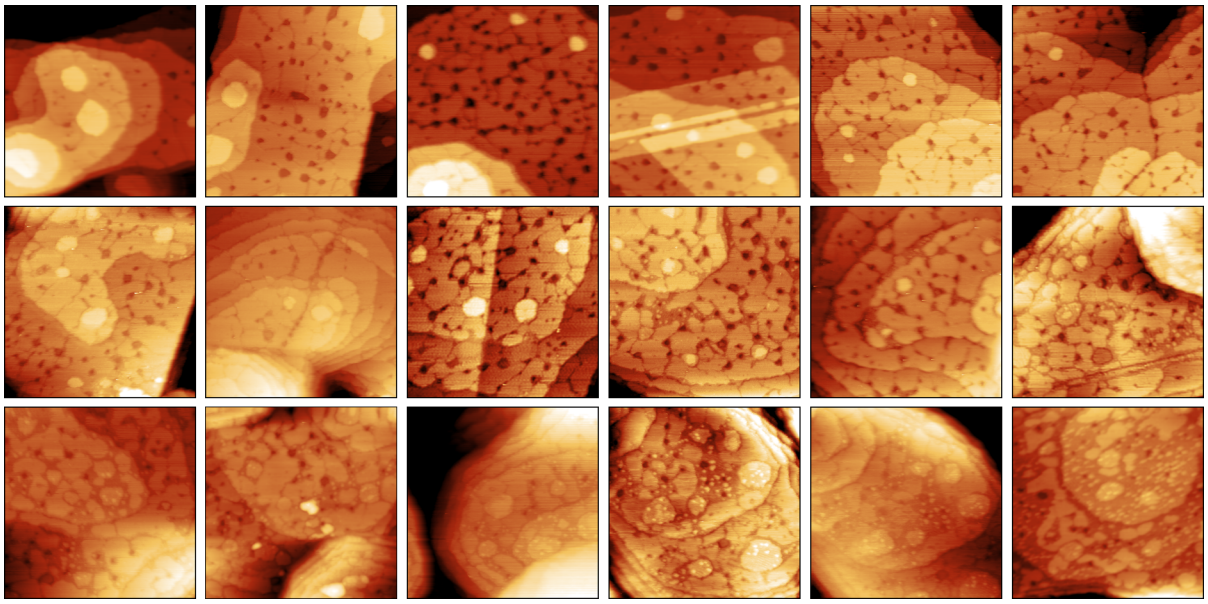

Figure C.3: STM images used to construct 10C SAM kinetics curve at 250 K (**Figures 4.2 and 4.3**). All images are 200 nm × 200 nm in size (CONTINUED ON NEXT PAGE) File names:
2018_12_07_SAM_unreacted0001, 2018_12_07_SAM_unreacted0005,
2018_12_10_SAM_60min_250K_ImagedRT0001, 2018_12_10_SAM_60min_250K_ImagedRT0004,
2018_12_10_SAM_90min_250K_Imaged250K0025,
2018_12_10_SAM_90min_250K_Imaged250K0028,
2018_12_10_SAM_105min_250K_Imaged250K0034,
2018_12_10_SAM_105min_250K_Imaged250K0040,
2018_12_11_SAM_105min_250K_Imaged250K0001,
2018_12_11_SAM_120min_250K_Imaged250K0009,
2018_12_11_SAM_120min_250K_Imaged250K0018,
2018_12_11_SAM_135min_250K_Imaged250K0024,
2018_12_11_SAM_135min_250K_Imaged250K0028,
2018_12_11_SAM_135min_250K_Imaged250K0032,
2018_12_11_SAM_150min_250K_Imaged250K0039,
2018_12_11_SAM_150min_250K_Imaged250K0040,
2018_12_11_SAM_150min_250K_Imaged250K0043,
2018_12_12_SAM_165min_250K_Imaged250K0001,
2018_12_12_SAM_165min_250K_Imaged250K0005,
2018_12_12_SAM_165min_250K_Imaged250K0011,
2018_12_12_SAM_180min_250K_Imaged250K0013,
2018_12_12_SAM_180min_250K_Imaged250K0015,
2018_12_12_SAM_180min_250K_Imaged250K0021,
2018_12_12_SAM_195min_250K_Imaged250K0026,
2018_12_12_SAM_195min_250K_Imaged250K0031

FIGURE C.3 CONTINUED

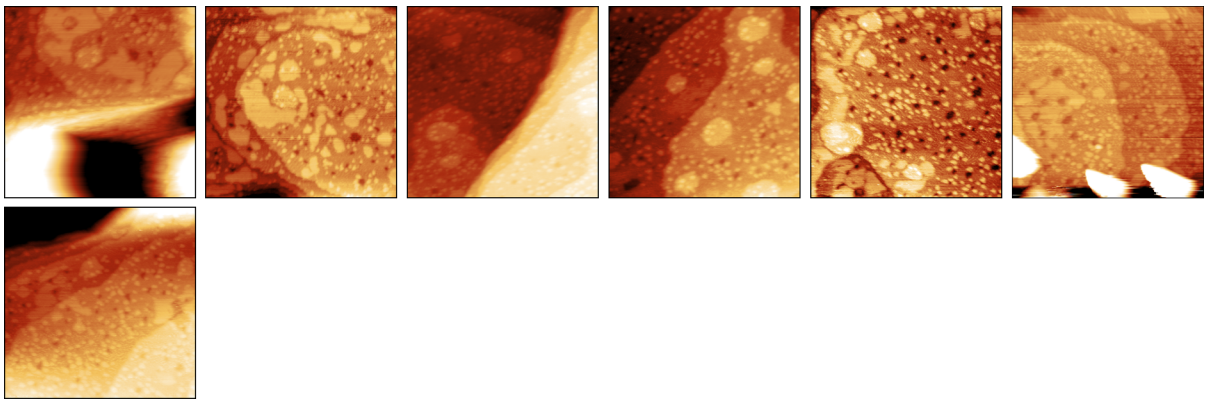

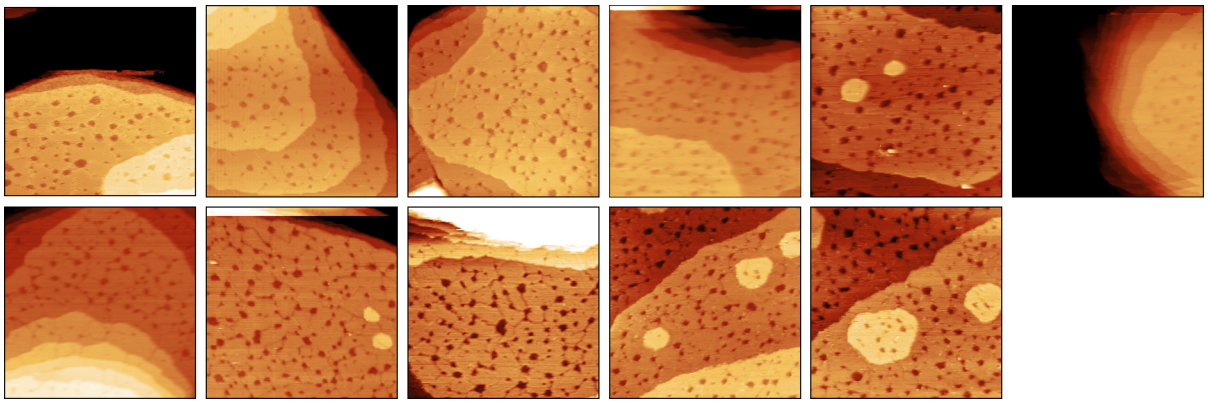

Figure C.4: STM images used to construct 10C SAM kinetics curve at 130 K (**Figure 4.2**). All images are 200 nm × 200 nm in size. File names: 2018_11_27_10CSAM_0min_cold_reaction0001, 2018_11_27_10CSAM_0min_cold_reaction0012, 2018_11_29_10CSAM_0min_cold_reaction0002, 2018_11_29_10CSAM_40min_cold_reaction0015, 2018_11_29_10CSAM_40min_cold_reaction0023, 2018_11_29_10CSAM_40min_cold_reaction0025, 2018_11_30_10CSAM_120min_cold_reaction_imagedRT0001, 2018_11_30_10CSAM_120min_cold_reaction_imagedRT0018, 2018_11_30_10CSAM_120min_cold_reaction_imagedRT0023, 2021_04_16_10C-SAM-130K_loc10007, 2021_04_16_10C-SAM-130K_loc10008

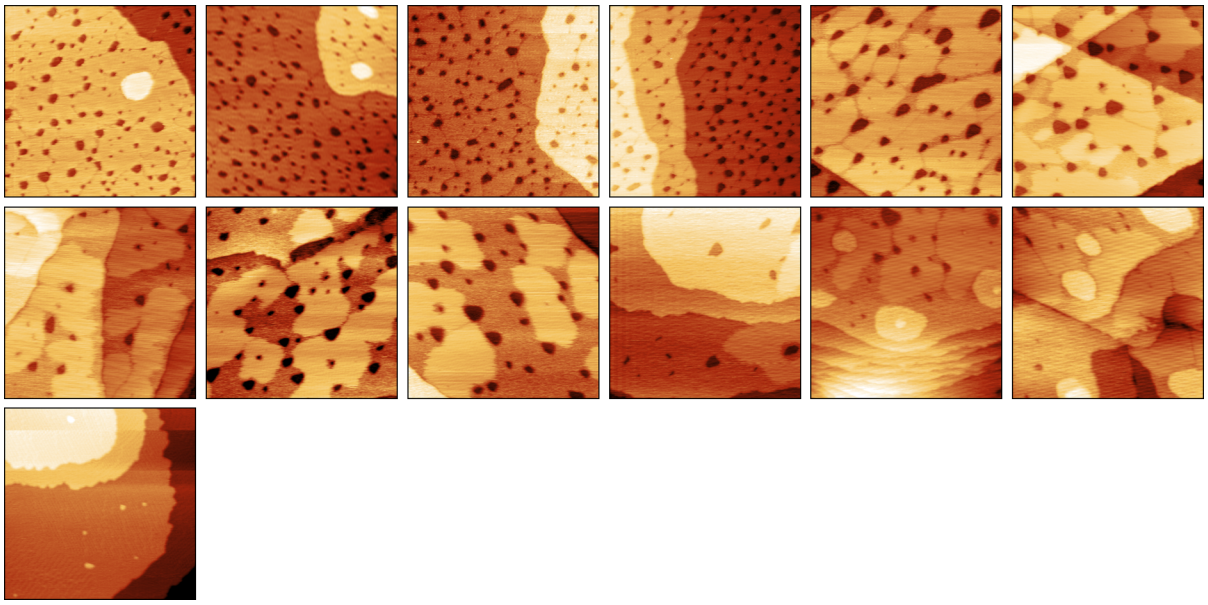

Figure C.5: STM images used to construct 8C SAM kinetics curve at 295 K (**Figure 4.3**). All images are 200 nm × 200 nm in size. File names:
2020_10_23_8C-PHASIS-H-anneal-BUBBLE-295K-0min0008,
2020_10_28_8C-PHASIS-H-anneal-BUBBLE-295K-5min-loc20009,
2020_10_28_8C-PHASIS-H-anneal-BUBBLE-295K-15min-loc20018,
2020_10_28_8C-PHASIS-H-anneal-BUBBLE-295K-25min-loc10023,
2020_10_29_8C-PHASIS-H-anneal-BUBBLE-295K-35min-loc20010,
2020_10_29_8C-PHASIS-H-anneal-BUBBLE-295K-45min-loc10022,
2020_10_29_8C-PHASIS-H-anneal-BUBBLE-295K-55min-loc10023,
2020_10_29_8C-PHASIS-H-anneal-BUBBLE-295K-55min-loc20029,
2020_10_29_8C-PHASIS-H-anneal-BUBBLE-295K-55min-loc20033,
2020_10_29_8C-PHASIS-H-anneal-BUBBLE-295K-65min-loc10034,
2020_10_29_8C-PHASIS-H-anneal-BUBBLE-295K-65min-loc20044,
2020_10_29_8C-PHASIS-H-anneal-BUBBLE-295K-65min-loc20046,
2020_10_30_8C-PHASIS-H-anneal-BUBBLE-295K-75min-loc10006

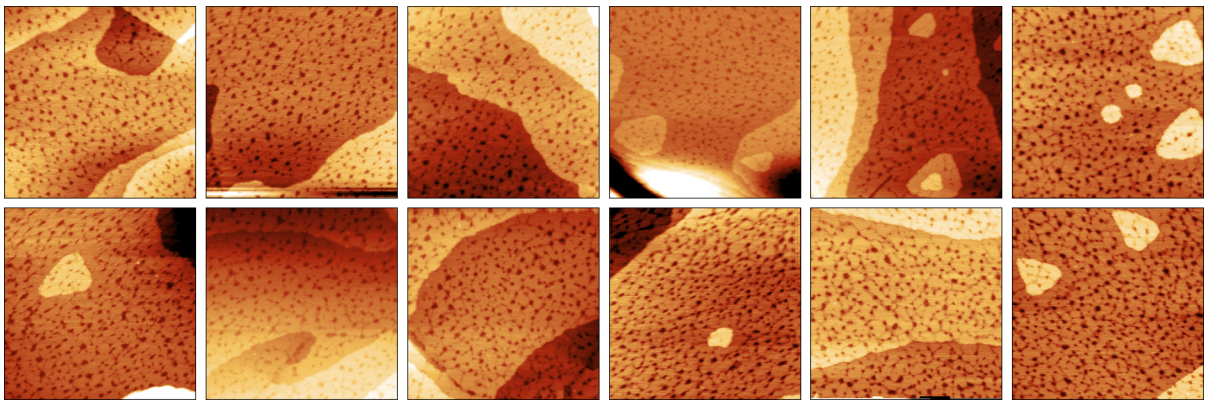

Figure C.6: STM images used to construct 8C SAM kinetics curve at 250 K (**Figure 4.3**). All images are 200 nm × 200 nm in size (CONTINUED ON NEXT PAGE) File names:
2020_12_04_8C-PHA-RT-SOAK-2-DROPS-250K-loc10002,
2020_12_04_8C-PHA-RT-SOAK-2-DROPS-250K-loc10005,
2020_12_04_8C-PHA-RT-SOAK-2-DROPS-250K-loc10007,
2020_12_04_8C-PHA-RT-SOAK-2-DROPS-250K-40min-loc10008,
2020_12_04_8C-PHA-RT-SOAK-2-DROPS-250K-40min-loc10014,
2020_12_04_8C-PHA-RT-SOAK-2-DROPS-250K-40min-loc10016,
2020_12_04_8C-PHA-RT-SOAK-2-DROPS-250K-50min-loc10020,
2020_12_04_8C-PHA-RT-SOAK-2-DROPS-250K-50min-loc10022,
2020_12_04_8C-PHA-RT-SOAK-2-DROPS-250K-50min-loc10027,
2020_12_04_8C-PHA-RT-SOAK-2-DROPS-250K-75min-loc10044,
2020_12_08_8C-PHA-RT-SOAK-2-DROPS-250K-85min-loc10004,
2020_12_08_8C-PHA-RT-SOAK-2-DROPS-250K-100min-loc10012,
2020_12_08_8C-PHA-RT-SOAK-2-DROPS-250K-100min-loc10014,
2020_12_08_8C-PHA-RT-SOAK-2-DROPS-250K-100min-loc10018,
2020_12_08_8C-PHA-RT-SOAK-2-DROPS-250K-115min-loc10022,
2020_12_08_8C-PHA-RT-SOAK-2-DROPS-250K-115min-loc10023,
2020_12_08_8C-PHA-RT-SOAK-2-DROPS-250K-115min-loc10026,
2020_12_09_8C-PHA-RT-SOAK-2-DROPS-250K-130min-loc10003,
2020_12_09_8C-PHA-RT-SOAK-2-DROPS-250K-130min-loc10001,
2020_12_09_8C-PHA-RT-SOAK-2-DROPS-250K-130min-loc10005,
2020_12_09_8C-PHA-RT-SOAK-2-DROPS-250K-150min-loc10019,
2020_12_09_8C-PHA-RT-SOAK-2-DROPS-250K-170min-loc10026,
2020_12_13_8C-PHA-RT-SOAK-2-DROPS-250K-190min-loc10000,
2020_12_13_8C-PHA-RT-SOAK-2-DROPS-250K-190min-loc10001,
2020_12_13_8C-PHA-RT-SOAK-2-DROPS-250K-190min-loc10010,
2020_12_13_8C-PHA-RT-SOAK-2-DROPS-250K-210min-loc10015,
2020_12_13_8C-PHA-RT-SOAK-2-DROPS-250K-210min-loc10016,
2020_12_13_8C-PHA-RT-SOAK-2-DROPS-250K-210min-loc10019,
2020_12_13_8C-PHA-RT-SOAK-2-DROPS-250K-225min-loc10030,
2020_12_13_8C-PHA-RT-SOAK-2-DROPS-250K-265min-loc10046,
2020_12_13_8C-PHA-RT-SOAK-2-DROPS-250K-265min-loc10047,
2020_12_13_8C-PHA-RT-SOAK-2-DROPS-250K-265min-loc10049,
2020_12_13_8C-PHA-RT-SOAK-2-DROPS-250K-285min-loc10062,
2020_12_13_8C-PHA-RT-SOAK-2-DROPS-250K-285min-loc10064,
2020_12_13_8C-PHA-RT-SOAK-2-DROPS-250K-285min-loc10066,
2020_12_13_8C-PHA-RT-SOAK-2-DROPS-250K-295min-loc10068

FIGURE C.6 CONTINUED

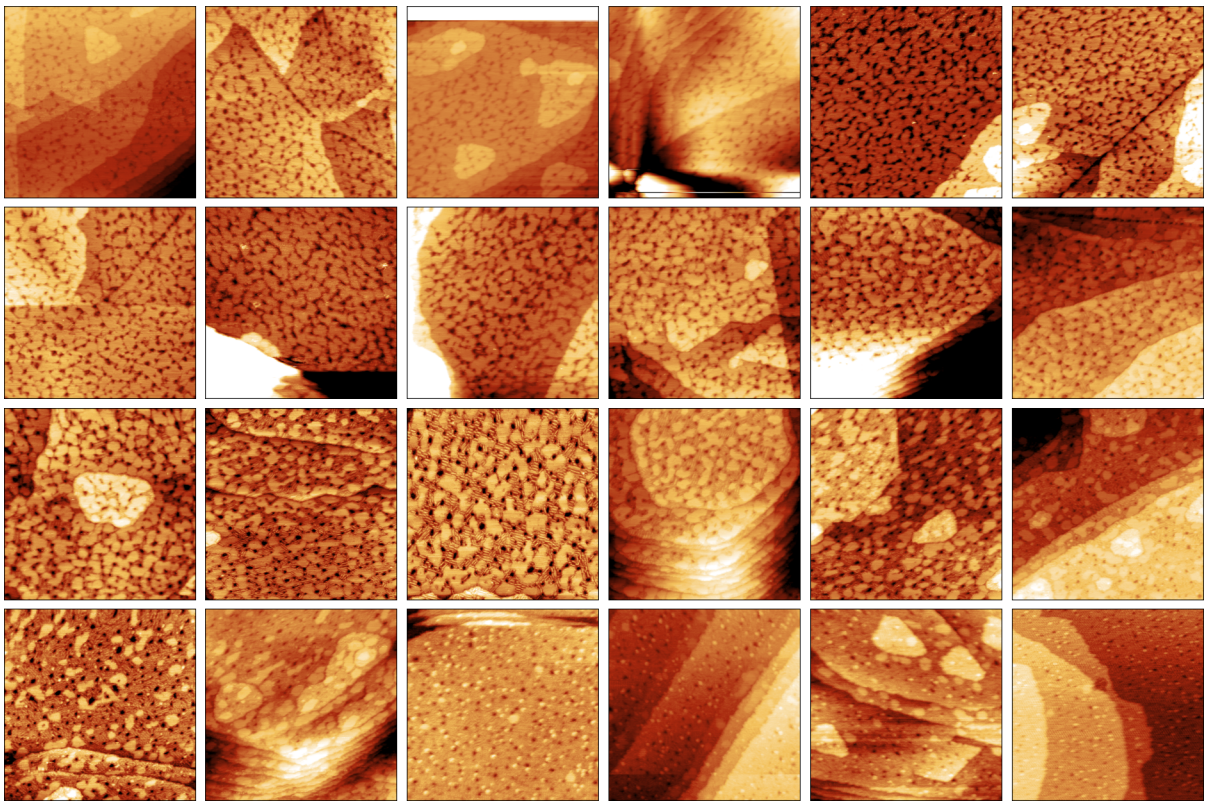

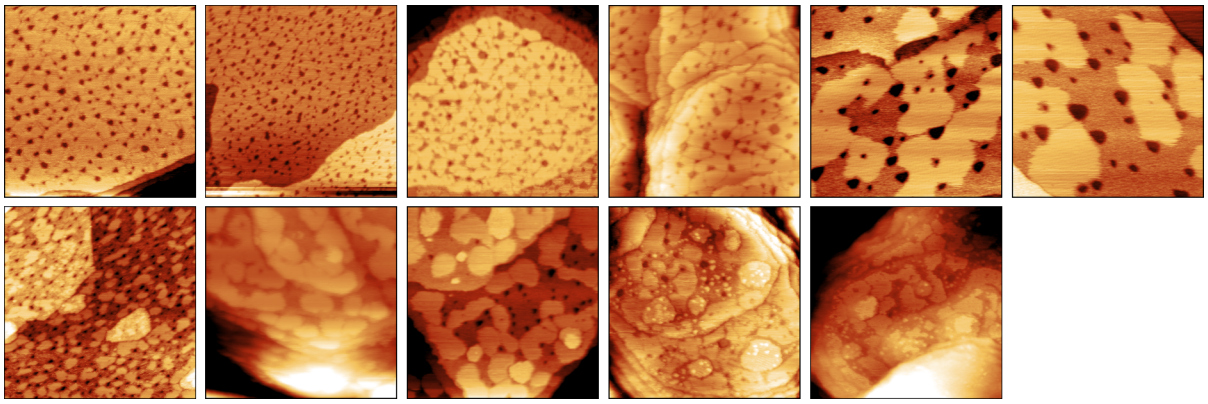

Figure C.7: STM images used to analyse ϕ-phase domain size as a function of thiolate chain length during the SAM's reaction with atomic H (**Figure 4.4**). All images are 200 nm $\times$ 200 nm in size. File names: 2018_04_17_SplitCrystal_8C_0min0012,
2020_12_04_8C-PHA-RT-SOAK-2-DROPS-250K-loc10005,
2018_05_11_5SplitCrystal_10C_0min0014, 2020_02_20_10C-key-250K-0min0008,
2020_10_29_8C-PHASIS-H-anneal-BUBBLE-295K-55min-loc20029,
2020_10_29_8C-PHASIS-H-anneal-BUBBLE-295K-55min-loc20033,
2020_12_13_8C-PHA-RT-SOAK-2-DROPS-250K-225min-loc10030,
2018_11_25_10CSAM_45min_reaction0002, 2018_11_25_10CSAM_45min_reaction0004,
2018_12_11_SAM_150min_250K_Imaged250K0040,
2018_12_11_SAM_150min_250K_Imaged250K0045

Appendix D

Full Published Text (Chapter 5)

The large-scale synthesis of high-quality thin films with extensive tunability derived from molecular building blocks will advance the development of artificial solids with designed functionalities. We report the synthesis of two-dimensional (2D) porphyrin polymer films with wafer-scale homogeneity in the ultimate limit of monolayer thickness by growing films at a sharp pentane/water interface, which allows the fabrication of their hybrid superlattices. Laminar assembly polymerisation of porphyrin monomers could form monolayers of metal-organic frameworks with Cu^{2+} linkers or covalent organic frameworks with terephthalaldehyde linkers. Both the lattice structures and optical properties of these 2D films were directly controlled by the molecular monomers and polymerisation chemistries. The 2D polymers were used to fabricate arrays of hybrid superlattices with molybdenum disulphide that could be used in electrical capacitors.

Monolayer two-dimensional polymers (2DPs), which are one-molecule-thick, freestanding films composed of periodically linked monomers,[86–89] offer an ideal material system with two key advantages. First, their properties can be tuned at the molecular level by using different monomers and polymerisation chemistries.[90;91] Second, as the molecular analogs of 2D atomic crystals (e.g. graphene and transition metal dichalcogenides (TMDs)),[92–94] 2DPs can be assembled through van der Waals (vdW) interactions into heterostructures and superlattices, layer by layer. vdW heterostructures generated from 2D atomic crystals have produced properties not observed in individual building blocks.[95;96] Adding the chemical tunability of the 2DPs to such vdW heterostructures will lead to the properties and functionalities designed at the molecular level and further tuned by the interlayer interactions. However, it has remained an unmet challenge to scalably synthesise monolayer 2DP films and subsequently integrate them with other materials with monolayer precision.[97;98] This is due to the difficulty of controlling

reactions in the monolayer limit with large-scale uniformity and to the lack of facile methods for the transfer and integration of monolayer 2DPs because of their fragility. Previous experiments have reported progress toward large-scale synthesis of 2DPs[99–107] but with limited success with regard to wafer-scale homogeneity, microscopic characterisation of crystalline structures, and scalable thin-film integration.[108]

Here, we report the wafer-scale synthesis and integration of monolayer 2DPs for the fabrication of their hybrid heterostructures with monolayer precision. We developed an interfacial synthesis technique, laminar assembly polymerisation (LAP), that is compatible with various molecular building blocks and two primary polymerisation chemistries (coordination and covalent). This approach incorporated key features necessary for scalable and facile processing, including large-area synthesis, ambient growth conditions, and compatibility with established patterning and integration methods. These characteristics enabled the fabrication of superlattices based on monolayer 2DPs and 2D atomic crystals.

The design approach for the 2DP monolayers was based on porphyrin building blocks (**Figure D.1**A) These molecules had two variation sites: one at the center of the porphyrin ring (**M** = 2H, Fe(III), or Pt(II)) that tuned the optical spectra (**Figure D.1**B) and the other on the phenyl groups (**R** = -COOH or -NH_2) that controlled the monomer-monomer bonds. The monomers were cross-linked either through coordination bonds via a copper paddle wheel structure in the presence of Cu^{2+} ions (**Figure D.1**A, left; **R** = -COOH)[99] or through covalent bonds via the Schiff base reaction in the presence of terephthalaldehyde (TPA) (**Figure D.1**A, right; **R** = -NH_2).[106] The former forms coordination 2DPs (2DP I-III, **M** = 2H, Pt^{2+}, or Fe^{3+}, respectively), also known as monolayer metal-organic frameworks (MOFs), whereas the latter forms covalent 2DPs (2DP IV, **M** = 2H), also known as monolayer covalent organic frameworks (COFs). The linkage chemistry for all the 2DPs was confirmed by Fourier-transform infrared spectroscopy (FTIR).

Wafer-scale 2DP films were all produced at a sharp pentane-water interface and then transferred onto a substrate (e.g. fused silica in **Figure D.1**) placed underneath by slowly draining the bottom solution. We visualised these films using a custom colour-coding scheme based on the hyperspectral optical transmission images (**Figure D.1**C). Images of four transferred 2DP monolayers that covered an entire 2 in (5 cm) fused silica substrate are shown in **Figure D.1**D.

The films displayed uniform contrast over entire wafers, suggesting macroscopic continuity and homogeneity. The MOF-based 2DP I-III with different **M** had distinct absorption spectra (**Figure D.1**B), resulting in markedly different colours (shown in **Figure D.1**D). The absorption spectra of the 2DPs resembled those of the corresponding porphyrin monomers, indicating that the optical properties of the 2DP films could be directly tuned at the molecular level.

These monolayer 2DPs were synthesised using the LAP explained in **Figure D.2**. It is based on monomer self-assembly and polymerisation at the sharp interface formed between two immiscible solvents (pentane/water) that strictly confined the monomers in a monolayer limit, which was critical for precise control of the thickness (**Figures D.2**A and B). Laminar flow of the assembled monomers led to large-scale continuity and homogeneity in thickness (**Figure D.2**A describes the LAP synthesis and the in situ optical characterisation apparatus).

There are three phases in the LAP process (illustrated in **Figures D.2**A and B): injection, self-assembly, and polymerisation. During injection, the monomers were introduced from the edge of the reactor (width W) and directly delivered onto the sharp pentane/water interface by a continuous stream of carrier solution through the pentane layer (within 1 cm from the edge). The pentane-mediated delivery has two key advantages. First, the mass flow of the precursor is continuous at the interface, which is achieved by using microsyringe pumps and by carefully choosing the combination of the carrier solvents. Second, the pentane/water interface is steady during the growth, resulting in minimal disturbance. This contrasts with dropwise delivery through the air, which disturbs the interface. Once delivered to the interface, the porphyrin-based monomers self-assembled at the interface because of their amphiphilicity and then spread, while being restricted by the longer sidewalls (length L). This process generated laminar flow of the monomers away from the injection region and resulted in a continuous monolayer assembly. Then, the polymerisation of assembled monomers takes place gradually through the reaction with the reagents present in water (Cu^{2+} ions for MOF-based 2DP I-III; TPA for COF-based 2DP IV).

The monolayer nature of the 2DPs was confirmed by optical images that showed unidirectional movement of the monolayer assembly parallel to the longer sidewalls (**Figure D.2**C) with little mixing perpendicular to this direction (**Figure D.2**F), confirming a laminar flow. This monolayer remained intact upon solvent washing after a complete polymerisation ($\sim$30 min); in

contrast, unpolymerised films were washed away (**Figure D.2**D). Quantitative measurements of the synthesised area of 2DP I (**R** = -COOH and **M** = 2H with Cu^{2+} ions) as a function of the injected volume of the monomer solution closely followed a linear growth model consistent with a near-unity monomer-to-monolayer yield (**Figure D.2**E).

The LAP synthesis offers several advantages important for thin-film processing and integration of 2DP monolayers. First, the growth can be easily scaled up by injecting more monomers (for greater L) and by adding an array of nozzles in parallel (for greater W). For example, the 2 in films shown in **Figure D.1**D were synthesised with three nozzles in a 2 in (W) by 5 in (L) reactor. Second, lateral heterojunctions of monolayer 2DPs can be grown with tunable compositions and widths by introducing different monomers from each nozzle and by controlling the relative injection rates (**Figures D.2**F and G). Sharp interfaces between adjacent monolayer stripes were observed without voids. Finally, the 2DP films were compatible with a wide range of patterning and transfer techniques. For instance, they could be transferred to various substrates without tearing, distortion, or buckling after evaporating pentane (e.g. SiO_2/Si in **Figure D.3**B and gold in **Figure D.3**D), and they could be patterned by using a laser marker while still on the water surface with a scanning laser. Multiple patterning and transfer steps can be combined to fabricate laterally patterned and vertically stacked heterostructures while maintaining the integrity of the intricate patterns, as shown in **Figure D.2**H.

The 2DP films were mechanically robust and homogeneous in thickness. On the large scale, they exhibited considerable mechanical strength and could be transferred onto various substrates as continuous films, as shown in **Figure D.1**D. As an additional example, a scanning electron microscopy (SEM) image of a 2DP I film transferred and suspended over a holey transmission electron microscope (TEM) grid (2 μm-diameter holes) (**Figure D.3**A) displays an array of freestanding 2DP membranes. These membranes were suspended with a near-perfect yield (> 99%; one broken membrane, denoted by an arrow) and appeared uniform and continuous over the entire area without cracks or voids. These 2DP films were close to 1 nm in height, near the expected thickness of a monolayer,[133] with a uniform and smooth surface as measured by atomic force microscopy (**Figure D.3**B).

The MOF-based 2DP I-III showed a polycrystalline structure, which was confirmed by synchrotron grazing incidence X-ray diffraction (GIXRD) (**Figure D.3**C). Using 2DP II as an

example, the in-plane XRD pattern showed all of the main peaks predicted on the basis of the structure model (inset in **Figure D.3**C), and the average lateral domain size was estimated to be ~20 nm according to the Scherrer equation. As additional evidence, the crystalline structure of 2DP II monolayers transferred onto flat Au(111) surfaces was confirmed with scanning tunnelling microscopy (STM) performed under ultrahigh vacuum. The STM topography image (**Figure D.3**D) showed a square lattice with a single crystalline domain that fully covered the 30 nm × 30 nm area (see the 2D fast Fourier transform (FFT) image (inset in **Figure D.3**D)). Another STM image (**Figure D.3**E; 60 nm × 60 nm) displayed three primary crystalline orientations (lattice constant a = 1.66 ± 0.03 nm (mean ± standard error of the mean), measured from **Figure D.3**F), suggesting that the 2DP II films are polycrystalline with domain structures similar to those in previously imaged 2DPs.[109;110] The lattice constant extracted from these microscopic STM analyses is close to that from GIXRD measurements (1.64 nm) performed on the macroscopic scale (0.1 mm × 10 mm) with a mismatch less than 2% (**Figure D.3**C). In the composite inverse 2D FFT image in **Figure D.3**G, each region is coloured according to the lattice orientation. We used this map to estimate the sizes of domains (between 10 and 40 nm) and locate domain boundaries (marked by dashed lines in **Figure D.3**E). For the COF-based 2DP IV, no evidence for long-range order could be collected (through GIXRD or selected area electron diffraction), similar to other monolayer covalent 2DPs reported previously.[110]

In **Figure D.4**, we further demonstrate the potential of LAP by presenting an array of vertically programmed hybrid vdW superlattices. These superlattices were produced by repeatedly stacking in vacuum hybrid 2D building units 2DP/$(MoS_2)_n$, each made of a 2DP monolayer and n monolayers of MoS_2. Examples of a 2DP II/$(MoS_2)_3$ superlattice and a 2DP II/MoS_2 film are shown in **Figures D.4**A and B, respectively.[134;135] **Figure D.4**A shows a cross-sectional annular dark field (ADF) scanning transmission electron microscope (STEM) image of a representative 2DP II/$(MoS_2)_3$ superlattice – an 11-layer stack – constructed by alternating one layer of 2DP II and three layers of MoS_2. The image shows three bright bands separated by two dark lines. Each of the bright bands consisted of three layers of MoS_2, and the dark layer in between corresponds to a 2DP II monolayer, as confirmed by the composite ADF and electron energy loss spectroscopy (EELS) mapping (**Figure D.4**A). The films ran parallel to each other with sharp interfaces and a uniform layer thickness over the entire 100 nm view of the ADF STEM image, indicating a high

level of uniformity. In addition, the composition of the superlattice could be tuned by using a different 2DP, as demonstrated with the 2DP III/$(MoS_2)_2$ superlattice shown in **Figure D.4**C. EELS data confirmed the chemical composition of each constituting layer, where 2DP III was identified by a strong carbon signal and MoS_2 by a strong sulphur signal (**Figure D.4**C).

The vertical structure and composition of the hybrid vdW superlattices could be directly engineered by using different hybrid building units. **Figure D.4**D (left) shows a series of vdW superlattices with varied superlattice periodicity d made of 2DP II/$(MoS_2)_n$ repeating units, with n = 1, 2, or 3. The grazing incidence wide-angle X-ray scattering (GIWAXS) data presented in **Figure D.4**D (middle and right) show the distinctive diffraction peak for each superlattice. By radially integrating the 2D GIWAXS images along the out-of-plane direction, 1D spectra were obtained in reciprocal space and used to measure d. For example, the superlattice with n = 3 showed d = 3.5 nm and a vdW thickness of 1.5 nm for 2DP II, which was close to the value measured from **Figure D.4**A. The results from other superlattices agreed very well with the predicted values. In addition, X-ray reflectivity (XRR) measurements conducted on similar superlattice structures and the scattering length density profiles generated from fitting the XRR spectra clearly revealed oscillations of electron density consistent with the alternating structures of $(MoS_2)_n$ and 2DP II. The thickness of the repeating units extracted from the XRR analysis matched those obtained from GIWAXS and cross-sectional STEM within a 2 Å mismatch. Both the GIWAXS and the XRR data were taken from a macroscopic area randomly chosen from 1 cm $\times$ 1 cm superlattice films, illustrating the homogeneity of the vdW superlattices on a large scale.

Vertically programmed vdW superlattices and heterostructures provide a powerful platform for fabricating uniform arrays of devices whose properties are engineered layer by layer.[95;96;136–139] To demonstrate such potential, we chose to fabricate arrays of electrical capacitors (photo shown in **Figure D.4**F) from vdW heterostructures of 2DP II and MoS_2 (**Figure D.4**E), as such a process involves integration of both top and bottom electrodes and the capacitance can be directly tuned by the thickness of the superlattices. Each device in an array consisted of two gold electrodes sandwiching the vdW heterostructure dielectric.[134] **Figure D.4**G shows the results measured from a series of heterostructures, $(MoS_2/\text{2DP II})_N(MoS_2)_{6-N}$, where N monolayers of 2DP II films were inserted in between MoS_2 layers of a six-layer MoS_2 stack (schematics in **Figure D.4**G). Thus, the dielectric thickness and the capacitance are directly

tuned by varying the layer number of monolayer 2DP II. The measured inverse capacitance, $1/C'$, where C' is the area-normalised capacitance, linearly increased as N increased from 1 to 5. Using the classical capacitor model, we extracted the dielectric constants of 2DP II (4.1) and MoS_2 (2.7), and these were in agreement with reported values.[140;141] The measured capacitance from an array of devices exhibited a narrow distribution (lower inset in **Figure D.4**G), suggesting the spatial uniformity of the hybrid heterostructures. This spatial uniformity is comparable to what has been achieved with stacked MoS_2 films.[134] Thus, this method offers a general platform to incorporate diverse molecular species into vdW hybrid thin films for functional devices.

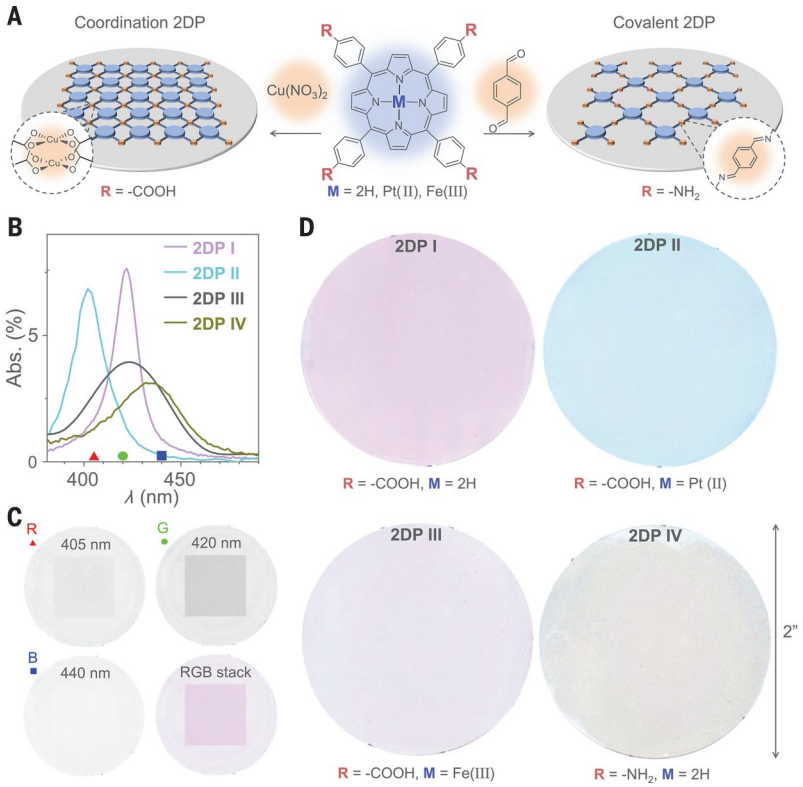

Figure D.1: Wafer-scale monolayer 2DPs. (A) Schematic of monolayer 2DPs and corresponding chemical structures of the molecular precursors. (B) Absorption spectra of monolayer 2DPs on fused silica substrates. (C) Hyperspectral transmission images and resulting false-colour images of 1-inch-square 2DP I on a 2-inch fused silica substrate. Transmission images taken at the wavelengths of 405, 420, and 440 nm were assigned red, green, and blue channels, respectively, to generate the false-colour image. A linear transmission scale of 50 to 95% was applied to all of the channels. (D) False-colour images of monolayer 2DPs covering entire 2-inch fused silica wafers. The same colour code was applied in (C) and (D).

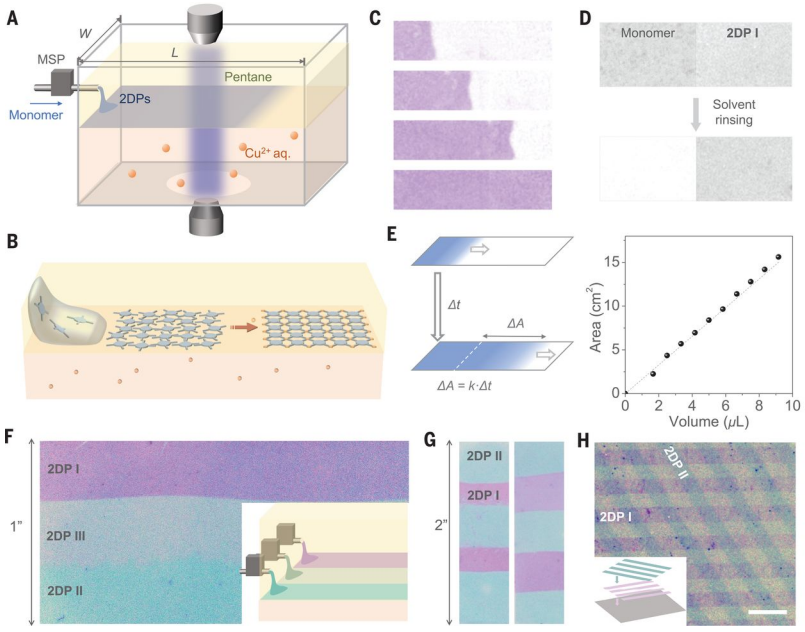

Figure D.2: Laminar assembly polymerisation. (A) Schematic of a LAP reactor and in situ optical characterisation apparatus. MSP, microsyringe pump. (B) Schematic of the LAP synthesis that involves three phases. (C) False-colour images of 2DP I film at four different stages during growth. The precursor was injected from the left side. The film was coloured with purple. The view size is 6 mm by 24 mm. (D) Optical transmission images comparing monolayer films produced with and without Cu^{2+} ions before and after rinsing, measured at the wavelength of 425 nm. Image size is 0.67 cm $\times$ 1 cm. (E) (Left) Schematic of a linear growth model based on LAP. The film area increases linearly over time with a rate constant $k = C_N \cdot A_0 \cdot v \cdot \eta / N_{eff}$, where C_N is number concentration of the molecular precursor, A_0 is the unit cell area of the 2DP I lattice, v is the volumetric injection rate, η is the monomer-to-monolayer yield, and N_{eff} is the effective layer number. (Right) Relation between film area and volume of the injected precursor, measured for 2DP I. The dashed line indicates the theoretical curve for 100% monomer-to-monolayer conversion based on the lattice structure of 2DP I (η = 100%, N_{eff} = 1). (F) False-colour image of 2DP I/2DP III/2DP II lateral junctions. (Inset) Schematic of generating lateral heterostructures of 2DP I/2DP III/2DP II generated using three nozzles in LAP. (G) False-color images of 2DP I/2DP II lateral junctions with tunable stripe widths. (H) False-colour image of overlapped 2DP I and 2DP II stripes. Scale bar, 500 μm.

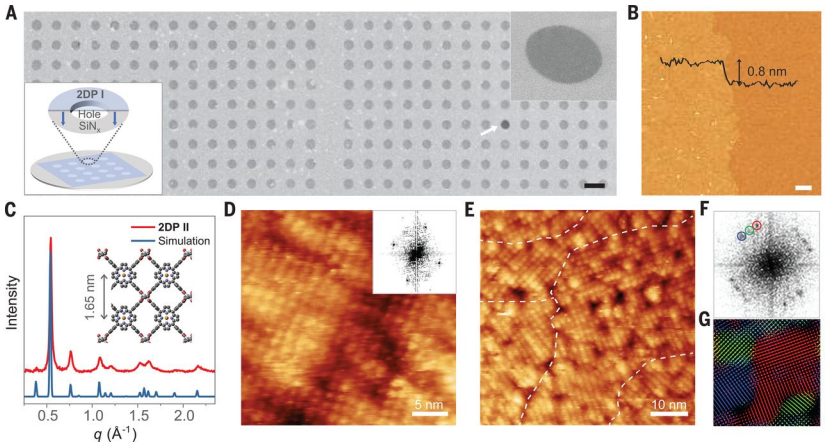

Figure D.3: Structural characterisations of 2DPs. (A) SEM image of monolayer 2DP I on a holey silicon nitride TEM grid. The white arrow indicates a hole not covered by monolayer 2DP I. Scale bar, 5 μm. (Bottom left inset) Schematic of monolayer 2DP I suspended over a hole on a silicon nitride TEM grid. (Top right inset) Magnified SEM image of monolayer 2DP I suspended over a 2 μm hole. (B) AFM height image of monolayer 2DP I. Scale bar, 500 nm. (Inset) AFM height profile. (C) Experimental and calculated in-plane XRD profiles for 2DP II. The experiment was conducted on a stacked 2DP II of 147 layers on sapphire. (Inset) Crystal structure of 2DP II. (D) Constant-current STM topography image of a single-crystalline domain of monolayer 2DP II on a thin film of Au(111)-on-mica. (Inset) 2D FFT of the image. (E) Constant-current STM topography image of multiple crystalline domains of monolayer 2DP II. Boundaries between different domains are manually identified by the white dashed line. (F) 2D FFT of (E) showing square lattices of three major orientations. (G) Colour-coded inverse 2D FFT image generated using the three sets of square lattice spots in (F). One spot from each set is circled with the corresponding colour in (F).

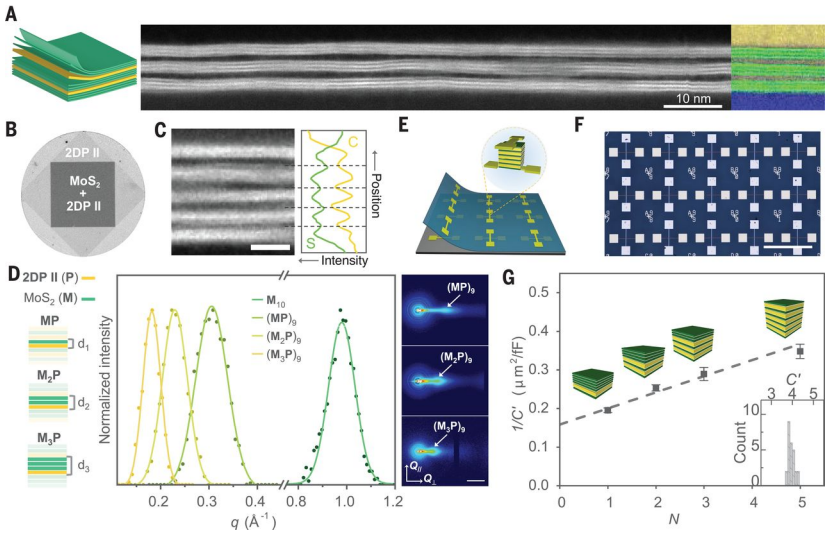

Figure D.4: 2DP/TMD vertical superlattices. (A) (Left) Schematic of a 2DP/$(MoS_2)_3$ superlattice. (Middle) Cross-sectional ADF STEM image of a 2DP II/$(MoS_2)_3$ superlattice film transferred onto a SiO_2/Si substrate. Each bright band consists of three MoS_2 monolayers, and each dark layer between the bands is a monolayer 2DP II. (Right) Composite image of carbon (yellow) and oxygen (blue) EELS mapping and ADF STEM signal (green). (B) Optical transmission image of a 2DP II/MoS_2 heterostructure on fused silica taken at the wavelength of 405 nm. The diameter of the wafer is 1 in. (C) (Left) Cross-sectional ADF STEM image of a 2DP III/$(MoS_2)_2$ superlattice film transferred onto a SiO_2/Si substrate. Each bright layer consists of two layers of MoS_2 stacked, and each dark layer is a 2DP III monolayer. (Right) EELS profiles of carbon and sulphur. Scale bar, 5 nm. (D) (Left) Structures of 2DP II/$(MoS_2)_n$ vertical superlattices. (Middle) Normalised diffraction peaks corresponding to 2DP II/$(MoS_2)_n$ superlattices measured by GIWAXS. (Right) 2D GIWAXS scattering patterns of 2DP II/$(MoS_2)_n$ superlattices. Scale bar, 0.2 $Å^{-1}$. (E) Schematic of vertical capacitor device arrays and individual device geometry. (F) Optical image of a 3×5 capacitor device array. Scale bar, 500 μm. (G) Reciprocal of area-normalised capacitance, $1/C'$, as a function of N, the number of 2DP II layers in stacked $(MoS_2/\text{2DP II})_N(MoS_2)_{6-N}$ films. Each data point is averaged from ten devices with corresponding stacked film structures shown above. Green, MoS_2; yellow, **2DP II**. The inset shows a capacitance histogram of 25 devices of $N = 2$.

References

[1] Caro, A. M.; Armini, S.; Richard, O.; Maes, G.; Borghs, G.; Whelan, C. M.; Travaly, Y. Bottom-Up Engineering of Subnanometer Copper Diffusion Barriers Using NH2-Derived Self-Assembled Monolayers. *Advanced Functional Materials* **2010**, *20*, 1125–1131.

[2] Onclin, S.; Ravoo, B. J.; Reinhoudt, D. N. Engineering silicon oxide surfaces using self-assembled monolayers. *Angewandte Chemie International Edition* **2005**, *44*, 6282–6304.

[3] Holzweber, M.; Heinrich, T.; Kunz, V.; Richter, S.; Traulsen, C. H.-H.; Schalley, C. A.; Unger, W. E. Principal component analysis (PCA)-assisted time-of-flight secondary-ion mass spectrometry (ToF-SIMS): a versatile method for the investigation of self-assembled monolayers and multilayers as precursors for the bottom-up approach of nanoscaled devices. *Analytical chemistry* **2014**, *86*, 5740–5748.

[4] Smits, E. C.; Mathijssen, S. G.; Van Hal, P. A.; Setayesh, S.; Geuns, T. C.; Mutsaers, K. A.; Cantatore, E.; Wondergem, H. J.; Werzer, O.; Resel, R., et al. Bottom-up organic integrated circuits. *Nature* **2008**, *455*, 956–959.

[5] Seo, S.; Hwang, E.; Cho, Y.; Lee, J.; Lee, H. Functional Molecular Junctions Derived from Double Self-Assembled Monolayers. *Angewandte Chemie* **2017**, *129*, 12290–12294.

[6] Zacher, D.; Shekhah, O.; Wöll, C.; Fischer, R. A. Thin films of metal–organic frameworks. *Chemical Society Reviews* **2009**, *38*, 1418–1429.

[7] Mantis Deposition LTD, MCG75 Thermal Gas Cracker Operations Manual. 2017.

[8] Binnig, G. K.; Rohrer, H. Scanning tunneling microscopy–from birth to adolescence. *Uspekhi Fizicheskikh Nauk* **1988**, *154*, 261–278.

[9] Binnig, G.; Rohrer, H.; Salvan, F.; Gerber, C.; Baro, A. Revisiting the 7$\times$ 7 reconstruction of Si (111). *Surface Science Letters* **1985**, *157*, L373–L378.

[10] Hipps, K. *Handbook of Applied Solid State Spectroscopy*; Springer, 2006; pp 305–350.

[11] Nečas, D.; Klapetek, P. Gwyddion: an open-source software for SPM data analysis. *Open Physics* **2012**, *10*, 181–188.

[12] Zharnikov, M.; Geyer, W.; Gölzhäuser, A.; Frey, S.; Grunze, M. Modification of alkanethiolate monolayers on Au-substrate by low energy electron irradiation: Alkyl chains and the S/Au interface. *Physical Chemistry Chemical Physics* **1999**, *1*, 3163–3171.

[13] Sayler, J. D.; Brown, S.; Sibener, S. Chain-length-dependent reactivity of alkanethiolate self-assembled monolayers with atomic hydrogen. *The Journal of Physical Chemistry C* **2019**, *123*, 26932–26938.

[14] Ulman, A. Formation and structure of self-assembled monolayers. *Chemical reviews* **1996**, *96*, 1533–1554.

[15] Poirier, G.; Pylant, E. The self-assembly mechanism of alkanethiols on Au (111). *Science* **1996**, *272*, 1145–1148.

[16] Poirier, G. E. Characterization of organosulfur molecular monolayers on Au (111) using scanning tunneling microscopy. *Chemical reviews* **1997**, *97*, 1117–1128.

[17] Häkkinen, H. The gold–sulfur interface at the nanoscale. *Nature chemistry* **2012**, *4*, 443–455.

[18] DiMilla, P. A.; Folkers, J. P.; Biebuyck, H. A.; Haerter, R.; Lopez, G. P.; Whitesides, G. M. Wetting and protein adsorption on self-assembled monolayers of alkanethiolates supported on transparent films of gold. *Journal of the American Chemical Society* **1994**, *116*, 2225–2226.

[19] Devi, J. M. A simulation study on the thermal and wetting behavior of alkane thiol SAM on gold (111) surface. *Progress in Natural Science: Materials International* **2014**, *24*, 405–411.

[20] Gleiche, M.; Chi, L. F.; Fuchs, H. Nanoscopic channel lattices with controlled anisotropic wetting. *Nature* **2000**, *403*, 173–175.

[21] Laibinis, P. E.; Whitesides, G. M.; Allara, D. L.; Tao, Y. T.; Parikh, A. N.; Nuzzo, R. G. Comparison of the structures and wetting properties of self-assembled monolayers of n-alkanethiols on the coinage metal surfaces, copper, silver, and gold. *Journal of the American Chemical Society* **1991**, *113*, 7152–7167.

[22] Raynor, J. E.; Capadona, J. R.; Collard, D. M.; Petrie, T. A.; García, A. J. Polymer brushes and self-assembled monolayers: Versatile platforms to control cell adhesion to biomaterials. *Biointerphases* **2009**, *4*, FA3–FA16.

[23] Kondo, T.; Uosaki, K. Self-assembled monolayers (SAMs) with photo-functionalities. *Journal of Photochemistry and Photobiology C: Photochemistry Reviews* **2007**, *8*, 1–17.

[24] Plant, A. L. Self-assembled phospholipid/alkanethiol biomimetic bilayers on gold. *Langmuir* **1993**, *9*, 2764–2767.

[25] Prime, K. L.; Whitesides, G. M. Adsorption of proteins onto surfaces containing end-attached oligo (ethylene oxide): a model system using self-assembled monolayers. *Journal of the American Chemical Society* **1993**, *115*, 10714–10721.

[26] Zamborini, F. P.; Crooks, R. M. Corrosion passivation of gold by n-alkanethiol self-assembled monolayers: effect of chain length and end group. *Langmuir* **1998**, *14*, 3279–3286.

[27] Yourdshahyan, Y.; Zhang, H.; Rappe, A. n-alkyl thiol head-group interactions with the Au (111) surface. *Physical Review B* **2001**, *63*, 081405.

[28] Gorham, J.; Smith, B.; Fairbrother, D. H. Modification of alkanethiolate self-assembled monolayers by atomic hydrogen: Influence of alkyl chain length. *The Journal of Physical Chemistry C* **2007**, *111*, 374–382.

[29] Sieval, A. B.; Huisman, C. L.; Schönecker, A.; Schuurmans, F. M.; van der Heide, A. S.; Goossens, A.; Sinke, W. C.; Zuilhof, H.; Sudhölter, E. J. Silicon surface passivation by organic monolayers: minority charge carrier lifetime measurements and Kelvin probe investigations. *The Journal of Physical Chemistry B* **2003**, *107*, 6846–6852.

[30] Love, J. C.; Estroff, L. A.; Kriebel, J. K.; Nuzzo, R. G.; Whitesides, G. M. Self-assembled monolayers of thiolates on metals as a form of nanotechnology. *Chemical reviews* **2005**, *105*, 1103–1170.

[31] Gorham, J. M.; Stover, A. K.; Fairbrother, D. H. Modification of 1 H, 1 H, 2 H, 2 H-Perfluorooctyltrichlorosilane Self-Assembled Monolayers by Atomic Hydrogen. *The Journal of Physical Chemistry C* **2007**, *111*, 18663–18671.

[32] Jobbins, M. M.; Raigoza, A. F.; Kandel, S. A. Adatoms at the Sulfur–Gold Interface in 1-Adamantanethiolate Monolayers, Studied Using Reaction with Hydrogen Atoms and Scanning Tunneling Microscopy. *The Journal of Physical Chemistry C* **2011**, *115*, 25437–25441.

[33] Kautz, N. A.; Kandel, S. A. Alkanethiol monolayers contain gold adatoms, and adatom coverage is independent of chain length. *The Journal of Physical Chemistry C* **2009**, *113*, 19286–19291.

[34] Kautz, N. A.; Kandel, S. A. Alkanethiol/Au (111) self-assembled monolayers contain gold adatoms: Scanning tunneling microscopy before and after reaction with atomic hydrogen. *Journal of the American Chemical Society* **2008**, *130*, 6908–6909.

[35] Kautz, N. A.; Fogarty, D. P.; Kandel, S. A. Degradation of octanethiol self-assembled monolayers from hydrogen-atom exposure: A molecular-scale study using scanning tunneling microscopy. *Surface science* **2007**, *601*, L86–L90.

[36] Lee, D. Y.; Kautz, N. A.; Kandel, S. A. Reactivity of Gas-Phase Radicals with Organic Surfaces. *The Journal of Physical Chemistry Letters* **2013**, *4*, 4103–4112.

[37] Kautz, N. A.; Kandel, S. A. Reactivity of self-assembled monolayers: Local surface environment determines monolayer erosion rates. *The Journal of Physical Chemistry C* **2012**, *116*, 4725–4731.

[38] Layfield, J. P.; Troya, D. Theoretical study of the dynamics of F+ alkanethiol self-assembled monolayer hydrogen-abstraction reactions. *The Journal of chemical physics* **2010**, *132*, 134307.

[39] Yuan, H.; Gibson, K.; Li, W.; Sibener, S. Modification of Alkanethiolate Monolayers by O (3P) Atomic Oxygen: Effect of Chain Length and Surface Temperature. *The Journal of Physical Chemistry B* **2013**, *117*, 4381–4389.

[40] Waring, C.; Bagot, P. A.; Räisänen, M. T.; Costen, M. L.; McKendrick, K. G. Dynamics of the reaction of O (3P) atoms with alkylthiol self-assembled monolayers. *The Journal of Physical Chemistry A* **2009**, *113*, 4320–4329.

[41] Wagner, A.; Wolfe, G.; Fairbrother, D. Atomic oxygen reactions with semifluorinated and n-alkanethiolate self-assembled monolayers. *The Journal of chemical physics* **2004**, *120*, 3799–3810.

[42] Torres, J.; Perry, C. C.; Bransfield, S. J.; Fairbrother, D. H. Radical reactions with organic thin films: chemical interaction of atomic oxygen with an X-ray modified self-assembled monolayer. *The Journal of Physical Chemistry B* **2002**, *106*, 6265–6272.

[43] Waring, C.; Bagot, P. A.; Bebbington, M. W.; Räisänen, M. T.; Buck, M.; Costen, M. L.; McKendrick, K. G. How penetrable are thioalkyl self-assembled monolayers? *The Journal of Physical Chemistry Letters* **2010**, *1*, 1917–1921.

[44] Fiegland, L. R.; McCorn Saint Fleur, M.; Morris, J. R. Reactions of C C-Terminated Self-Assembled Monolayers with Gas-Phase Ozone. *Langmuir* **2005**, *21*, 2660–2661.

[45] Norrod, K. L.; Rowlen, K. L. Ozone-induced oxidation of self-assembled decanethiol: Contributing mechanism for "photooxidation"? *Journal of the American Chemical Society* **1998**, *120*, 2656–2657.

[46] Poirier, G. E.; Herne, T. M.; Miller, C. C.; Tarlov, M. J. Molecular-scale characterization of the reaction of ozone with decanethiol monolayers on Au (111). *Journal of the American Chemical Society* **1999**, *121*, 9703–9711.

[47] Fitts, W.; White, J.; Poirier, G. Low-coverage decanethiolate structure on Au (111): Substrate effects. *Langmuir* **2002**, *18*, 1561–1566.

[48] Picraux, L. B.; Zangmeister, C. D.; Batteas, J. D. Preparation and structure of a low-density, flat-lying decanethiol monolayer from the densely packed, upright monolayer on gold. *Langmuir* **2006**, *22*, 174–180.

[49] Poirier, G.; Fitts, W.; White, J. Two-dimensional phase diagram of decanethiol on Au (111). *Langmuir* **2001**, *17*, 1176–1183.

[50] Camillone Iii, N.; Eisenberger, P.; Leung, T.; Schwartz, P.; Scoles, G.; Poirier, G.; Tarlov, M. New monolayer phases of n-alkane thiols self-assembled on Au (111): Preparation, surface characterization, and imaging. *The Journal of chemical physics* **1994**, *101*, 11031–11036.

[51] Poirier, G.; Tarlov, M. The c (4×2) superlattice of n-alkanethiol monolayers self-assembled on Au (111). *Langmuir* **1994**, *10*, 2853–2856.

[52] Widrig, C. A.; Alves, C. A.; Porter, M. D. Scanning tunneling microscopy of ethanethiolate and n-octadecanethiolate monolayers spontaneously absorbed at gold surfaces. *Journal of the American Chemical Society* **1991**, *113*, 2805–2810.

[53] Poirier, G. Coverage-dependent phases and phase stability of decanethiol on Au (111). *Langmuir* **1999**, *15*, 1167–1175.

[54] Tao, F.; Bernasek, S. L. Understanding odd- even effects in organic self-assembled monolayers. *Chemical reviews* **2007**, *107*, 1408–1453.

[55] Wong, S.-S.; Takano, H.; Porter, M. D. Mapping orientation differences of terminal functional groups by friction force microscopy. *Analytical Chemistry* **1998**, *70*, 5209–5212.

[56] Poirier, G.; Tarlov, M.; Rushmeier, H. Two-dimensional liquid phase and the p $\times\sqrt{3}$ phase of alkanethiol self-assembled monolayers on Au (111). *Langmuir* **1994**, *10*, 3383–3386.

[57] Poirier, G.; Tarlov, M. Molecular ordering and gold migration observed in butanethiol self-assembled monolayers using scanning tunneling microscopy. *The Journal of Physical Chemistry* **1995**, *99*, 10966–10970.

[58] Brown, S.; Sayler, J. D.; Sibener, S. Influence of Structural Dynamics on the Kinetics of Atomic Hydrogen Reactivity with Low-Temperature Alkanethiolate Self-Assembled Monolayers. *The Journal of Physical Chemistry C* **2021**,

[59] Laibinis, P. E.; Whitesides, G. M. Self-assembled monolayers of n-alkanethiolates on copper are barrier films that protect the metal against oxidation by air. *Journal of the American Chemical Society* **1992**, *114*, 9022–9028.

[60] Robinson, G. N.; Freedman, A.; Graham, R. L. Reactions of fluorine atoms with self-assembled monolayers of alkanethiolates. *Langmuir* **1995**, *11*, 2600–2608.

[61] Scherer, J.; Vogt, M.; Magnussen, O.; Behm, R. Corrosion of alkanethiol-covered Cu (100) surfaces in hydrochloric acid solution studied by in-situ scanning tunneling microscopy. *Langmuir* **1997**, *13*, 7045–7051.

[62] Burleigh, T.; Gu, Y.; Donahey, G.; Vida, M.; Waldeck, D. Tarnish protection of silver using a hexadecanethiol self-assembled monolayer and descriptions of accelerated tarnish tests. *Corrosion* **2001**, *57*, 1066–1074.

[63] Jennings, G. K.; Yong, T.-H.; Munro, J. C.; Laibinis, P. E. Structural effects on the barrier properties of self-assembled monolayers formed from long-chain ω-alkoxy-n-alkanethiols on copper. *Journal of the American Chemical Society* **2003**, *125*, 2950–2957.

[64] Lim, H.; Carraro, C.; Maboudian, R.; Pruessner, M. W.; Ghodssi, R. Chemical and thermal stability of alkanethiol and sulfur passivated InP (100). *Langmuir* **2004**, *20*, 743–747.

[65] Tortech, L.; Mekhalif, Z.; Delhalle, J.; Guittard, F.; Geribaldi, S. Self-assembled monolayers of semifluorinated thiols on electrochemically modified polycrystalline nickel surfaces. *Thin Solid Films* **2005**, *491*, 253–259.

[66] McGuiness, C. L.; Shaporenko, A.; Zharnikov, M.; Walker, A. V.; Allara, D. L. Molecular Self-Assembly at Bare Semiconductor Surfaces: Investigation of the Chemical and Electronic Properties of the Alkanethiolate- GaAs (001) Interface. *The Journal of Physical Chemistry C* **2007**, *111*, 4226–4234.

[67] Hautman, J.; Klein, M. L. Molecular dynamics simulation of the effects of temperature on a dense monolayer of long-chain molecules. *The Journal of chemical physics* **1990**, *93*, 7483–7492.

[68] Mar, W.; Klein, M. L. Molecular dynamics study of the self-assembled monolayer composed of $S(CH_2)_{14}CH_3$ molecules using an all-atoms model. *Langmuir* **1994**, *10*, 188–196.

[69] Bhatia, R.; Garrison, B. J. Phase transitions in a methyl-terminated monolayer self-assembled on Au (111). *Langmuir* **1997**, *13*, 765–769.

[70] Rai, B.; Sathish, P.; Malhotra, C. P.; Pradip,; Ayappa, K. Molecular dynamic simulations of self-assembled alkylthiolate monolayers on an Au (111) surface. *Langmuir* **2004**, *20*, 3138–3144.

[71] Camillone III, N.; Chidsey, C. E.; Liu, G.-y.; Putvinski, T.; Scoles, G. Surface structure and thermal motion of n-alkane thiols self-assembled on Au (111) studied by low energy helium diffraction. *The Journal of chemical physics* **1991**, *94*, 8493–8502.

[72] Nuzzo, R. G.; Korenic, E. M.; Dubois, L. H. Studies of the temperature-dependent phase behavior of long chain n-alkyl thiol monolayers on gold. *The Journal of chemical physics* **1990**, *93*, 767–773.

[73] Fenter, P.; Eisenberger, P.; Liang, K. Chain-length dependence of the structures and phases of $CH_3(CH_2)_{n-1}SH$ self-assembled on Au (111). *Physical review letters* **1993**, *70*, 2447.

[74] Day, B. S.; Morris, J. R. Packing density and structure effects on energy-transfer dynamics in argon collisions with organic monolayers. *The Journal of chemical physics* **2005**, *122*, 234714.

[75] Day, B. S.; Morris, J. R.; Alexander, W. A.; Troya, D. Theoretical study of the effect of surface density on the dynamics of Ar+ alkanethiolate self-assembled monolayer collisions. *The Journal of Physical Chemistry A* **2006**, *110*, 1319–1326.

[76] Vericat, C.; Vela, M.; Benitez, G.; Carro, P.; Salvarezza, R. Self-assembled monolayers of thiols and dithiols on gold: new challenges for a well-known system. *Chemical Society Reviews* **2010**, *39*, 1805–1834.

[77] Vericat, C.; Vela, M. E.; Corthey, G.; Pensa, E.; Cortés, E.; Fonticelli, M. H.; Ibanez, F.; Benitez, G.; Carro, P.; Salvarezza, R. C. Self-assembled monolayers of thiolates on metals: a review article on sulfur-metal chemistry and surface structures. *Rsc Advances* **2014**, *4*, 27730–27754.

[78] Paz, Y.; Trakhtenberg, S.; Naaman, R. Reaction between O (3P) and organized organic thin films. *The Journal of Physical Chemistry* **1994**, *98*, 13517–13523.

[79] Feulner, P.; Niedermayer, T.; Eberle, K.; Schneider, R.; Menzel, D.; Baumer, A.; Schmich, E.; Shaporenko, A.; Tai, Y.; Zharnikov, M. Strong temperature dependence of irradiation effects in organic layers. *Physical review letters* **2004**, *93*, 178302.

[80] Mulder, W. H.; Calvente, J. J.; Andreu, R. A kinetic model for the reductive desorption of self-assembled thiol monolayers. *Langmuir* **2001**, *17*, 3273–3280.

[81] Doudevski, I.; Hayes, W. A.; Schwartz, D. K. Submonolayer island nucleation and growth kinetics during self-assembled monolayer formation. *Physical review letters* **1998**, *81*, 4927.

[82] Vinokurov, I. A.; Morin, M.; Kankare, J. Mechanism of reductive desorption of self-assembled monolayers on the basis of Avrami theorem and diffusion. *The Journal of Physical Chemistry B* **2000**, *104*, 5790–5796.

[83] Dordi, B.; Schönherr, H.; Vancso, G. J. Reactivity in the confinement of self-assembled monolayers: chain length effects on the hydrolysis of N-hydroxysuccinimide ester disulfides on gold. *Langmuir* **2003**, *19*, 5780–5786.

[84] Turner, D. A.; Schalk, C. N.; Kandel, S. A. Atomic Hydrogen Reactions of Alkanethiols on Au (111): Phase Transitions at Elevated Temperatures. *The Journal of Physical Chemistry C* **2020**, *124*, 7139–7143.

[85] Zhong, Y.; Cheng, B.; Park, C.; Ray, A.; Brown, S.; Mujid, F.; Lee, J.-U.; Zhou, H.; Suh, J.; Lee, K.-H., et al. Wafer-scale synthesis of monolayer two-dimensional porphyrin polymers for hybrid superlattices. *Science* **2019**, *366*, 1379–1384.

[86] Servalli, M.; Schlüter, A. D. Synthetic two-dimensional polymers. *Annual Review of Materials Research* **2017**, *47*, 361–389.

[87] Payamyar, P.; King, B. T.; Öttinger, H. C.; Schlüter, A. D. Two-dimensional polymers: concepts and perspectives. *Chemical Communications* **2016**, *52*, 18–34.

[88] Perepichka, D. F.; Rosei, F. Extending polymer conjugation into the second dimension. *Science* **2009**, *323*, 216–217.

[89] Franc, G.; Gourdon, A. Covalent networks through on-surface chemistry in ultra-high vacuum: state-of-the-art and recent developments. *Physical chemistry chemical physics* **2011**, *13*, 14283–14292.

[90] Furukawa, H.; Cordova, K. E.; O'Keeffe, M.; Yaghi, O. M. The chemistry and applications of metal-organic frameworks. *Science* **2013**, *341*.

[91] Waller, P. J.; Gándara, F.; Yaghi, O. M. Chemistry of covalent organic frameworks. *Accounts of chemical research* **2015**, *48*, 3053–3063.

[92] Novoselov, K. S.; Jiang, D.; Schedin, F.; Booth, T.; Khotkevich, V.; Morozov, S.; Geim, A. K. Two-dimensional atomic crystals. *Proceedings of the National Academy of Sciences* **2005**, *102*, 10451–10453.

[93] Mak, K. F.; Lee, C.; Hone, J.; Shan, J.; Heinz, T. F. Atomically thin MoS 2: a new direct-gap semiconductor. *Physical review letters* **2010**, *105*, 136805.

[94] Novoselov, K. S.; Geim, A. K.; Morozov, S. V.; Jiang, D.-e.; Zhang, Y.; Dubonos, S. V.; Grigorieva, I. V.; Firsov, A. A. Electric field effect in atomically thin carbon films. *science* **2004**, *306*, 666–669.

[95] Novoselov, K.; Mishchenko, A.; Carvalho, A.; Neto, A. C. 2D materials and van der Waals heterostructures. *Science* **2016**, *353*.

[96] Geim, A. K.; Grigorieva, I. V. Van der Waals heterostructures. *Nature* **2013**, *499*, 419–425.

[97] Feng, X.; Schlüter, A. D. Towards macroscopic crystalline 2D polymers. *Angewandte Chemie International Edition* **2018**, *57*, 13748–13763.

[98] Colson, J. W.; Dichtel, W. R. Rationally synthesized two-dimensional polymers. *Nature chemistry* **2013**, *5*, 453–465.

[99] Makiura, R.; Motoyama, S.; Umemura, Y.; Yamanaka, H.; Sakata, O.; Kitagawa, H. Surface nano-architecture of a metal–organic framework. *Nature materials* **2010**, *9*, 565–571.

[100] Dong, R.; Zhang, T.; Feng, X. Interface-assisted synthesis of 2D materials: trend and challenges. *Chemical reviews* **2018**, *118*, 6189–6235.

[101] Sheberla, D.; Sun, L.; Blood-Forsythe, M. A.; Er, S.; Wade, C. R.; Brozek, C. K.; Aspuru-Guzik, A.; Dincă, M. High electrical conductivity in Ni_3 (2,3,6,7,10,11-hexaiminotriphenylene) 2, a semiconducting metal–organic graphene analogue. *Journal of the American Chemical Society* **2014**, *136*, 8859–8862.

[102] Dong, R.; Pfeffermann, M.; Liang, H.; Zheng, Z.; Zhu, X.; Zhang, J.; Feng, X. Large-area, free-standing, two-dimensional supramolecular polymer single-layer sheets for highly efficient electrocatalytic hydrogen evolution. *Angewandte Chemie International Edition* **2015**, *54*, 12058–12063.

[103] Sahabudeen, H.; Qi, H.; Glatz, B. A.; Tranca, D.; Dong, R.; Hou, Y.; Zhang, T.; Kuttner, C.; Lehnert, T.; Seifert, G., et al. Wafer-sized multifunctional polyimine-based two-dimensional conjugated polymers with high mechanical stiffness. *Nature communications* **2016**, *7*, 1–8.

[104] Dong, R.; Han, P.; Arora, H.; Ballabio, M.; Karakus, M.; Zhang, Z.; Shekhar, C.; Adler, P.; Petkov, P. S.; Erbe, A., et al. High-mobility band-like charge transport in a semiconducting two-dimensional metal–organic framework. *Nature materials* **2018**, *17*, 1027–1032.

[105] Bauer, T.; Zheng, Z.; Renn, A.; Enning, R.; Stemmer, A.; Sakamoto, J.; Schlüter, A. D. Synthesis of free-standing, monolayered organometallic sheets at the air/water interface. *Angewandte Chemie International Edition* **2011**, *50*, 7879–7884.

[106] Matsumoto, M.; Valentino, L.; Stiehl, G. M.; Balch, H. B.; Corcos, A. R.; Wang, F.; Ralph, D. C.; Mariñas, B. J.; Dichtel, W. R. Lewis-acid-catalyzed interfacial polymerization of covalent organic framework films. *Chem* **2018**, *4*, 308–317.

[107] Müller, V.; Shao, F.; Baljozovic, M.; Moradi, M.; Zhang, Y.; Jung, T.; Thompson, W. B.; King, B. T.; Zenobi, R.; Schlüter, A. D. Structural characterization of a covalent monolayer sheet obtained by two-dimensional polymerization at an air/water interface. *Angewandte Chemie International Edition* **2017**, *56*, 15262–15266.

[108] Wang, W.; Schlüter, A. D. Synthetic 2D polymers: A critical perspective and a look into the future. *Macromolecular rapid communications* **2019**, *40*, 1800719.

[109] Dienstmaier, J. F.; Gigler, A. M.; Goetz, A. J.; Knochel, P.; Bein, T.; Lyapin, A.; Reichlmaier, S.; Heckl, W. M.; Lackinger, M. Synthesis of well-ordered COF monolayers: surface growth of nanocrystalline precursors versus direct on-surface polycondensation. *ACS nano* **2011**, *5*, 9737–9745.

[110] Cardenas, L.; Gutzler, R.; Lipton-Duffin, J.; Fu, C.; Brusso, J. L.; Dinca, L. E.; Vondráček, M.; Fagot-Revurat, Y.; Malterre, D.; Rosei, F., et al. Synthesis and electronic structure of a two dimensional π-conjugated polythiophene. *Chemical Science* **2013**, *4*, 3263–3268.

[111] Kaspar, C.; Ravoo, B.; van der Wiel, W.; Wegner, S.; Pernice, W. The rise of intelligent matter. *Nature* **2021**, *594*, 345–355.

[112] Kanao, K.; Harada, S.; Yamamoto, Y.; Honda, W.; Arie, T.; Akita, S.; Takei, K. Highly selective flexible tactile strain and temperature sensors against substrate bending for an artificial skin. *Rsc Advances* **2015**, *5*, 30170–30174.

[113] Kim, J.; Lee, M.; Shim, H. J.; Ghaffari, R.; Cho, H. R.; Son, D.; Jung, Y. H.; Soh, M.; Choi, C.; Jung, S., et al. Stretchable silicon nanoribbon electronics for skin prosthesis. *Nature communications* **2014**, *5*, 1–11.

[114] Fernández-Caramés, T. M.; Fraga-Lamas, P. Towards the Internet of smart clothing: A review on IoT wearables and garments for creating intelligent connected e-textiles. *Electronics* **2018**, *7*, 405.

[115] Oh, S.-W.; Nam, S.-M.; Kim, S.-H.; Yoon, T.-H.; Kim, W. S. Self-Regulation of Infrared Using a Liquid Crystal Mixture Doped with Push–Pull Azobenzene for Energy-Saving Smart Windows. *ACS Applied Materials & Interfaces* **2021**, *13*, 5028–5033.

[116] Walther, A. From responsive to adaptive and interactive materials and materials systems: A roadmap. *Advanced Materials* **2020**, *32*, 1905111.

[117] Kathan, M.; Hecht, S. Photoswitchable molecules as key ingredients to drive systems away from the global thermodynamic minimum. *Chemical Society Reviews* **2017**, *46*, 5536–5550.

[118] Taniguchi, T.; Asahi, T.; Koshima, H. Photomechanical azobenzene crystals. *Crystals* **2019**, *9*, 437.

[119] Evans, S.; Johnson, S.; Ringsdorf, H.; Williams, L.; Wolf, H. Photoswitching of azobenzene derivatives formed on planar and colloidal gold surfaces. *Langmuir* **1998**, *14*, 6436–6440.

[120] Comstock, M. J.; Levy, N.; Kirakosian, A.; Cho, J.; Lauterwasser, F.; Harvey, J. H.; Strubbe, D. A.; Fréchet, J. M.; Trauner, D.; Louie, S. G., et al. Reversible photomechanical switching of individual engineered molecules at a metallic surface. *Physical review letters* **2007**, *99*, 038301.

[121] Nacci, C.; Baroncini, M.; Credi, A.; Grill, L. Reversible photoswitching and isomer-dependent diffusion of single azobenzene tetramers on a metal surface. *Angewandte Chemie International Edition* **2018**, *57*, 15034–15039.

[122] Umemoto, T.; Ishikawa, K.; Takezoe, H.; Fukuda, A.; Sasaki, T.; Ikeda, T. Photoisomerization observed by means of scanning tunneling microscopy. *Japanese journal of applied physics* **1993**, *32*, L936.

[123] Blinov, L. M. *Structure and properties of liquid crystals*; Springer Science & Business Media, 2010; Vol. 123.

[124] Castellano, J. A. *Liquid gold: the story of liquid crystal displays and the creation of an industry*; World Scientific, 2005.

[125] Möltgen, H.; Kleinermanns, K. Resonance enhanced scanning tunneling (REST) spectroscopy of molecular aggregates on graphite. *Physical Chemistry Chemical Physics* **2003**, *5*, 2643–2647.

[126] Otsuki, J. STM studies on porphyrins. *Coordination Chemistry Reviews* **2010**, *254*, 2311–2341.

[127] Tanikaga, R. Photochemical Rearrangement of Azoxybenzene to 2-Hydroxyazobenzene and cis-trans Isomerization. *Bulletin of the Chemical Society of Japan* **1968**, *41*, 2151–2155.

[128] Zhao, X.; Zheng, W.; Zhang, Y.; Huang, W. cis alkenes stabilized by intramolecular sulphur$\cdots\pi$ interactions. *Chemical Communications* **2020**, *56*, 814–817.

[129] Feng, C. L.; Zhang, Y.; Jin, J.; Song, Y.; Xie, L.; Qu, G.; Jiang, L.; Zhu, D. Completely interfacial photoisomerization of 4-hydroxy-3'-trifluoromethyl-azobenzene studied by STM on HOPG. *Surface science* **2002**, *513*, 111–118.

[130] Cheng, K.-Y.; Lin, C.-H.; Tzeng, M.-C.; Mahmood, A.; Saeed, M.; Chen, C.-h.; Ong, C. W.; Lee, S.-L. Superstructure manipulation and electronic measurement of monolayers comprising discotic liquid crystals with intrinsic dipole moment using STM/STS. *Chemical Communications* **2018**, *54*, 8048–8051.

[131] Miniewicz, A.; Orlikowska, H.; Sobolewska, A.; Bartkiewicz, S. Kinetics of thermal cis–trans isomerization in a phototropic azobenzene-based single-component liquid crystal in its nematic and isotropic phases. *Physical Chemistry Chemical Physics* **2018**, *20*, 2904–2913.

[132] Pace, G.; Ferri, V.; Grave, C.; Elbing, M.; von Hänisch, C.; Zharnikov, M.; Mayor, M.; Rampi, M. A.; Samorì, P. Cooperative light-induced molecular movements of highly ordered azobenzene self-assembled monolayers. *Proceedings of the National Academy of Sciences* **2007**, *104*, 9937–9942.

[133] Motoyama, S.; Makiura, R.; Sakata, O.; Kitagawa, H. Highly crystalline nanofilm by layering of porphyrin metal- organic framework sheets. *Journal of the American Chemical Society* **2011**, *133*, 5640–5643.

[134] Kang, K.; Lee, K.-H.; Han, Y.; Gao, H.; Xie, S.; Muller, D. A.; Park, J. Layer-by-layer assembly of two-dimensional materials into wafer-scale heterostructures. *Nature* **2017**, *550*, 229–233.

[135] Kang, K.; Xie, S.; Huang, L.; Han, Y.; Huang, P. Y.; Mak, K. F.; Kim, C.-J.; Muller, D. A.; Park, J. High-mobility three-atom-thick semiconducting films with wafer-scale homogeneity. *Nature* **2015**, *520*, 656–660.

[136] Liu, Y.; Huang, Y.; Duan, X. Van der Waals integration before and beyond two-dimensional materials. *Nature* **2019**, *567*, 323–333.

[137] Liu, Y.; Weiss, N. O.; Duan, X.; Cheng, H.-C.; Huang, Y.; Duan, X. Van der Waals heterostructures and devices. *Nature Reviews Materials* **2016**, *1*, 1–17.

[138] Jariwala, D.; Marks, T. J.; Hersam, M. C. Mixed-dimensional van der Waals heterostructures. *Nature materials* **2017**, *16*, 170–181.

[139] Wang, C.; He, Q.; Halim, U.; Liu, Y.; Zhu, E.; Lin, Z.; Xiao, H.; Duan, X.; Feng, Z.; Cheng, R., et al. Monolayer atomic crystal molecular superlattices. *Nature* **2018**, *555*, 231–236.

[140] Chen, X.; Wu, Z.; Xu, S.; Wang, L.; Huang, R.; Han, Y.; Ye, W.; Xiong, W.; Han, T.; Long, G., et al. Probing the electron states and metal-insulator transition mechanisms in molybdenum disulphide vertical heterostructures. *Nature communications* **2015**, *6*, 1–8.

[141] Redel, E.; Wang, Z.; Walheim, S.; Liu, J.; Gliemann, H.; Wöll, C. On the dielectric and optical properties of surface-anchored metal-organic frameworks: A study on epitaxially grown thin films. *Applied Physics Letters* **2013**, *103*, 091903.